

SPECTROSCOPY OF NEUTRON UNBOUND STATES IN
NEUTRON RICH OXYGEN ISOTOPES

By

Nathan Henry Frank

A DISSERTATION

Submitted to
Michigan State University
in partial fulfillment of the requirements
for the degree of

DOCTOR OF PHILOSOPHY

Department of Physics and Astronomy

2006

ABSTRACT

SPECTROSCOPY OF NEUTRON UNBOUND STATES IN NEUTRON RICH OXYGEN ISOTOPES

By

Nathan Henry Frank

The existence of so-called magic nuclei has been well established for nuclei near stability; they are well reproduced by the nuclear shell model. Magic nuclei have a certain number of protons and neutrons. These nuclei are more bound than their respective neighbors. In the past it was assumed that the magic numbers are fixed throughout the nuclear chart; there is mounting evidence that this in fact is not the case. Recently the breakdown of the well known magic neutron number $N = 20$ and the emergence of a new magic number of neutrons $N = 16$ has been proposed for the oxygen isotopes. Experimental observations of the relative binding energies of nuclei, such as the one-neutron separation energy as well as shell model calculations suggest that $N = 16$ is indeed a new magic number for neutron rich nuclei very far from stability. Under this assumption, the nucleus ^{24}O with a magic number of eight protons and sixteen neutrons would be doubly-magic. Another observable to identify magic nuclei is a high first excited state energy. Previous experiments to verify this prediction of the first excited states of ^{23}O and ^{24}O demonstrated that these states are unstable to neutron emission. The goal of the current work was to observe the neutron unbound states of ^{23}O and ^{24}O by neutron decay spectroscopy.

The energy of the neutron unbound first excited states were reconstructed by measuring the momentum vector of the charged fragment and neutron resulting from the decay. Neutron unbound $^{23}\text{O}^*$ and $^{24}\text{O}^*$ were produced using a ^{26}Ne beam impinged on a beryllium target. The charged particles were bent away from the neutrons using the recently commissioned Sweeper Magnet and analyzed in charged particle detec-

tors. The neutrons continued at zero degrees to be detected by the Modular Neutron Array, MoNA.

Finally, the observed decay spectra of $^{22}\text{O}^*$, $^{23}\text{O}^*$ and $^{24}\text{O}^*$ were compared to simulation. The decay of $^{22}\text{O}^*$ is consistent with a thermalized neutron source, while neutron unbound excited states of 48 ± 10 keV and 670 ± 150 keV were observed in the decay energy spectra for ^{23}O and ^{24}O , respectively. The theoretical prediction of the first excited state of ^{23}O is consistent with the measurement. The theoretical predictions considering the first excited state of ^{24}O are in fairly good agreement. Comparison of theory to the measurement confirm a change in shell structure around $N = 16$ in oxygen isotopes.

To my wife, Holly

ACKNOWLEDGMENTS

First, I would like to thank my advisor Michael Thoennessen. He has been a constant source of knowledge, advice and encouragement. He helped me stay on track and I could not have proceeded to this point without him. I thank professors Thomas Glasmacher, Alex Brown, Stuart Tessmer and Wayne Repko for being on my guidance committee and providing assistance along the way.

I must thank the Operations and Support staff at the NSCL for providing the beam necessary to perform the experiment of this dissertation. I especially would like to thank those who helped build the mapping mechanism for the Sweeper Magnet.

I would like to thank the National High Magnetic Field Laboratory for building and testing the Sweeper Magnet.

I would like to thank the members of the MoNA collaboration for building MoNA and helping perform the experiment. I would especially like to thank Andreas Schiller, Jean-Luc Lecouey, Thomas Baumann, Bryan Luther, Joe Finck, Ruth Howes, Jim Brown, and Paul DeYoung for helpful discussion, advice, and dissertation reading.

I would like to thank John Yurkon his help in building and repairing the charged particle detectors. I would like to thank Daniel Bazin for help in working with the charged particle detector system as well as a constant source of advice on COSY.

I would like to thank Heiko Scheit for writing the simulation and for helpful advice and assistance.

I thank my fellow graduate students for your companionship and support through the long days and nights of graduate school.

I thank my family and friends for constant support, especially my wife Holly for her patience and support through this entire process.

Contents

1	Introduction	1
2	Theory and Motivation	5
2.1	Indications for Shell Evolution in Oxygen Isotopes	5
2.2	Previous Experimental Result	9
2.3	2^+ Energy Predictions from Theory	11
2.4	Production of ^{24}O	12
3	Method	15
3.1	Decay Energy Reconstruction	15
3.2	Production Mechanism	18
3.3	Experimental Setup	18
3.3.1	Beamline Tracking Detectors	19
3.3.2	Target Chamber	23
3.3.3	Sweeper Magnet	23
3.3.4	Charged Particle Detectors	26
3.3.5	MoNA	28
3.4	Electronics and Data Acquisition	28
3.4.1	Charged Particle Electronics	28
3.4.2	MoNA Electronics	31
3.4.3	Trigger Electronics	33
4	Analysis	34
4.1	Overview	34
4.2	Secondary Beam Particle Identification	35
4.3	CRDC Calibration	36
4.4	PPAC Calibration	44
4.5	Element Identification	45
4.5.1	Ionization Chamber Calibration	48
4.5.2	dE Scintillator Calibration	48
4.6	Isotopic Identification	51
4.6.1	TKE Scintillator Calibration	51
4.6.2	Time-of-Flight Corrections	57
4.7	Neutron Processing	68
4.8	Fragment Reconstruction	72
4.9	Neutron Decay Spectra	78

5	Discussion	90
5.1	Simulation	90
5.2	Comparisons to Simulated Spectra	92
5.3	Physics Interpretation	96
6	Summary and Conclusions	104
	<i>Bibliography</i>	107

List of Figures

1.1	First excited state energy versus atomic number (A) and neutron number (N) for calcium isotopes.	2
1.2	Schematic plot of energy levels in the nuclear shell model.	4
2.1	Effective single particle energies (ESPE's) vs neutron number for oxygen isotopes.	6
2.2	First excited state energy versus atomic number (A) or neutron number (N) for even oxygen isotopes.	7
2.3	Calculated neutron ESPE's for ^{30}Si (a) and ^{24}O (b) starting with the $1s_{1/2}$ sub-shell.	8
2.4	One neutron separation energy (S_n) versus neutron number (N) for odd N , even Z (a) and odd N , odd Z (b).	10
2.5	Measured γ -ray energy spectrum from experiment for ^{24}O (solid line) and a simulated (dashed) γ -ray energy peak.	11
2.6	Evolution of the 2_1^+ state in oxygen isotopes.	13
3.1	Schematic of the ^{24}O decay.	16
3.2	Schematic of the coupled cyclotron facility and the A1900 fragment separator at the NSCL.	17
3.3	Experimental setup	20
3.4	Charged particle detector layout	21
3.5	Experimental beamline	21
3.6	Parallel plate avalanche counters	22
3.7	Sweeper Magnet technical drawings	24
3.8	Cathode readout drift chamber	25
3.9	dE and TKE scintillators.	27
3.10	Charged particle electronics	29
3.11	Charged particle trigger	32
4.1	Energy loss (dE) versus RF time.	37
4.2	Energy loss versus the A1900 Fragment Separator focal plane dispersive position.	38
4.3	Time-of-Flight secondary beam identification plot	39
4.4	y -position versus x -position for the mask of CRDC2	40
4.5	Mean y -position of both CRDCs versus run number for all charged fragments in coincidence with incoming ^{26}Ne secondary beam.	41
4.6	Pad width σ_{pad} for CRDC1 (left) and CRDC2 (right).	43

4.7	Sample width σ_{sample} for CRDC1 (left) and CRDC2 (right).	43
4.8	Integrated charge for CRDC1 (left) and CRDC2 (right).	44
4.9	Integrated charge for x_{PPAC1} (upper-left), y_{PPAC1} (upper-right), x_{PPAC2} (lower-left), y_{PPAC2} (lower-right).	45
4.10	Sample width σ_{sample} for x_{PPAC1} (upper-left), y_{PPAC1} (upper-right), x_{PPAC2} (lower-left), y_{PPAC2} (lower-right).	46
4.11	Pad width σ_{pad} for x_{PPAC1} (upper-left), y_{PPAC1} (upper-right), x_{PPAC2} (lower-left), y_{PPAC2} (lower-right).	47
4.12	Ionization chamber pad peaks versus run number.	49
4.13	Energy loss in ionization chamber versus vertical position at the dE scintillator (y_{dE}).	50
4.14	Down-right PMT integrated charge versus y_{dE} .	52
4.15	Down-right PMT integrated charge versus x_{dE} .	53
4.16	dE scintillator energy loss	54
4.17	Energy loss (ionization chamber) versus energy loss (dE scintillator).	55
4.18	TKE scintillator energy loss (arbit. units)	56
4.19	ToF of down-left PMT versus down-right PMT after travel time correction.	58
4.20	Average ToF versus θ_x without (top) and with (bottom) θ_x correction.	59
4.21	Corrected ToF $t_{ToF_{corr1}}$ versus constructed dispersive position x' uncorrected (top) and corrected (bottom).	61
4.22	Corrected ToF $t_{ToF_{corr2}}$ versus x -position at the reaction target uncorrected (top) and corrected (bottom).	62
4.23	Corrected ToF $t_{ToF_{corr3}}$ versus y -position at the reaction target uncorrected (top) and corrected (bottom).	63
4.24	Corrected ToF $t_{ToF_{corr4}}$ versus θ_y uncorrected (top) and corrected (bottom).	65
4.25	Final corrected ToF t_{final}	66
4.26	TKE energy versus ToF t_{final}	67
4.27	Projection from TKE versus corrected ToF plot.	68
4.28	Prompt γ -ray and neutron peaks in the neutron ToF spectrum.	69
4.29	y -position versus x -position on MoNA.	71
4.30	A Sweeper Magnet map with positive dispersive position marked at both the reaction target and CRDC1.	74
4.31	Dispersive position distribution x_{ta} at the reaction target.	76
4.32	Forward-tracked CRDC1 x -position versus measured CRDC1 x -position.	78
4.33	Forward-tracked CRDC1 x -angle versus measured CRDC1 x -angle.	79
4.34	Forward-tracked CRDC1 y -position versus measured CRDC1 y -position.	79
4.35	Forward-tracked CRDC1 y -angle versus measured CRDC1 y -angle.	80
4.36	Backward reconstructed target x -angle versus measured target x -angle.	80
4.37	Backward reconstructed target y -position versus measured target y -position.	81
4.38	Backward reconstructed target y -angle versus measured target y -angle.	81
4.39	Backward reconstructed secondary beam energy versus measured secondary beam energy.	82

4.40	Reconstructed fragment kinetic energy spectrum (left) and neutron kinetic energy spectrum (right) for $^{22}\text{O}^*$ (top), $^{23}\text{O}^*$ (middle), and $^{24}\text{O}^*$ (bottom).	83
4.41	Reconstructed fragment angle spectrum (left) and neutron angle spectrum (right) for unbound $^{22}\text{O}^*$ (top), $^{23}\text{O}^*$ (middle), and $^{24}\text{O}^*$ (bottom).	84
4.42	Opening angle (θ_{open}) between neutron and charged fragment (left) and reconstructed decay energy spectrum (20 keV/bin) (right) for $^{22}\text{O}^*$ (top), $^{23}\text{O}^*$ (middle), and $^{24}\text{O}^*$ (bottom).	86
4.43	Decay energy spectra for correlated (points with error bars) and uncorrelated (histogram) neutron and charged fragment events for $^{22}\text{O}^*$ (top) and $^{23}\text{O}^*$ (bottom).	87
4.44	Top: $^{24}\text{O}^*$ spectrum with scaled $^{23}\text{O}^*$ spectrum used for the subtraction. Bottom: Subtracted decay energy spectrum of $^{24}\text{O}^*$	89
5.1	Decay energy spectrum of $^{22}\text{O}^*$	93
5.2	Decay energy spectrum of $^{23}\text{O}^*$	94
5.3	Decay energy spectrum of $^{24}\text{O}^*$	95
5.4	Oxygen isotope production paths	97
5.5	Single particle configurations for unbound states in ^{23}O	99
5.6	^{23}O decay energy fit and theory comparison.	100
5.7	Single particle configuration for the 2^+ unbound state in ^{24}O	101
5.8	^{24}O decay energy fit and theory comparison.	103
6.1	First excited 2^+ state for nuclei near $Z = 8$	105

List of Tables

2.1	Two-proton knockout cross-sections comparing calculated measured	14
4.1	Isotope to total ratio from the production in the A1900 fragment separator without and with the extended focal plane slits.	36
5.1	Beam properties used within the simulation.	90
5.2	Resolutions used in the simulation.	91
5.3	Mass excess, E_{decay} and resulting excitation energies for observed states in $^{23}\text{O}^*$ and $^{24}\text{O}^*$	98
5.4	Comparison of theoretical calculations of the first neutron unbound excited 2^+ state in ^{24}O	102

Chapter 1

Introduction

The atomic nucleus is an unique quantum-mechanical many-body system. The nucleus is made up of two kinds of nearly identical mass particles, protons and neutrons. The protons and neutrons are fermions; they have a spin of $1/2$. The neutrons have zero electric charge while the protons have an electric charge equal in magnitude but opposite in sign to the electron. The protons and neutrons in the nucleus interact via the strong nuclear force and the electromagnetic (Coulomb) force. The nuclear force holds the nucleus together and the Coulomb force pushes the protons apart. The distance between the nucleons is on the order of 10^{-15} m because the strong force only attracts over very short distances. Despite the complicated quantum mechanical interactions of nucleons that comprise the nucleus, experiments on nuclei have observed distinctive properties.

There are about 2500 nuclei for which we have experimental information, but only about 300 of these are found naturally occurring on earth [1]. This provides a large amount of experimental data to study properties of nuclei as they evolve with the number of protons and neutrons. There are certain numbers of neutrons and protons that show specific indicators of the structure of nuclei. These “magic” numbers are experimentally observed for 2, 8, 20, 28, 50, 82, etc. A high lying first excited state for even proton (Z) and neutron (N) numbers, lower level density, the large number of

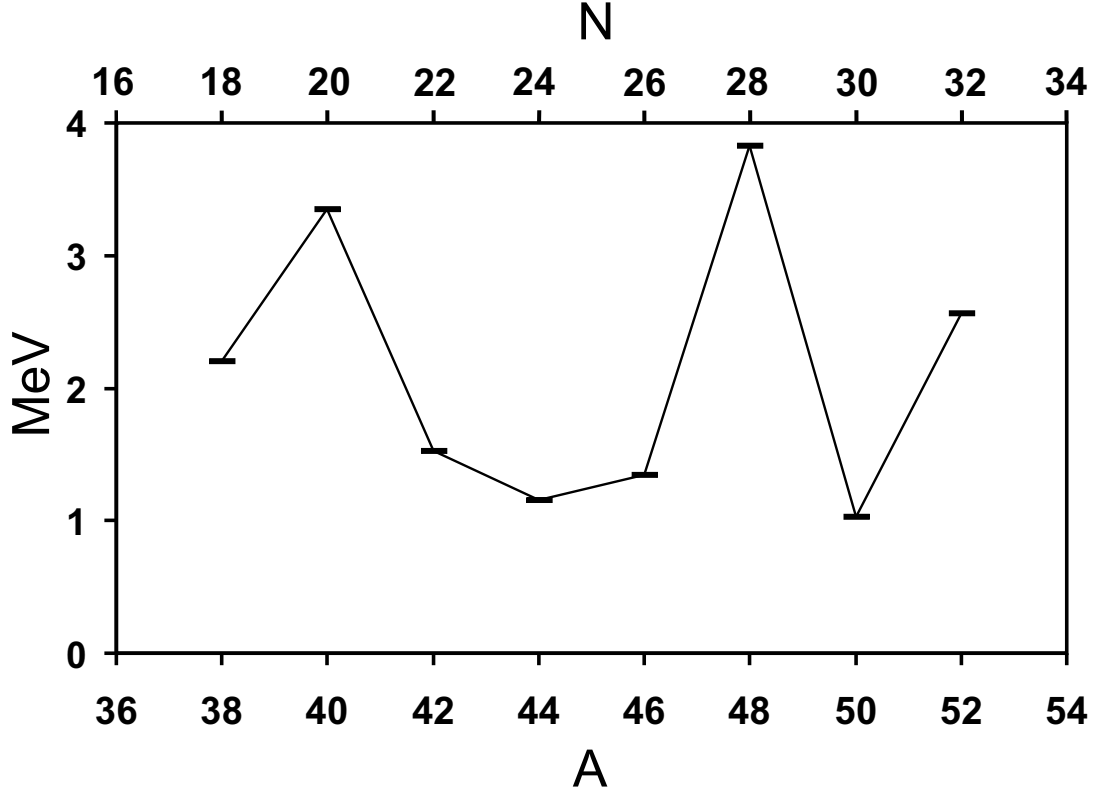


Figure 1.1: First excited state energy versus atomic number (A) and neutron number (N) for calcium isotopes. Data points from: $^{38,46,50,52}\text{Ca}$ [3], ^{40}Ca [4], ^{42}Ca [5], ^{44}Ca [6], and ^{48}Ca [7].

stable nuclei or more tightly bound nuclei, and large two neutron separation energy (S_{2n}), one neutron separation energy (S_n), or one proton separation energy (S_p) are all indicators of magic numbers of neutrons and protons [2]. The separation energy is the energy necessary to excite a nucleus to the point where it decays via particle or multi-particle emission. As an example of neutron magic numbers, Figure 1.1 shows the energy of the first excited state of calcium isotopes as a function of atomic number (A). The large energies for ^{40}Ca and ^{48}Ca indicate the existence of the magic numbers $N = 20$ and $N = 28$, respectively.

To be able to describe the observed properties of nuclei is a continuing challenge for theory. Due to the complicated nature of nuclei, calculations based on the interactions of individual nucleons is currently only possible up to $A \sim 12$ and will probably

not be possible for much heavier nuclei due to computation limitations [8]. Since a microscopic approach is not tractable to heavier nuclei, a model based on effective interactions in a mean field has to be applied. This approach is known as the nuclear shell model which resembles the shell structure found for electrons in the hydrogen atom. The difference between the two shell structures are the Coulomb versus nuclear and Coulomb forces and the relative size of 10^{-10} m versus 10^{-15} m for electrons and nuclei, respectively. In contrast to the atomic system, where the electrons move in the central potential of the nucleus, in the nuclear system the potential for the nucleons, has to be approximately by a mean potential generated by the nucleons themselves.

In addition to the differences in the calculation of energy levels for electrons and nuclei, protons and neutrons have a stronger spin-orbit coupling force than the atomic system. The shell model structure shown in Figure 1.2 (adapted from Reference [9]) shows the energy separations for major shells for a spherical potential with a strong spin-orbit coupling. The number of nuclei summed up to major shell closures correspond to the magic numbers observed in experiments on stable nuclei, which illustrates the success of the nuclear shell model. There are many approaches to calculate the many different parameter sets of the nuclear shell model. In general, theories can be accurate to within a few hundred keV of experimental values [1].

Based on the observed behavior of stable nuclei, a reasonable assumption would be that magic numbers at stability continue out to the neutron deficient and neutron rich nuclei at the driplines. The driplines mark the limits of nuclear binding and are located at nuclei that are unstable to proton decay (proton dripline) or neutron decay (neutron dripline). The assumption that shell structure does not change away from stability is not generally correct. For example, the neutron number of $N = 14$ has been shown to appear as a magic number for ^{22}O [10] which has six more neutrons than the heaviest stable oxygen isotope. The experimental confirmation of new magic numbers or the disappearance of known magic numbers due to changes in shell structure far from stability is a current topic of research in nuclear physics.

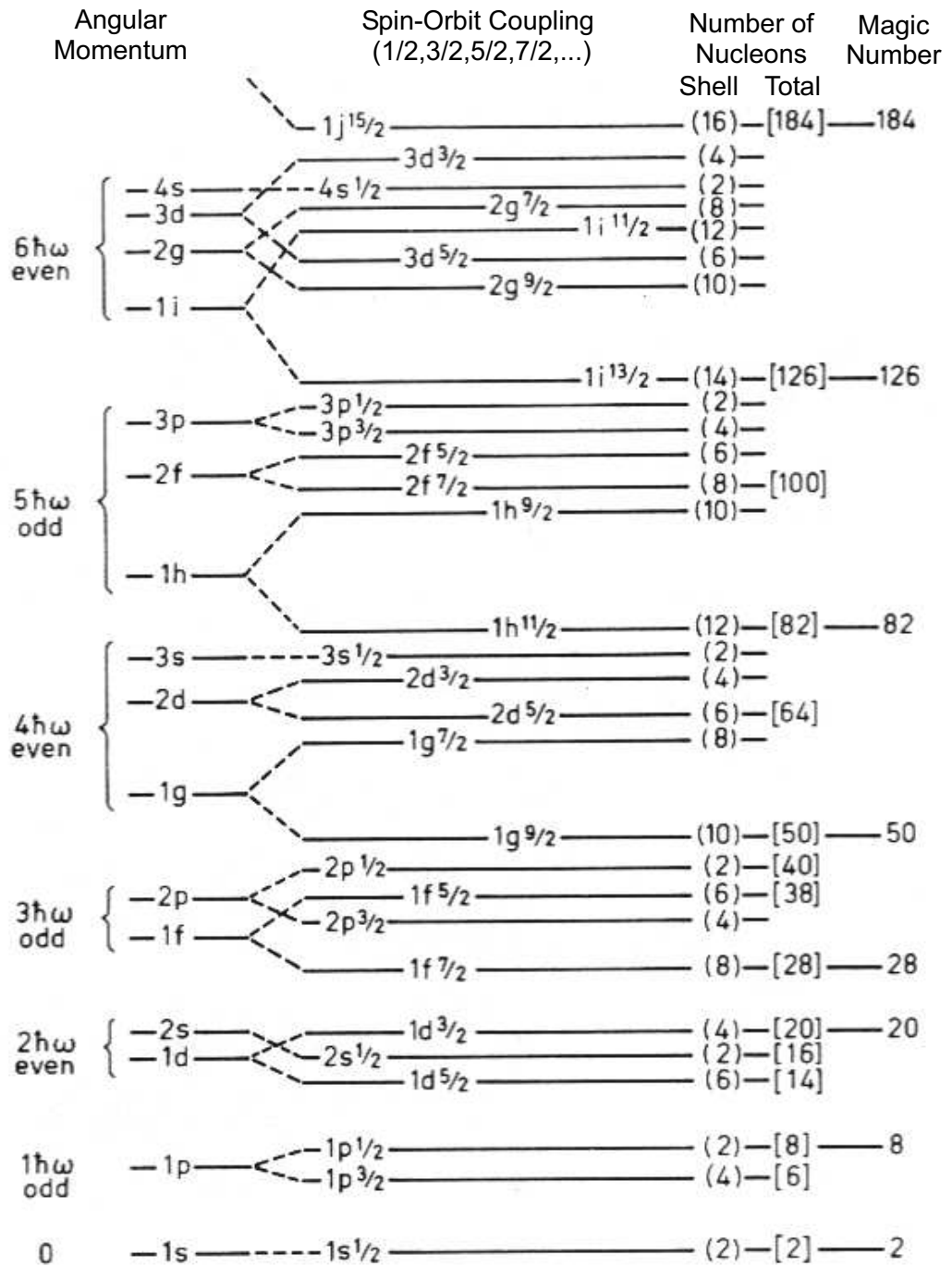


Figure 1.2: Schematic plot of energy levels in the nuclear shell model adapted from Reference [9]. The first column lists the principle angular momenta levels from the harmonic oscillator potential, the second column includes the spin-orbit potentials, the third column labels the sub-shell and total occupancy, and the last column represents the magic numbers.

Chapter 2

Theory and Motivation

2.1 Indications for Shell Evolution in Oxygen Isotopes

A change in shell structure has been predicted for neutron-rich oxygen isotopes. The two plots shown in Figure 2.1 show the effective single particle energy (ESPE) based on the “universal SD” (USD) and the Kuo-Brown G-matrix calculations for oxygen isotopes [11], where the effective single particle energy corresponds to the energy level for a nucleon in a particular sub-shell by taking into account the forces of the other nucleons. The USD interaction is based on an empirical fit of known data within the sd major shell [12,13] and the G-matrix uses an effective mean field potential [14,15]. The even-neutron isotopes of $^{22,24,28}\text{O}$ are marked to emphasize the shell gaps expected in the calculations. A magic number is interpreted as a large energy gap between sub-shells. The neutrons in $^{22,24,28}\text{O}$ occupy the sd major shell which is made up of the sub-shells $0d_{5/2}$, $1s_{1/2}$ and $0d_{3/2}$. A gap between the $1s_{1/2}$ and $0d_{3/2}$ sub-shells for neutrons in the calculations predict ^{24}O to be a doubly-magic nucleus like ^{16}O , which means that both N and Z are magic numbers. The two calculations differ in the prediction of ^{22}O as a doubly magic nucleus due to a difference in the expected sub-shell energy gap which would be reflected in the energy of the first excited state

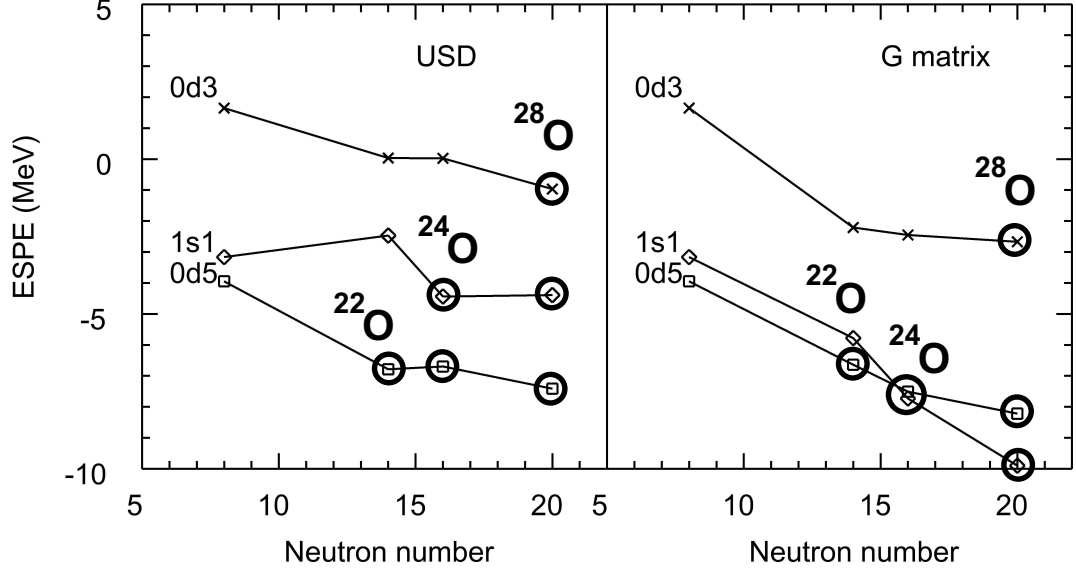


Figure 2.1: Effective single particle energies (ESPE's) vs neutron number for oxygen isotopes. Shell model calculations using USD (left) or G-matrix (right) from Reference [11]. Open circles indicate filled sub-shells for ^{22}O , ^{24}O , ^{28}O , respectively.

as shown in Figure 2.2. Figure 2.2 shows the high lying excited state supporting the USD calculations for the doubly magic nature of ^{22}O [10]. Both calculations agree on the prediction of the new magic number of $N = 16$ which is the topic of the present thesis.

Neither magic numbers of $N = 14, 16$ are observed near stability as a result of a small sub-shell energy gap. The spin-isospin component of the nucleon-nucleon force has been suggested as the reason for this change in structure far from stability [17]. The nucleon-nucleon interaction used in Reference [17] is a product of isospin (τ) and spin (σ) operators. The tensor resulting from this product has large attraction for protons and neutrons of the same orbital angular momentum (l) and opposite spin giving total angular momentum of $j_> = l + 1/2$ and $j_< = l - 1/2$. The overlap of opposite spin and isospin wave functions with the potential above yields an angular momentum independent energy shift, making this overlap a monopole interaction [18]. Figure 2.3 shows the difference between the $0d_{3/2}$ orbital for neutrons in ^{30}Si and ^{24}O . The filling of the $0d_{5/2}$ orbital for protons in ^{30}Si makes neutrons in the $0d_{3/2}$ orbital

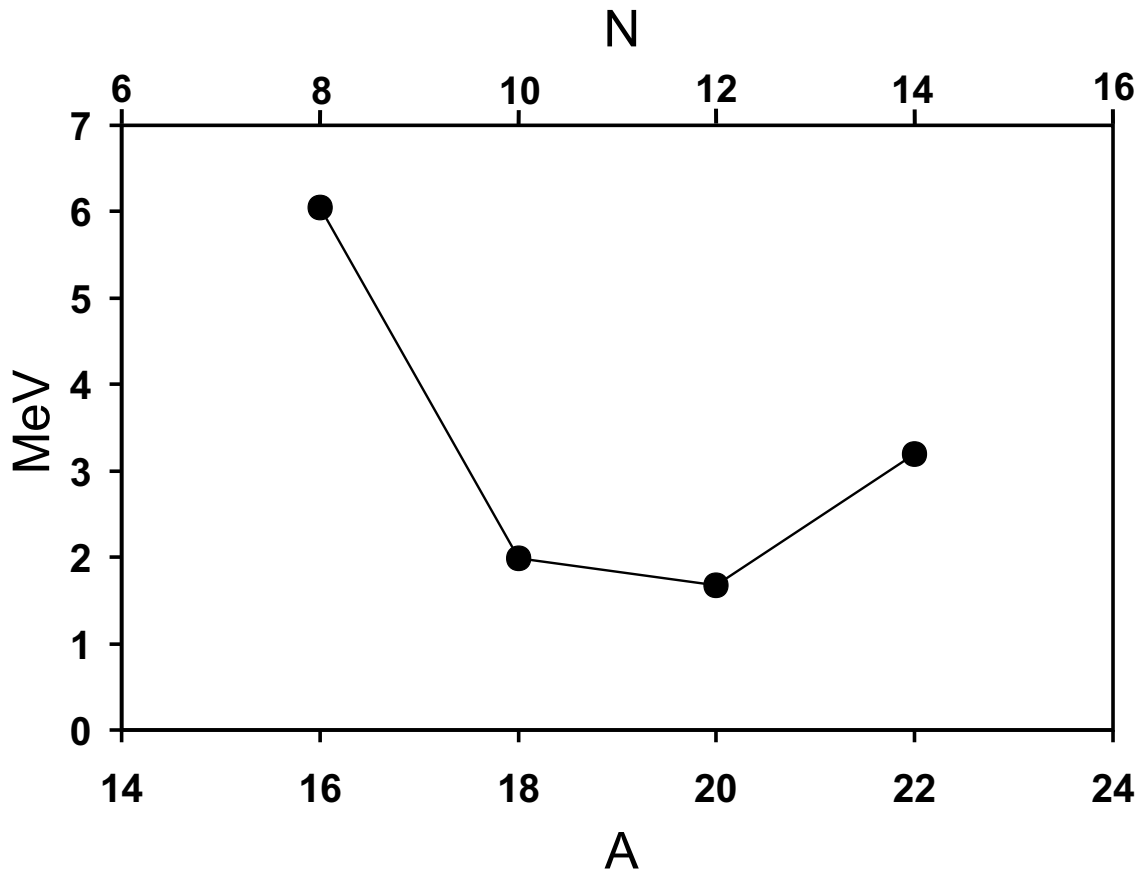


Figure 2.2: First excited state energy versus atomic number (A) or neutron number (N) for even oxygen isotopes. Data points taken from References [3,16].

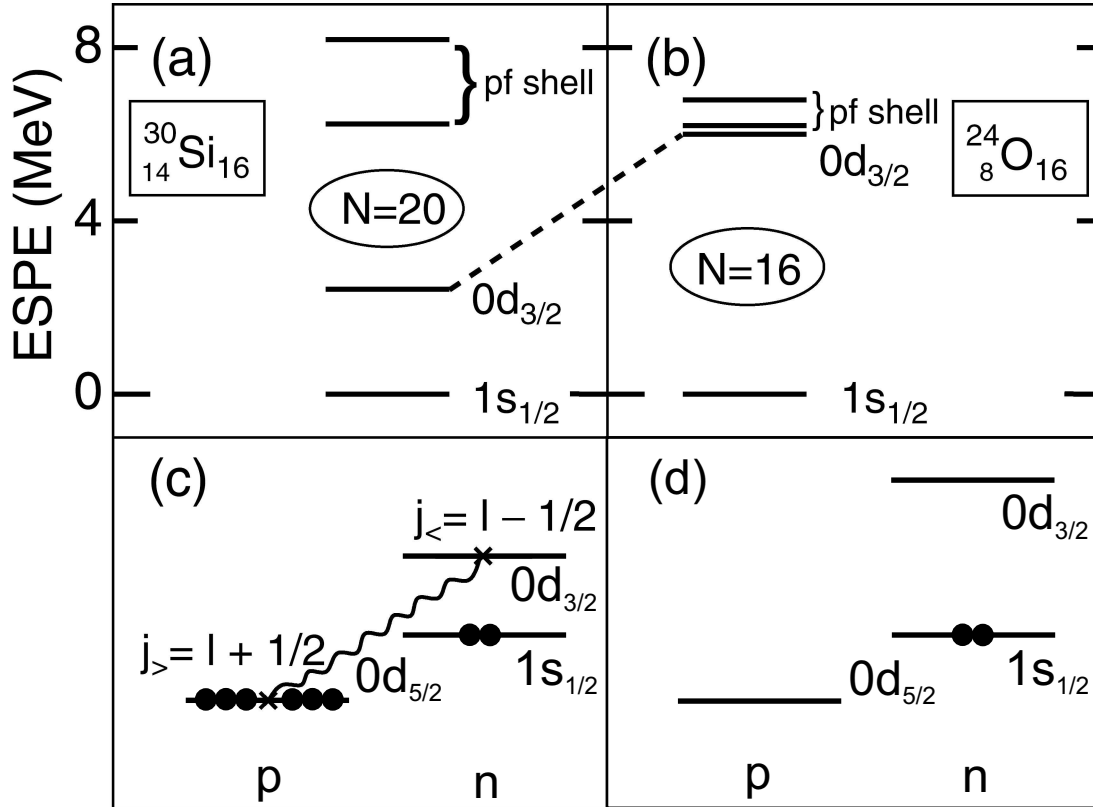


Figure 2.3: Calculated neutron ESPE's for ^{30}Si (a) and ^{24}O (b) starting with the $1s_{1/2}$ sub-shell. The change of the $0d_{3/2}$ sub-shell is indicated by the dotted line connecting (a) and (b). The occupation of proton and neutron sub-shells is shown for ^{30}Si (c) and ^{24}O (d). The major interaction generating the difference in the sub-shell of $1d_{3/2}$ in ^{30}Si and ^{24}O is represented by the wiggly line in (c). Figure adapted from Reference [17].

more bound than for ^{24}O where there are no protons in the $0d_{5/2}$ orbital. The effect of even one more proton in the $0d_{5/2}$ explains why ^{26}F is bound and ^{25}O is not. The monopole effect in this calculation is stronger than the pairing effect because ^{26}O is neutron unbound. As a result of the monopole interaction, ^{24}O is expected to have an increase of the energy gap between the $0d_{3/2}$ and $1s_{1/2}$ sub-shells for neutrons as compared to nuclei closer to stability.

The first experimental evidence for a large energy gap between the $0d_{3/2}$ and $1s_{1/2}$ sub-shells for neutrons in ^{24}O came from experimental observation of the one-neutron separation energy. Figure 2.4 is adapted from a study of one-neutron separation energy

(S_n) as it changes across neutron number [19]. Each joined set of points is for one value of the isospin number (T_z), which moves across many different isotopes. Decreases in the one neutron separation energy with an increase of neutron number are a good indicator for a magic number as the result of a large energy gap between sub-shells. The $N = 8$ magic number is indicated on the plot by a vertical line along the $T_z = 1/2$ line of the one neutron separation energy, where the nucleus to the left is ^{13}C and to the right is ^{17}O . The break for $N = 8$ is also visible for $T_z = 0$ between the nuclei ^{14}N and ^{18}F as well as for $T_z = 1$ between the nuclei ^{12}B and ^{16}N . Another important feature for the magic number of $N = 8$ is that evidence for it disappears for the $T_z = 3/2$ line between ^{11}Be and ^{15}C . Also to be noted is the break for $N = 20$ for many values of T_z . The $N = 20$ magic number disappears for $T_z = 9/2$ between ^{29}Ne and ^{33}Mg which is consistent with the result of ^{32}Mg at $T_z = 4$ [20]. The next noticeable feature is the unexpected clear break for the one neutron separation energy for the $T_z = 7/2$ line at $N = 16$, between ^{23}O and ^{27}Ne . This new break does not exist for nuclei near stability and is an indication for the evolution of the shell structure leading to a new magic number for nuclei near the dripline in this region.

2.2 Previous Experimental Result

The one-neutron separation energy trends and theoretical calculations indicate that ^{24}O has a new closed shell at $N = 16$ due to an enhanced sub-shell energy gap, which would make it doubly magic. A γ -ray and charged particle coincidence experiment was performed to search for the first excited 2^+ state of ^{24}O decaying to the 0^+ ground state [21]. The experiment measured γ -rays in coincidence with $^{20,21,22,23,24}\text{O}$. The spectrum shown in Figure 2.5 show that there is no γ -ray in coincidence with ^{24}O . The first 2^+ excited state is expected to have a configuration with one neutron in both the $1s_{1/2}$ and $0d_{3/2}$ sub-shells. Therefore the experiment is consistent with a larger energy gap between the $1s_{1/2}$ and $0d_{3/2}$ neutron sub-shells as compared to nuclei near

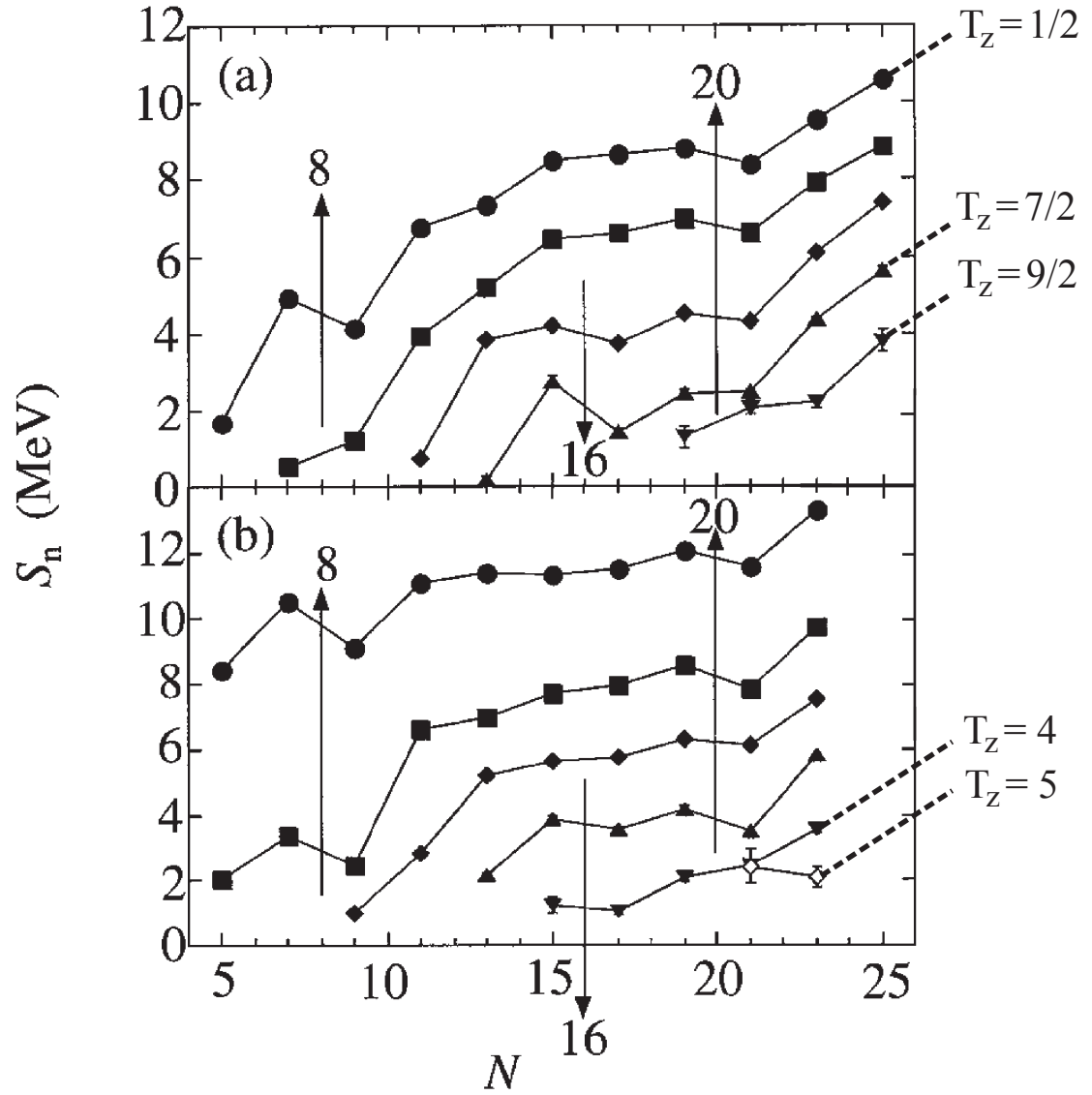


Figure 2.4: One neutron separation energy (S_n) versus neutron number (N) for odd N , even Z (a) and odd N , odd Z (b) adapted from Reference [19]. The lines connect points with the same T_z values, which are noted to the side for clarity.

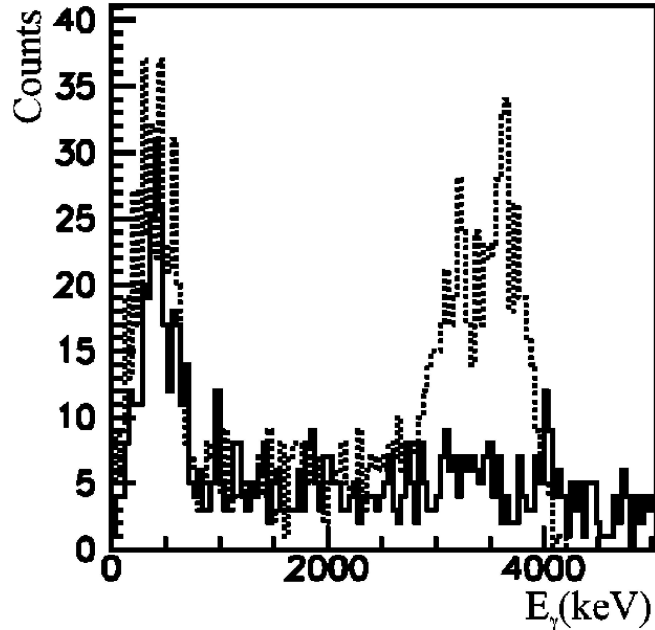


Figure 2.5: Measured γ -ray energy spectrum from experiment for ^{24}O (solid line) and a simulated (dashed) γ -ray energy peak [21]. The γ -ray peak was simulated with an energy of 3.7 MeV assuming 20% of the ^{24}O is produced in the 2_1^+ state. The lower limit of the production to the 2_1^+ state based on the data was 3%.

stability. It is noted here that the experiment also found that the first excited state of ^{23}O is neutron unbound. This requires a different experimental method to be used to confirm the doubly magic nature of ^{24}O since the state is likely to be unbound to neutron emission.

2.3 2^+ Energy Predictions from Theory

There have been several calculations that predict the energy of the first excited state for ^{24}O . Figure 2.6 shows a comparison of results from theoretical calculations to experimentally measured data for the first excited state of 2^+ for even oxygen isotopes. The experimentally known points are for $^{18,20,22}\text{O}$ [3, 16]. The theoretical calculations cover a wide range of methods. An Antisymmetrized Molecular Dynamics (AMD) calculation [22] is inconsistent with the data. Somewhat better agreement is achieved

by a quasiparticle random phase approximation (QRPA) calculation with Skyrme and pairing forces in [23]. In general shell model calculations show better agreement to the measured energies. A Monte-Carlo shell model using the USD and Kuo-Brown potential [24] and calculations using the Warburton-Becker-Millener-Brown (WBMB) hamiltonian [25] and USD with continuum [26] are all consistent with the first excited state energies of the data. Additional calculations performed for ^{24}O , a Random Phase Approximation (RPA) using the Gogny-D1S force [27] and a shell model calculation using the new USD interaction [28], predict that the excited state is above the one-neutron separation energy. Though not all theories reproduce the data, they all predict the 2_1^+ excited state of ^{24}O to be unbound with respect to one-neutron emission, consistent with the non-observation of a γ -ray transition [21].

2.4 Production of ^{24}O

To detect neutron-unbound decay, from excited states of ^{24}O , the states have to be populated. The predicted configuration for the excited state are one particle-one hole (1p - 1h) couplings of a $0d_{3/2}^1-1s_{1/2}^{-1}$ with states of total angular momentum $J = 1^+, 2^+$ or a $0d_{3/2}^1-0d_{5/2}^{-1}$ with states of $J = 1^+, 4^+$ [11], where the first two excited states are expected to be 2^+ and 1^+ , respectively. Possible choices of populating ^{24}O excited states are one-proton removal from ^{25}F or two-proton removal from ^{26}Ne . If ^{24}O is assumed to behave like a doubly-magic nucleus, another proton added to ^{24}O would be at a high energy. ^{25}F could then be thought of as a $0d_{5/2}$ proton coupled to a ^{24}O core. Therefore one-proton stripping of ^{25}F would be expected to populate the ground state with a much higher cross-section than the excited state in ^{24}O . With an estimated spectroscopic factor of 3% [28], the estimated cross-section from the ^{25}F ground state to the first excited 2^+ state of ^{24}O was approximately $0.12(\pm 0.018)$ mb. In comparison, the cross-section of ^{26}Ne in the ground state to the first excited 2^+ state was approximately 0.035 mb (see Table 2.1). The two-proton removal from

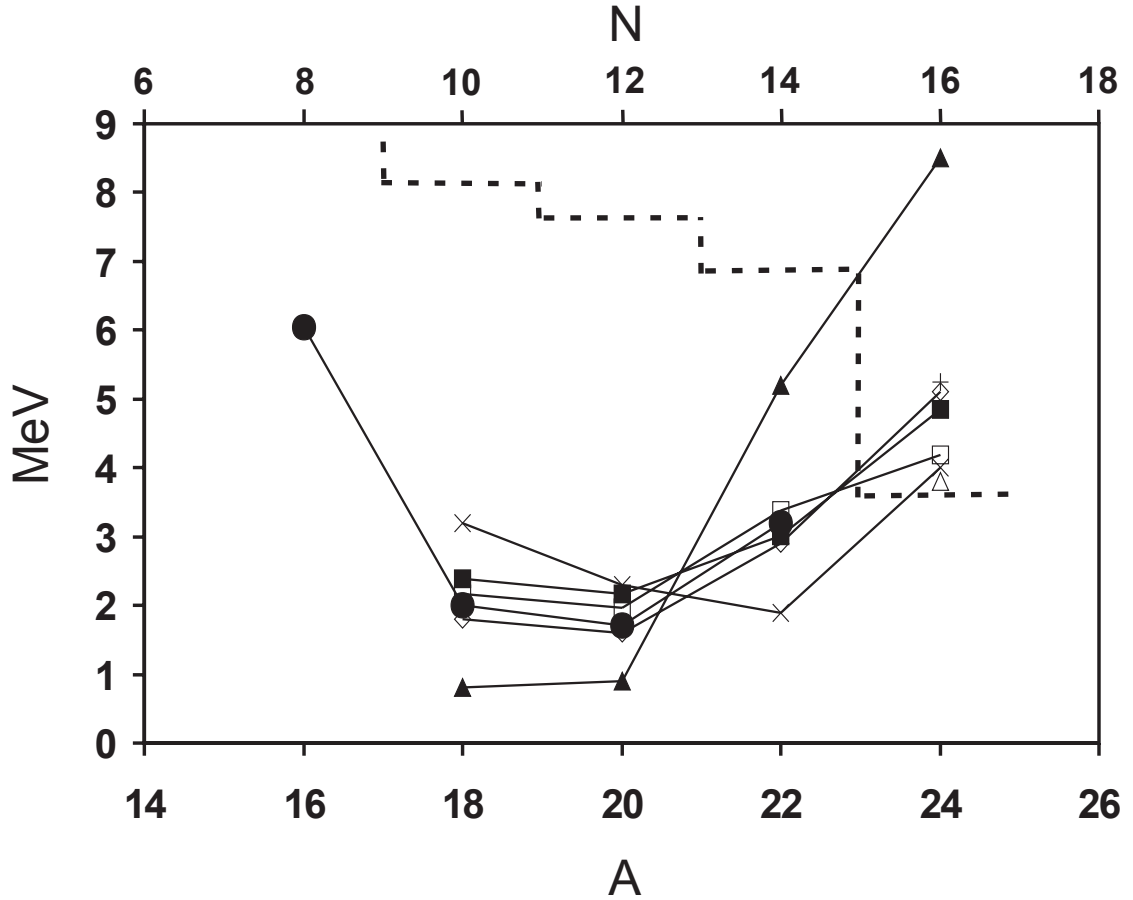


Figure 2.6: Evolution of the 2_1^+ state in oxygen isotopes. The dashed line marks the one-neutron separation energies for even oxygen isotopes of ^{16}O (15.6637 MeV), ^{18}O (8.044 MeV), ^{20}O (7.608 MeV), ^{22}O (6.85 MeV), and ^{24}O (3.61 MeV) (from Reference [29]). The theoretical calculations are Δ : Obertelli [27], \times : Khan [23], \square : Siiskonen [25], \blacksquare : Volya [26], \diamond : Utsuno [24], $+$: Brown [28], \blacktriangle : Thiamova [22]. The experimental points are \bullet : Firestone [3] and Belleguic [16] where the error bars are within the closed circles.

Table 2.1: Two-proton knockout cross-sections comparing calculations of two different models to measured values where applicable. When the final states are not resolved, “all” is mentioned instead of the level energy.

Beam energy (MeV/u)	Final nucleus	Level energy (MeV/u)	$\sigma^{(a)}_{-2p}$ (mb)	σ_{exp} (mb)
82	^{28}Mg	all	1.8	1.5(1)
88	^{30}Mg	all	1.3	0.49(5)
67	^{34}Si	all	2.2	0.76(10)
28	^9He	all	0.7	≈ 0.35
83	^{24}O	0	0.359 ^(b)	-
83	^{24}O	(4.18)	0.035 ^(b)	-

^acalculated with model from [31].

^bnew version including proton correlations [32].

^{26}Ne was chosen because the expected beam rates at the National Superconducting Cyclotron Laboratory were approximately a factor of 50 larger for ^{26}Ne compared to ^{25}F which made up for the difference in calculated cross-sections [30]. The two-proton cross-section was calculated using a model assuming a direct two-proton stripping reaction based on Reference [31]. Table 2.1 shows comparisons of calculated two-proton removal and measured cross-sections which agree within a factor of two. This provides confidence in the two-proton removal cross-section predicted for the excited 2^+ state of ^{24}O .

Chapter 3

Method

3.1 Decay Energy Reconstruction

The goal of the experiment was to measure the neutron unbound state(s) of ^{24}O . ^{24}O was produced using a two-proton stripping reaction from the secondary beam of ^{26}Ne . Then the decay products, ^{23}O and a neutron, were measured in coincidence. The neutron was detected in the Modular Neutron Array (MoNA) and the fragment's properties were measured using the Sweeper Magnet and charged particle detectors. The Sweeper Magnet bent the ^{26}Ne beam and charged fragments away from the beamline direction. The neutrons continued in the direction of the beamline to MoNA. Figure 3.1 shows a schematic of the decay. The decay was fully characterized by measuring the momentum vectors in the lab frame, which were constructed by measuring the energies and angles of the neutrons and charged fragments.

The decay energy is the energy above the one-neutron separation energy and is calculated using conservation of energy and momentum. The derivation is performed in four-vector notation for the charged particle \mathbf{p}_f and neutron \mathbf{p}_n :

$$\mathbf{p}_f = (E_f, \vec{p}_f) \tag{3.1}$$

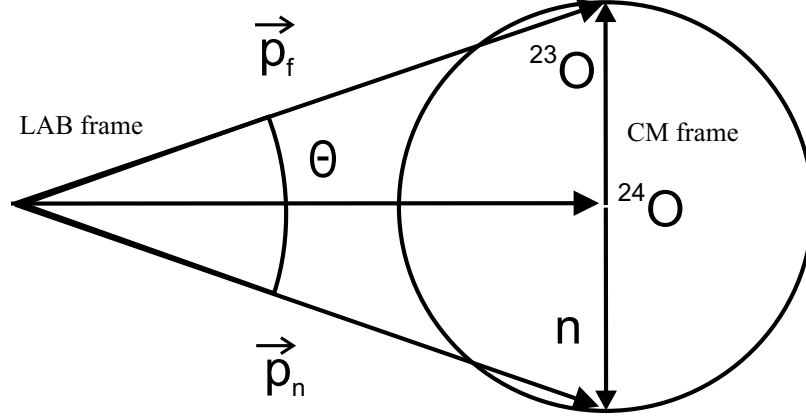


Figure 3.1: Schematic of the ^{24}O decay.

$$\mathbf{p}_n = (E_n, \vec{p}_n) \quad (3.2)$$

The constant \mathbf{m} is calculated using the four-vector product, which is constant regardless of the inertial frame the particles are in. The square of the invariant mass \mathbf{m}_{fn} is calculated from the four-vectors (Eq. 3.3) giving two terms; one that depend on the masses and a cross-term that depends on the energy (momentum) of the fragment and neutron as well as the opening angle between them, Θ , also shown in Figure 3.1. The square of the sum of the two four-vectors \mathbf{m}_{fn}^2 is calculated using:

$$\mathbf{m}_{\text{fn}}^2 = (\mathbf{p}_f + \mathbf{p}_n)^2 = \mathbf{p}_f^2 + \mathbf{p}_n^2 + 2\mathbf{p}_f\mathbf{p}_n = m_f^2 + m_n^2 + 2(E_f E_n - p_f p_n \cos \Theta) \quad (3.3)$$

where m_f and m_n are the fragment and neutron mass, respectively. The decay energy E_d is then the difference of the invariant mass and the sum of the fragment and neutron masses:

$$E_d = \sqrt{m_f^2 + m_n^2 + 2(E_f E_n - p_f p_n \cos \Theta)} - (m_f + m_n) \quad (3.4)$$

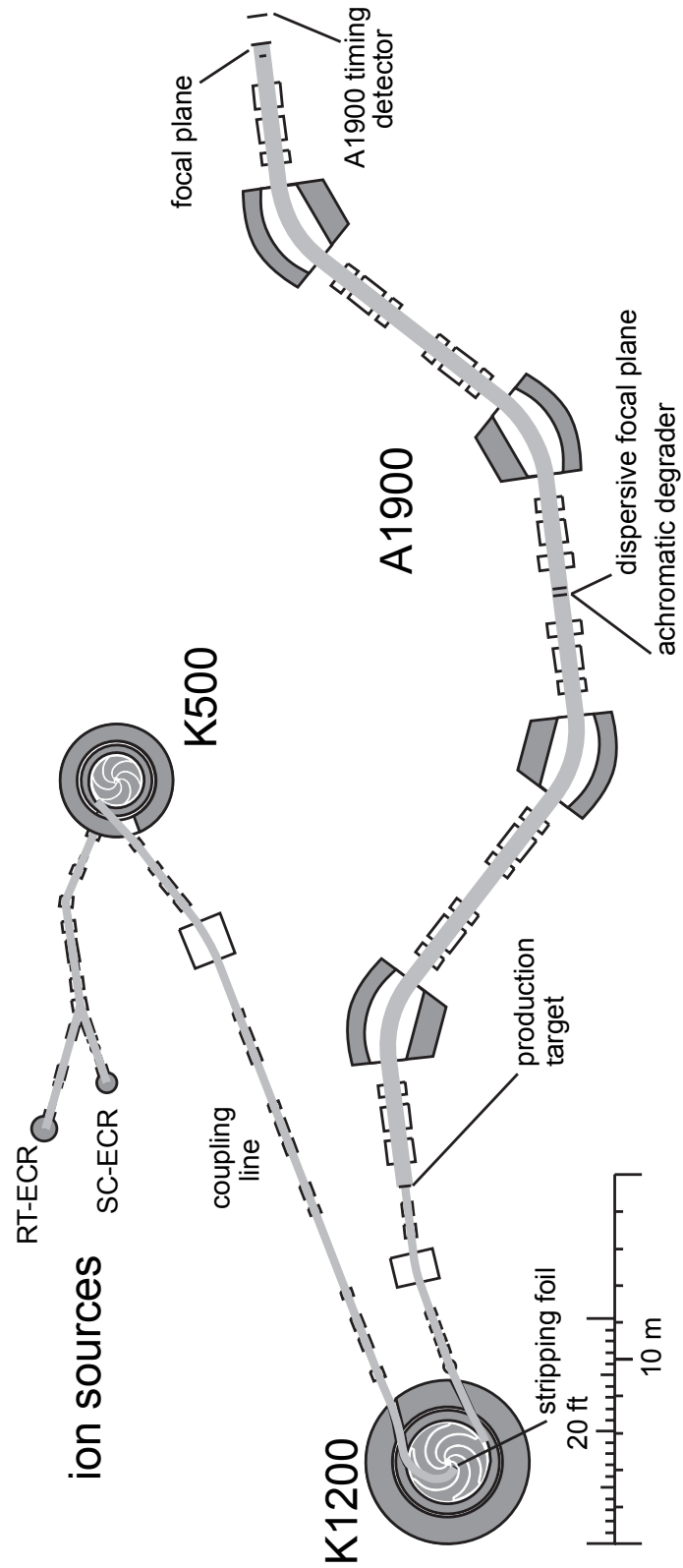


Figure 3.2: Schematic of the coupled cyclotron facility and the A1900 fragment separator at the NSCL.

3.2 Production Mechanism

The experiment was performed at the National Superconducting Cyclotron Laboratory (NSCL). The layout of the facility is shown in Figure 3.2. The primary beam of ^{40}Ar was produced in the ion source, entered the K500 cyclotron, and was accelerated to an intermediate energy of 12.5 MeV/A. The beam continued to the K1200 cyclotron where it was stripped of electrons and accelerated to 140 MeV/A. The primary beam intensity for data taking was $\sim 1.9\text{ e}\mu\text{A}$ ($\sim 105\text{ pA}$) as measured at the exit of the Coupled Cyclotrons. The ^{26}Ne secondary beam was produced by fragmentation from the primary beam on a 893 mg/cm^2 natural Be production target at the entrance of the A1900 Fragment Separator [33]. The A1900 uses dispersive dipole magnets to separate the beam particles by magnetic rigidity $B\rho$, the product of magnetic field and bending radius which is equal to the momentum-to-charge ratio. The A1900 consists of two mirror symmetric halves with a dispersive focal plane in between. This dispersive focal plane contains an achromatic degrader of 750 mg/cm^2 acrylic and momentum slits to limit the momentum acceptance. The A1900 was set to different $B\rho$ values for the first and second half of the separator, 4.01930 Tm and 3.58098 Tm, respectively, in order to select the ^{26}Ne nucleus. A timing detector located at the exit of the A1900 was necessary for identifying the ^{26}Ne particles at the experimental setup. The $B\rho$ of the ^{26}Ne after the timing scintillator was 3.56931 Tm. The beam purity was better than 80%.

3.3 Experimental Setup

The experimental setup is shown in Figure 3.3. It includes the tracking of the incoming beam particles. The neutrons are detected around zero degrees with the modular neutron detector array MoNA. The experiment performed requires tracking the paths of particles in front and behind the reaction target. The time-of-flight of the neutron is used to obtain its energy, and a position measurement is made to calculate the angle

of the neutron assuming a point-like target. The charged particles were deflected by the Sweeper magnet and detected and identified by a set of position sensitive, energy loss and energy detectors. The charged particle energy and angle at the reaction target were reconstructed from the measured angles and positions from the charged particle detectors using a matrix that calculated the trajectories from the field of the Sweeper Magnet.

For particle tracking in front of the target, the secondary beam passed through two parallel plate avalanche counters (PPACs), which measure x,y positions and together provide direction. The x,y position of PPAC2 and angles of the beam were used along with the quadrupole triplet transfer matrix to track the x,y positions and angles forward to the reaction target. For timing of the incoming particles, a timing scintillator detector was placed in front of the target, which provided a time reference right before the reaction target.

The charged particle detectors included two cathode readout drift chambers (CRDCs) to measure x,y position shown in Figure 3.4. The remaining detectors were used in obtaining isotopic separation. The ionization chamber and dE scintillator were used for element separation and identification by measuring the energy loss of the charged particles in each detector. The dE scintillator also generated the charged particle trigger. The time-of-flight measurement and energy measured in the TKE scintillator provided isotopic identification. The time-of-flight was constructed between the dE scintillator and the timing scintillator in front of the target. The TKE scintillator stopped the particles and measured the remaining energy.

3.3.1 Beamline Tracking Detectors

The secondary beam traveled down the beamline to the reaction target, shown in Figure 3.5. The secondary beam first passed through the PPACs, which were filled with 5 Torr of iso-butane gas, see Figure 3.6. The traversing beam excited the gas separating the molecules into positively and negatively charged ions. There were three

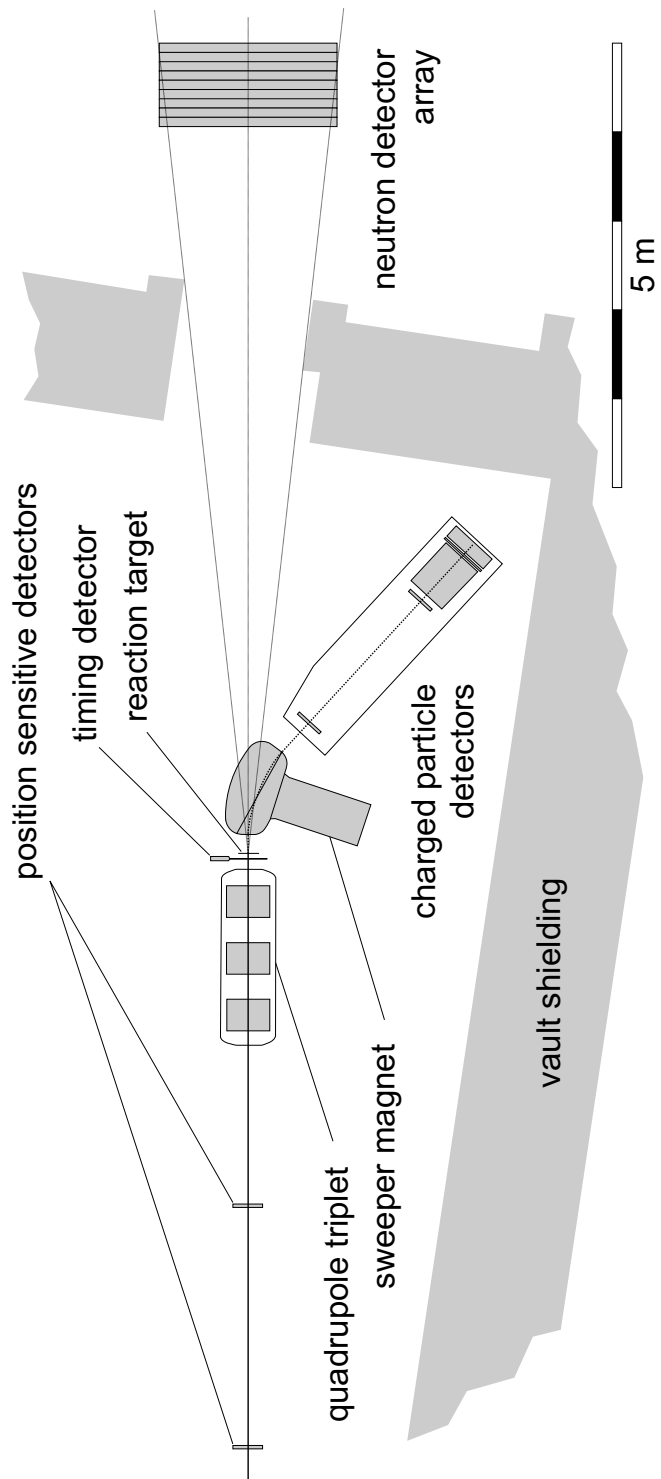


Figure 3.3: Experimental setup

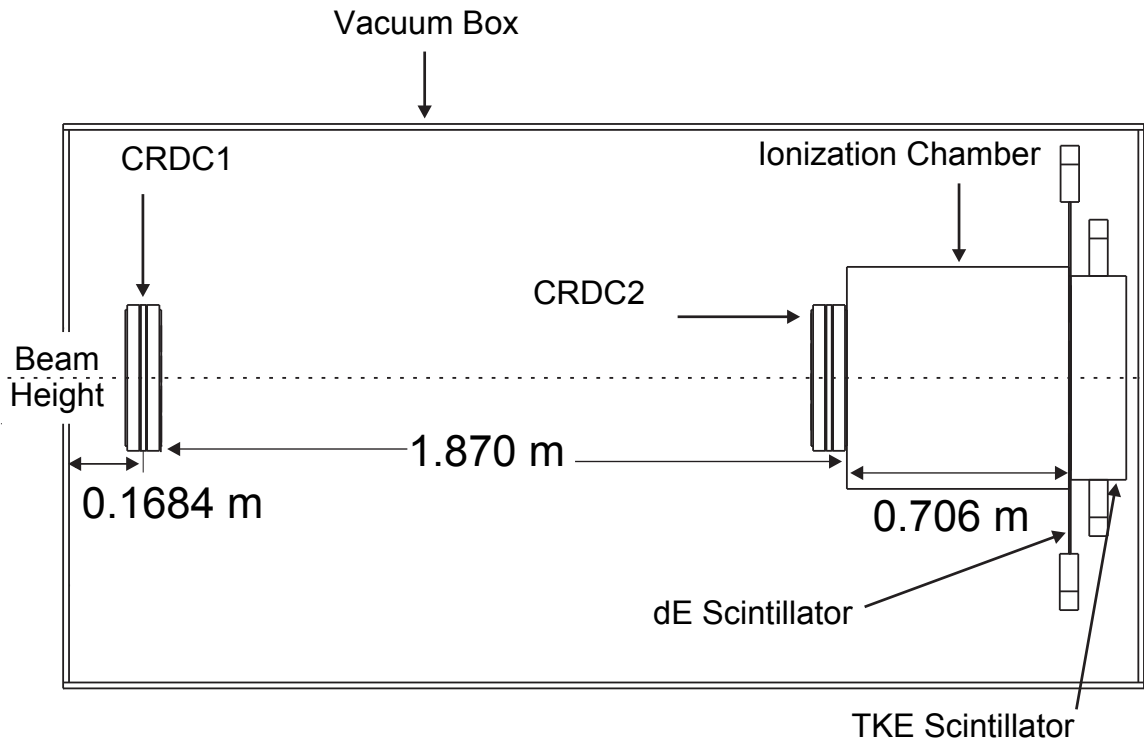


Figure 3.4: Charged particle detector layout

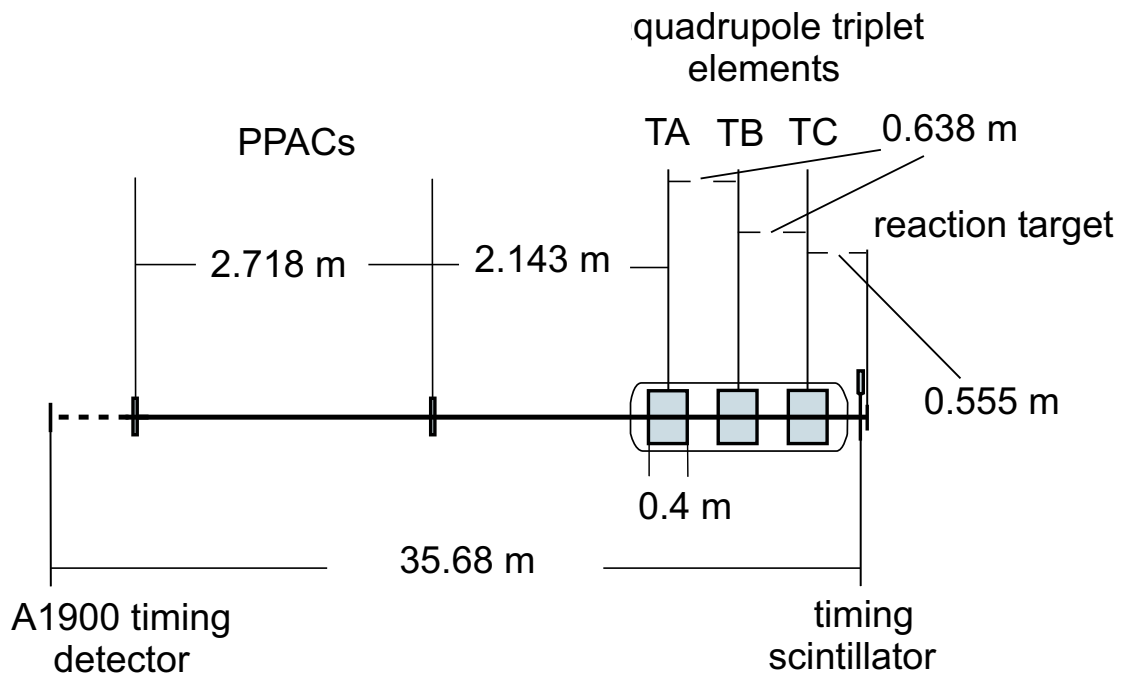


Figure 3.5: Experimental beamline

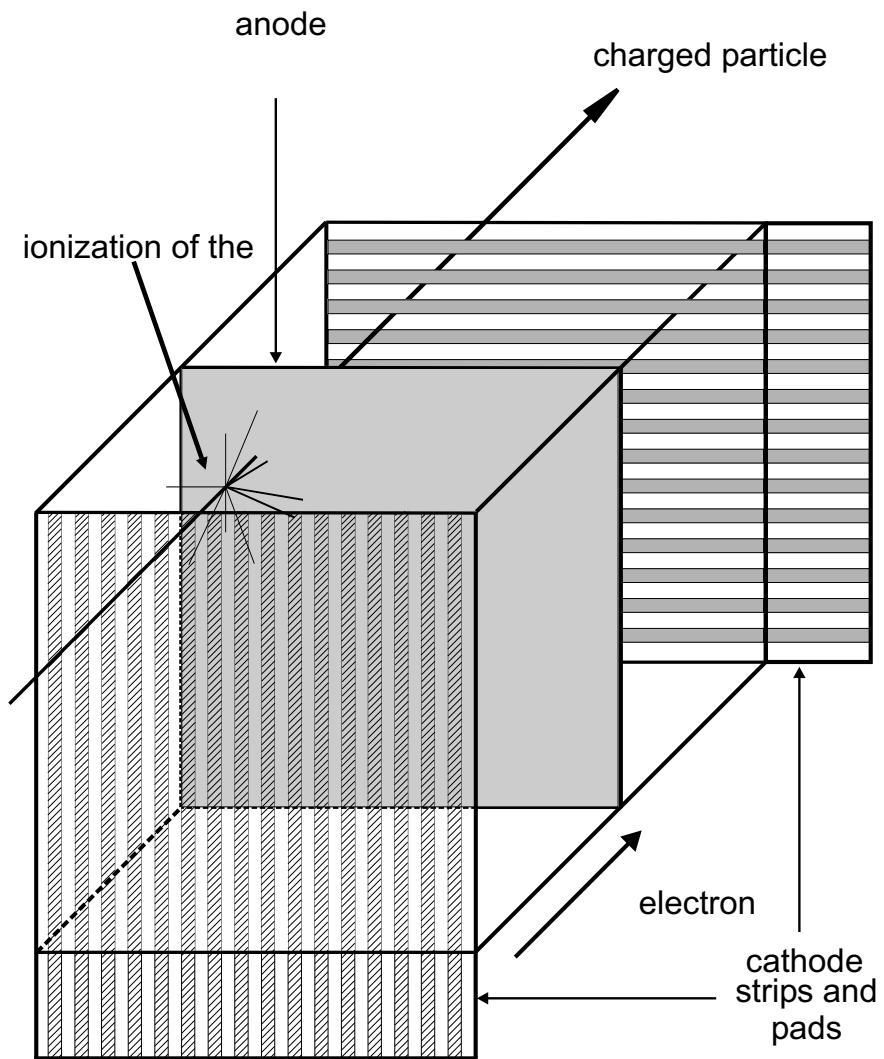


Figure 3.6: Parallel plate avalanche counters

parallel plates in each PPAC. The central plate was held at a positive voltage of 580 V to collect the electrons. The charge collected by the central plate induced an image charge on aluminum strips which were connected to pads placed along both directions. There were 128 pads spaced on both axis with a pitch of 1.27 mm.

3.3.2 Target Chamber

The target chamber included a timing scintillator and the reaction target. The reaction target was natural Be with a measured thickness of 721.3 mg/cm². The scintillator was made of BC-404 material with a thickness of 0.254 mm. The beam passed through the scintillator producing electron-hole pairs emitting light during recombination. The light was detected by one photo multiplier tube (PMT) mounted to it. A PMT converts photons into electrons with a photosensitive layer, called the photocathode. The electrons from the photocathode are multiplied by a multiplication structure which increases the number of electrons by factors of more than 10 million.

3.3.3 Sweeper Magnet

The superconducting Sweeper Magnet was built by the National High Magnetic Field Laboratory at Florida State University [34]. It is designed to bend particles up to 4 Tm at a 43 degree bend from the beamline using Niobium-Titanium (Nb-Ti) coils. The vertical gap of 14 cm provided a large opening for the neutrons produced in the reaction to pass through. Mechanical diagrams of the design are shown in Figure 3.7. There are two resistive coils (trim coils) placed on the outer edge of the magnet on the opposite side of the return yoke so that one could place magnetically sensitive detectors next to the magnet.

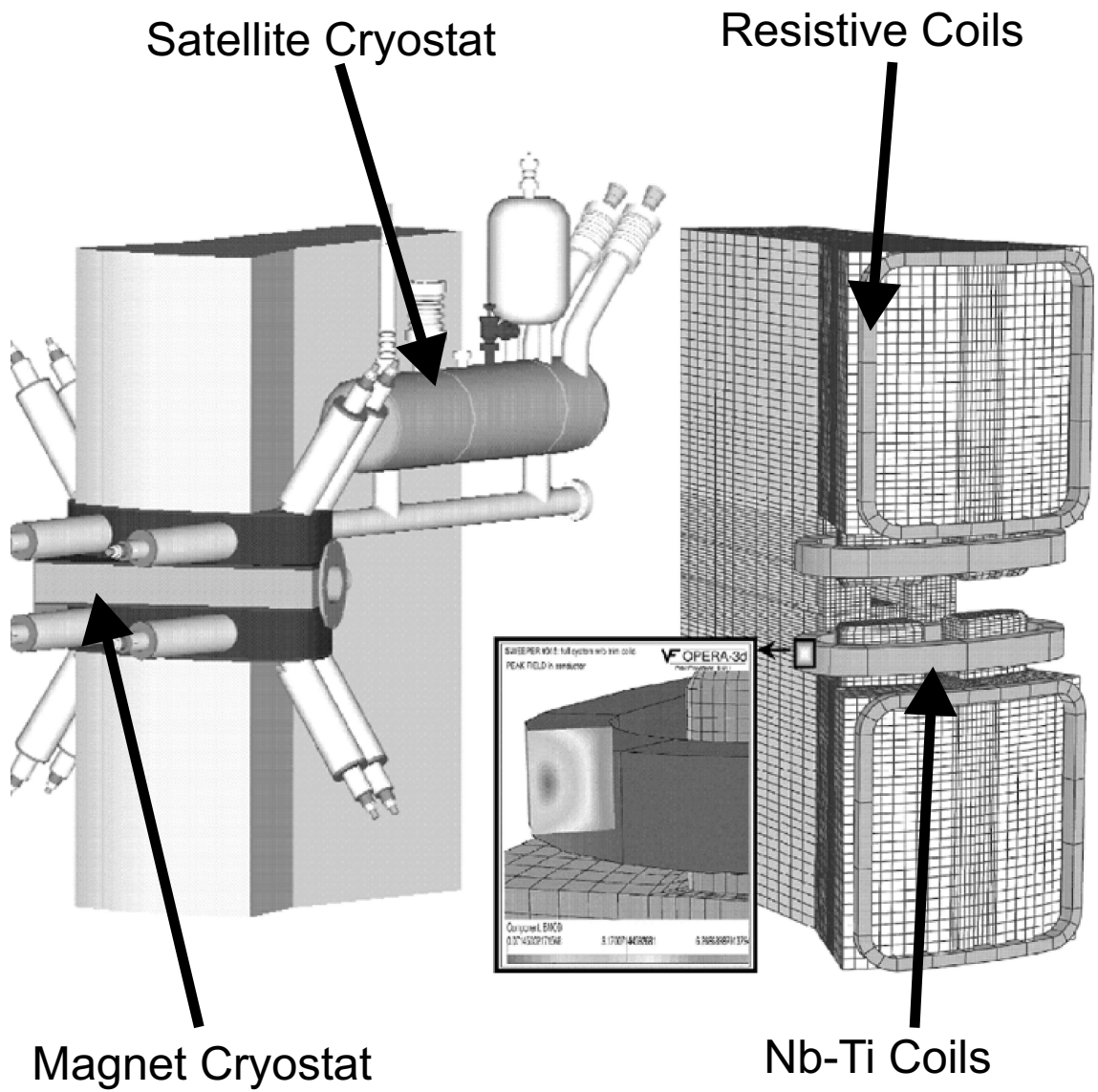


Figure 3.7: Sweeper Magnet technical drawings

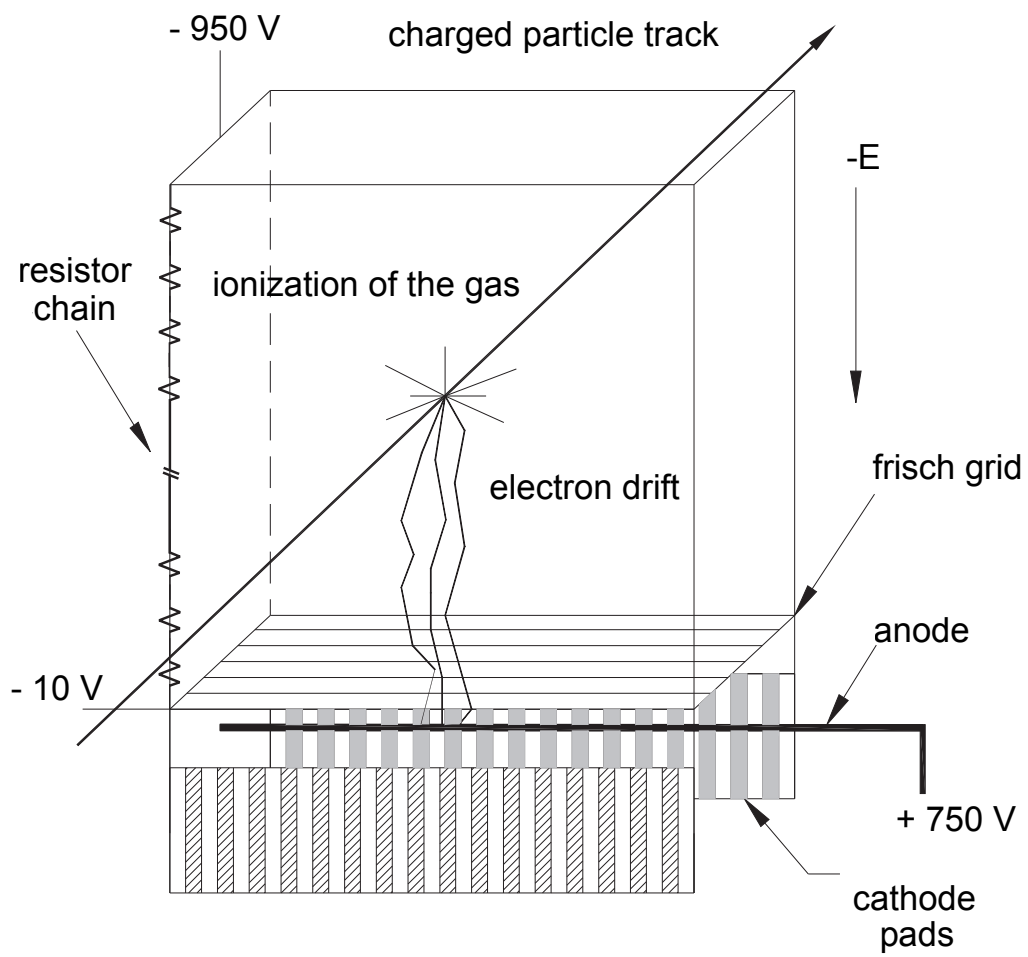


Figure 3.8: Cathode readout drift chamber

3.3.4 Charged Particle Detectors

Cathode Readout Drift Chambers (CRDCs) in the schematic shown in Figure 3.8 were used to detect the position of charged particles. They were filled with 20% isobutane and 80% CF_4 at an operating pressure of 50 Torr. The gas mixture enabled the particles to pass through the detector liberating charge pairs without creating an avalanche effect. The pairs were separated by an electric field produced by a plate at -950 V, which was connected through a resistor chain to a set of aluminum strips. At the end of this region, the electrons passed through a Frisch grid at -10 V and were collected by an anode wire held at 750 V. The region near the anode wire produced a small avalanche that increased the number of electrons available for collection. The x-direction was determined by using cathode pads to detect the induced charge from the anode wire. There were 128 pads with a pitch of 2.54 mm. The position in the y-direction was measured by the drift time, determined by the time difference of the trigger and the anode wire signal.

The ionization chamber was designed to help determine the particle charge by measuring the energy loss. The gas used was P-10, which is composed of 90% argon and 10% methane at an operating pressure of 150 Torr. The particles passed through the volume dissociated charge pairs and the electrons were pushed towards the 16 collection plates at the bottom of the chamber with a high negative voltage, approximately -1000 V. The collection plates were held at a positive potential, typically 100 V. The plates were used to reduce the overall noise as compared to using one large plate for collecting the electrons. Combining the 16 signals gave the energy loss measurement.

The plastic scintillators were made of BC-404 material with the dE scintillator of thickness 0.5 cm and the TKE scintillator of thickness 15 cm, shown in Figure 3.9. Both scintillators had four PMTs to detect the light produced by the scintillator. The dE scintillator used light guides to direct the light to the PMTs. The PMTs were operated at a voltage range of 1500-2000 V. The PMTs were labeled according to

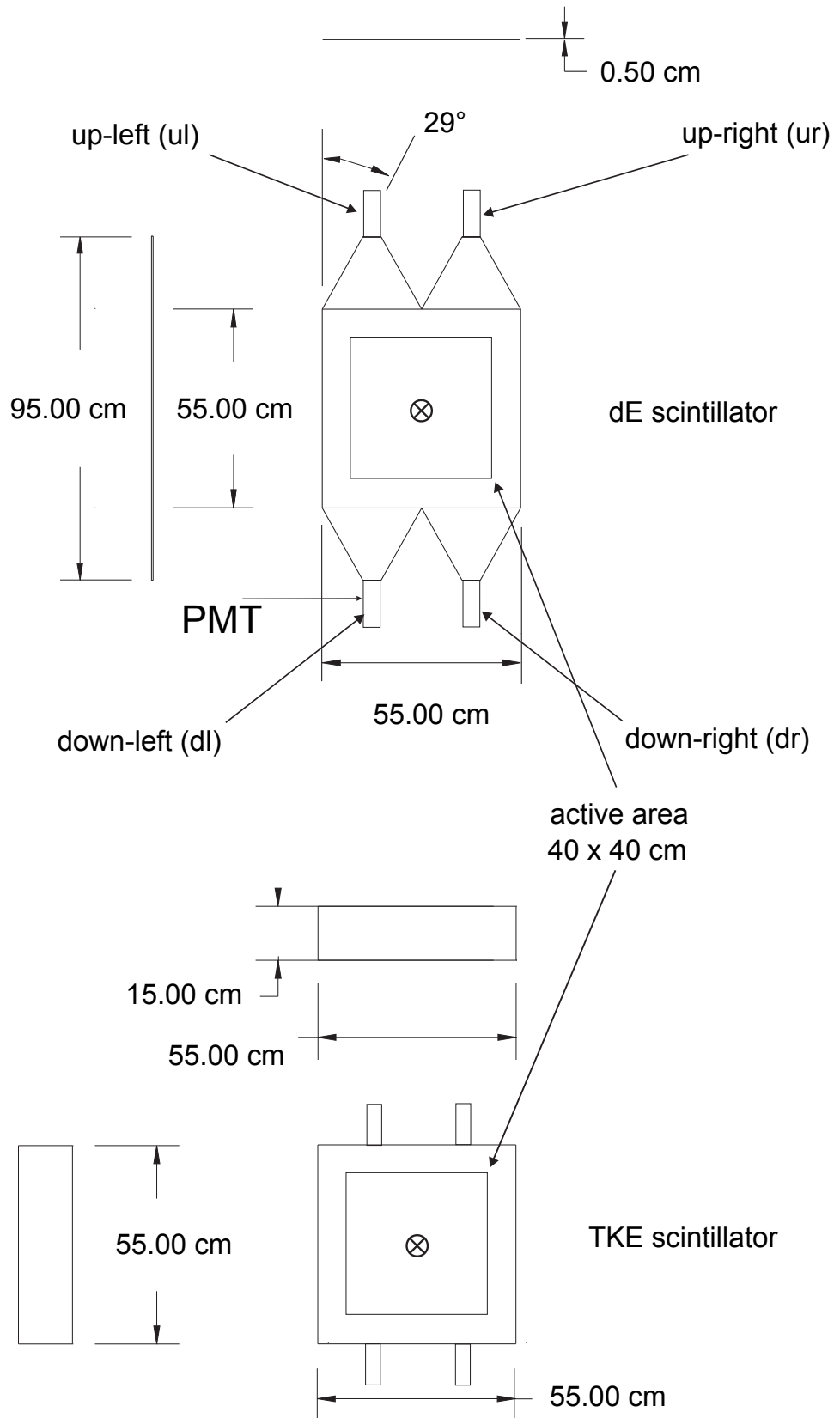


Figure 3.9: dE and TKE scintillators where the beam direction is into the page.

their position with respect to the beam direction designated up-left (ul), down-left (dl), up-right (ur), and down-right (dr).

3.3.5 MoNA

MoNA, the Modular Neutron Array, is designed to detect high-energy neutrons with high detection efficiency and consists of 144 scintillators arranged in 9 layers of 16 detector modules [35,36]. Each module has dimension of 2 m by 0.1 m by 0.1 m. MoNA was placed at a distance of 817(2) cm from the reaction target. Neutrons scatter off protons or carbon of the scintillator producing light. The light was collected at the end of each module with a light guide and a PMT. The energy of the neutrons was calculated by the time-of-flight from the timing detector in front of the target to a module. The angle was calculated by measuring the position in MoNA. The horizontal (x) position was reconstructed by measuring the time difference of the signals from each end of the bar with a position resolution of 7.5 cm. The vertical (y) position and the position along the beam direction (z) were determined from the location of the module giving a position uncertainty of ± 5 cm. The time resolution was < 1 ns.

3.4 Electronics and Data Acquisition

3.4.1 Charged Particle Electronics

Figure 3.10 shows the readout electronics for the beamline and charged particle detectors used in the experiment. The pad signals were digitized with the Front-End-Electronics (FEE), which samples the pad pulse. The time sampling was 200 ns and 25 ns for the PPACs and the CRDCs, respectively. The readout was controlled with three programmable logic modules (Xilinx Logic Module, XLM) one module for both PPACs and one module for each CRDC. The PPAC data were saved in a continuous sampling mode where the trigger indicated that a valid event had occurred. Upon re-

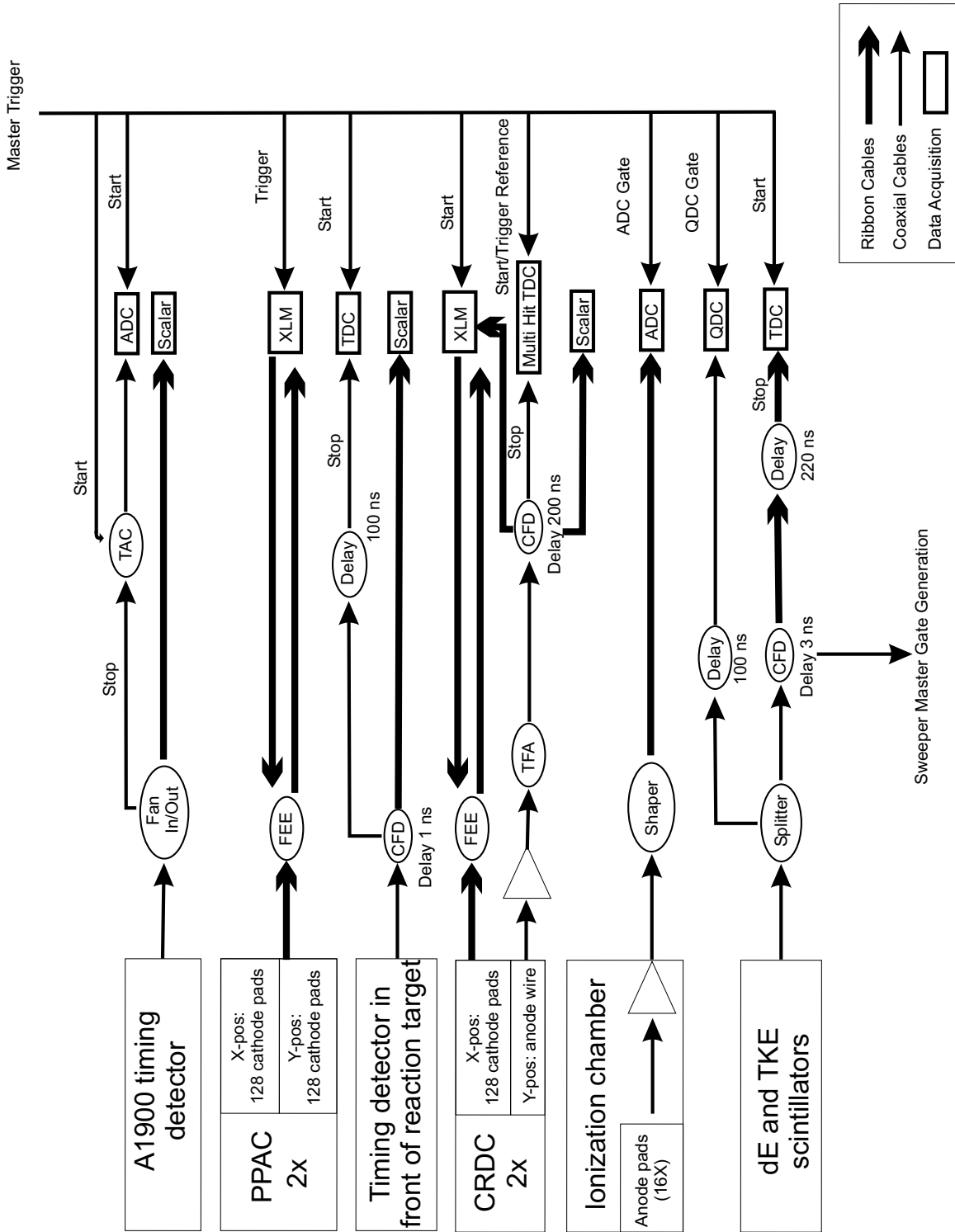


Figure 3.10: Charged particle electronics

ceiving this signal, the XLM searched for data at a specific time range in the past to find the particle signal passing through the detector. The continuous sampling mode was necessary for the PPACs because the anode plate does not provide a quality stop signal. In contrast, the CRDCs recorded data only when the trigger signal was received. Upon receiving this signal, the XLM recorded data until it received a stop signal generated by the anode wire. The data were recorded if the signal was above the hardware threshold set within the XLM.

The anode wire signal was sent through a preamplifier and shaped by a Time Filter Amplifier (TFA). The threshold of the Constant Fraction Discriminator (CFD) was matched to the voltage setting of the anode wire. The CFD internal delay was set to 200 ns. The output of the CFD was split and sent to the Multi-Hit Time-to-Digital Convertor (TDC) and XLM as the stop signal and into a Scaler. The start for the TDC and XLM was the master trigger. The time difference between the anode signal channel and the trigger reference channel was used as a measure of the y-position.

The logic signal of the timing scintillator detector at the end of the A1900 came from the A1900 to experimental vault and was sent to a scaler and used as the stop for the Time-to-Amplitude Convertor (TAC) where the TAC start was the master trigger. The output amplitude of the TAC was proportional to the time between the timing scintillator detector at the end of the A1900 and the master trigger corresponding to the time of the thin scintillator. The signals were digitized in an Analog-to-Digital Convertor (ADC). The timing scintillator in front of the reaction target signal was delayed by approximately 100 ns and sent into a CFD with an internal delay of 3 ns. This signal was split and used for the stop fed into the TDC and the scaler. The master trigger was the common start for the TDC.

The ionization chamber's anode pad signals were amplified by preamplifiers and a shaper. The shaper for each channel was set for maximum gain and the shaping time was 3 μ s. The shaped signals were delivered to a peak sensing ADC. The signal amplitudes were proportional to the energy loss of the charged particles as they

traversed the distance of the chamber.

The dE and TKE scintillators each had four signals. The integrated signal charge from the dE and TKE scintillator correspond to the energy loss of the particles passing through it. The signals for both were split and one was used as a stop for a time measurement of each PMT relative to the master trigger after conversion in a CFD (internal delay of 3 ns) and the other was used for the charge integration of the signal.

The start for the time measurement was the master trigger which was generated using an 'OR' of the four dE scintillator PMTs. The trigger details will be addressed below. The charge integration was performed using a Charge-to-Digital Convertor (QDC) after a delay of 100 ns. This delay was made as small as possible to minimize the signal attenuation due to cable length.

3.4.2 MoNA Electronics

Each MoNA PMT was connected to a QDC to integrate the charge of each signal and a CFD for conversion into logic pulses as an input to a TDC [35, 36, 37]. There were 288 individual channels for the QDCs, CFDs, and TDCs. The CFDs also provided an additional output to be provided to the trigger logic. XLMs were utilized to handle the complicated trigger logic for MoNA. The trigger logic was divided into two parts, level-1 and level-2. Level-1 handled each of the 9 individual layers providing input to scalers, QDC module gate generation and checks that at least one detector module had two PMTs fire. If one detector module had two PMTs fire, the level-2 logic registered a MoNA trigger which started the process of waiting for a sweeper electronics trigger for approximately 200 ns. The level-2 logic generated the computer 'GO', fast clear, and inhibited the CFDs until the detector was ready for another event.

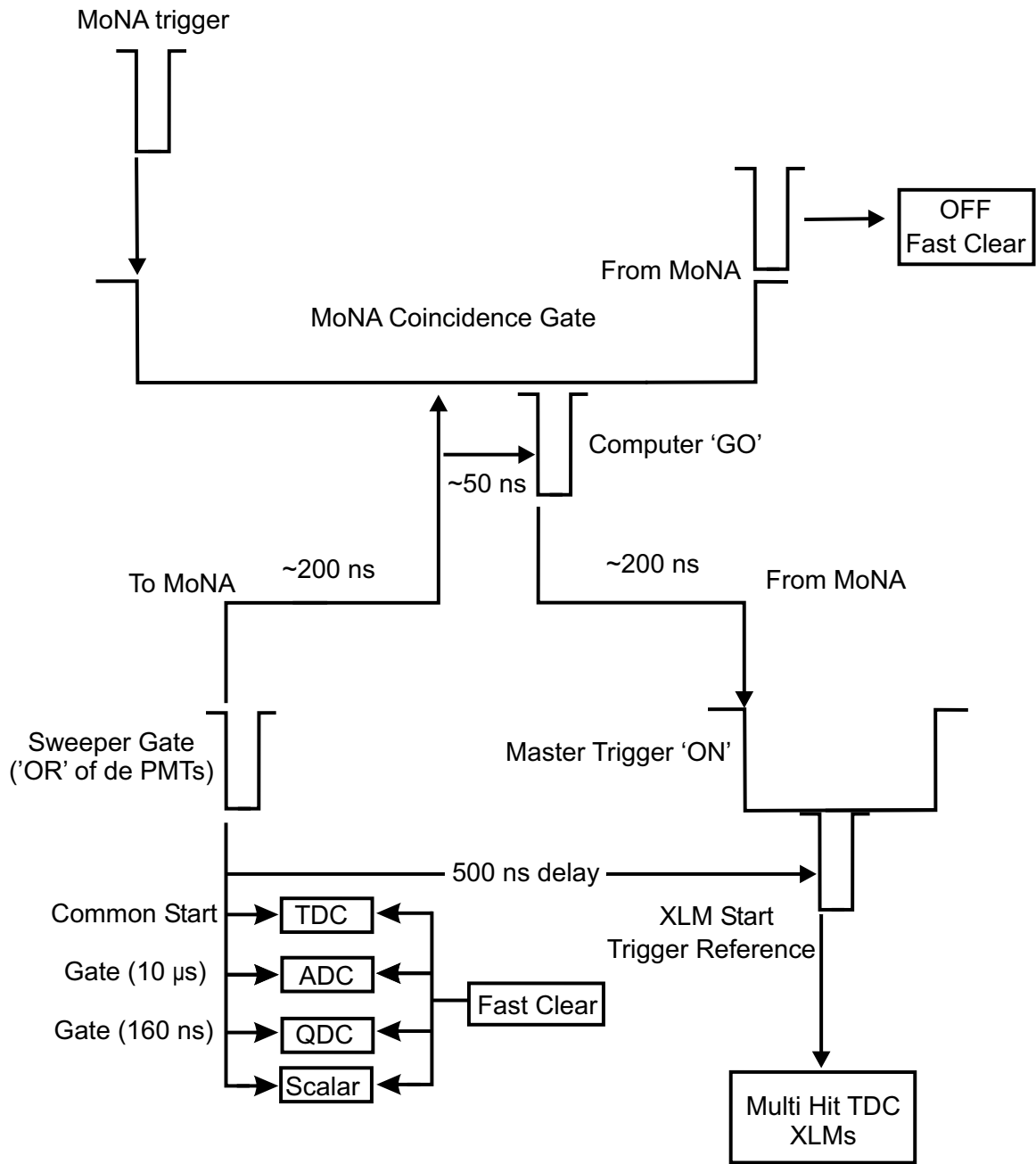


Figure 3.11: Charged particle trigger

3.4.3 Trigger Electronics

The sweeper trigger generated by the 'OR' of the four thin scintillator PMTs was sent to the MoNA trigger logic for processing, a scaler, and also generated several gates and starts, as shown in Figure 3.11. If the MoNA level-2 logic received a sweeper gate within the MoNA coincidence gate, the computer 'GO' and master trigger 'ON' conditions were set. If no sweeper gate was generated within the coincidence gate a fast clear was sent to all the QDCs and TDCs of MoNA as well as the TDC, QDC, and ADC of the sweeper electronics. After a fast clear, a data ready state was achieved within approximately 700 ns. For a valid event, the master trigger 'ON' was received after approximately 450 ns. The master trigger was included in an 'AND' gate with a delayed sweeper master gate. This start was then used for all the sweeper XLMs and the Multi-Hit TDC. The triggering was handled in this way for the Multi-Hit TDC and XLMs because they had no fast clear capability.

The online analysis was performed with SpecTcl [38] and the data were recorded on DLT tape for storage and offline analysis.

Chapter 4

Analysis

4.1 Overview

The data analysis was performed off-line using Physics Analysis Workstation (PAW) [39] and energy loss and kinematic calculations were performed with LISE++ [40]. Calibration runs before the experiment as well as off-line calibrations were necessary for the detectors. After calibrations of the charged particle and beamline tracking detectors, neutron and charged fragment reconstruction, the analysis of the data was performed.

All TDCs were calibrated with evenly spaced timing pulses from a time calibrator. Mask runs for the CRDCs and PPACs were performed to determine the x,y positions. The energy losses from the ionization chamber, dE scintillator, and energy deposited after the other detectors in the TKE scintillator were calibrated and position corrected using the position information of the CRDCs. The charged fragment time-of-flight was corrected using measured positions and angles to provide the isotopic separation. After these steps were performed, gates on incoming ^{26}Ne secondary beam and different isotopes were possible.

Cosmic ray data were recorded to calibrate the position along the length of the bars of MoNA. A thick target was used to stop the secondary beam producing γ -rays

as well as neutrons, which determined the absolute offset of the time-of-flight for all of MoNA.

The Sweeper Magnet’s magnetic field was carefully mapped. Ion-optical transfer matrices were calculated for the Sweeper Magnet and the quadrupole triplet with COSY Infinity [41]. Data runs with discrete Sweeper Magnet settings using secondary beam were performed to verify the ion-optical transfer matrices.

Finally momentum vectors of the neutrons and charged particles at the reaction target were reconstructed and isotope gates of ^{21}O , ^{22}O , and ^{23}O were used to reconstruct the decay $^{22}\text{O}^* \rightarrow ^{21}\text{O} + \text{n}$, $^{23}\text{O}^* \rightarrow ^{22}\text{O} + \text{n}$ and $^{24}\text{O}^* \rightarrow ^{23}\text{O} + \text{n}$, respectively.

4.2 Secondary Beam Particle Identification

Figure 4.1 shows the secondary beam produced from the A1900 Fragment Separator. The RF time was the cyclotron frequency relative to the electronic trigger of the A1900 data acquisition system. The secondary beam particle of interest was ^{26}Ne , which was the second highest isotope produced for both the 3% and 1% momentum acceptance settings. The main contaminants were ^{29}Mg , $^{27,28}\text{Na}$, ^{24}F and lighter particles produced mainly in the wedge at the dispersive focal plane of the A1900 fragment separator. To reduce the contaminants, the A1900 extended focal plane slits (XFP) were placed at ± 10 mm, shown in Figure 4.2. Table 4.1 shows the change of the rate of secondary beam contaminants without and with the extended focal plane slits. The purity for ^{26}Ne was increased from approximately 13.5% without extended focal plane slits to approximately 93.2% with extended focal plane slits.

The secondary beam time-of-flight spectrum was calculated based on the calibrated times of the timing detector at the exit of the A1900 and the timing detector in front of the reaction target. The time offset was determined with the knowledge of the expected central magnetic rigidity ($B\rho$) for ^{26}Ne of 3.56931 Tm and the distance

Table 4.1: Isotope to total ratio from the production in the A1900 fragment separator without and with the extended focal plane slits.

Isotope	no slits	slits
^{27}Na	52.9%	0.6%
^{26}Ne	13.5%	93.2%
^{29}Mg	10.6%	-
^{28}Na	2.0%	-
^{24}F	0.8%	-

between the scintillators (36.68 m, see Figure 3.5). Figure 4.3 shows the calibrated beam time-of-flight spectrum with the identification of ^{26}Ne and ^{27}Na along with light fragments. ^{26}Ne was clearly separated and a gate around it was applied before calibrating any other detector.

4.3 CRDC Calibration

The position calibration of the CRDC in the dispersive plane (x -position) was determined by the pad pitch 2.54 mm. The position calibration in the non-dispersive plane (y -position) was determined by sweeping beam across the detector with a mask placed in front of it with holes drilled at known positions (see Figure 4.4). The masks were 45 mm upstream from each detector, which required an iterative process using the angle calculated from the CRDCs to calibrate the y -position for each detector. This was approximately a 3% and less than 1% effect for the slope used for the y -calibration of CRDC1 and CRDC2, respectively. In addition, the y -position drift over time (as shown in Figure 4.5) was taken into account. The y -position drift was approximately a 3% change to the slope used in the y -calibration for both CRDCs.

The distribution of charge on the pads of the CRDC was used to calculate the x -position. The pad data were read out every 25 ns. (see Section 3.4.1). The total charge on each pad was then calculated from the sum of all time intervals after the subtraction of an electronic offset. All pads were calibrated to the same gain. The

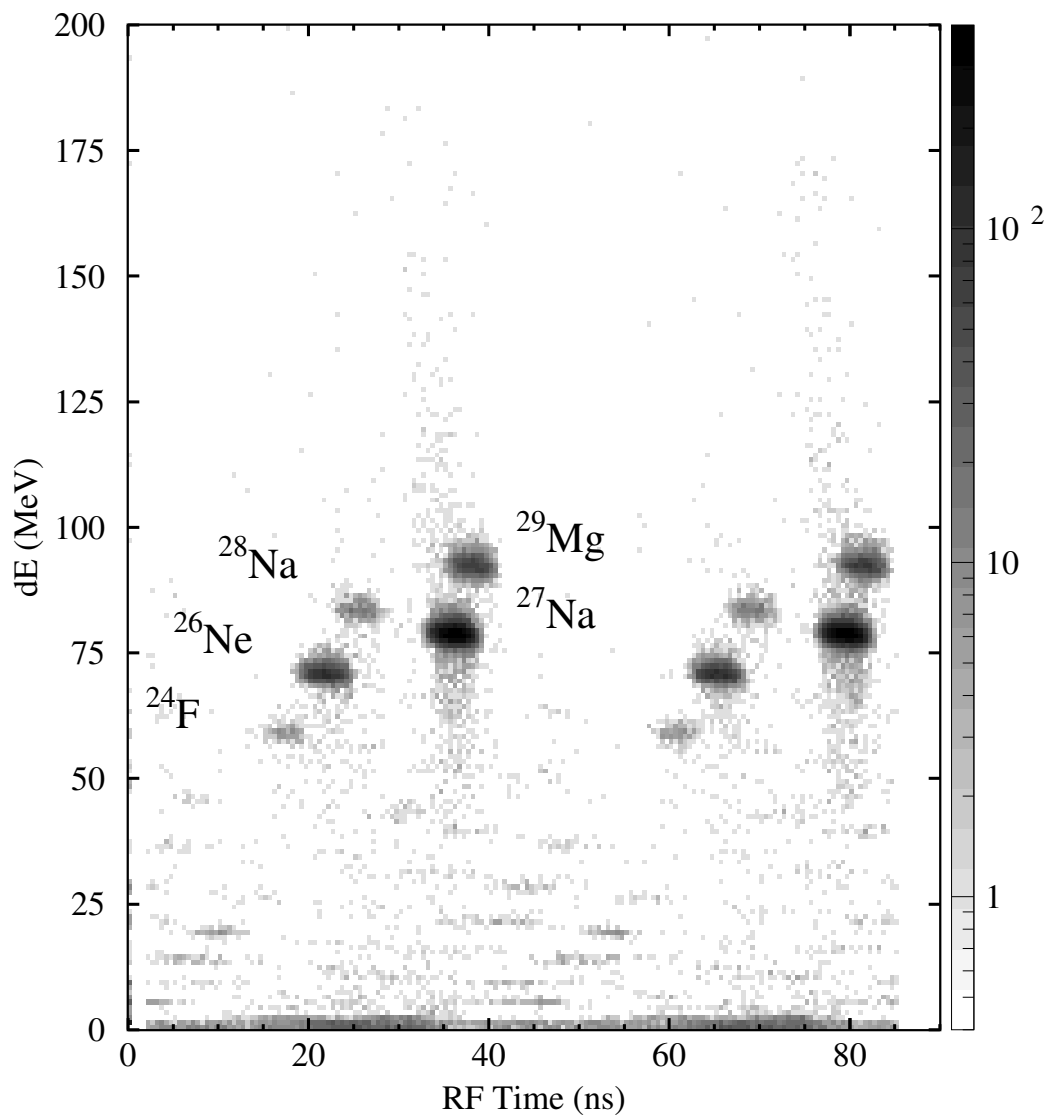


Figure 4.1: Energy loss (dE) versus RF time.

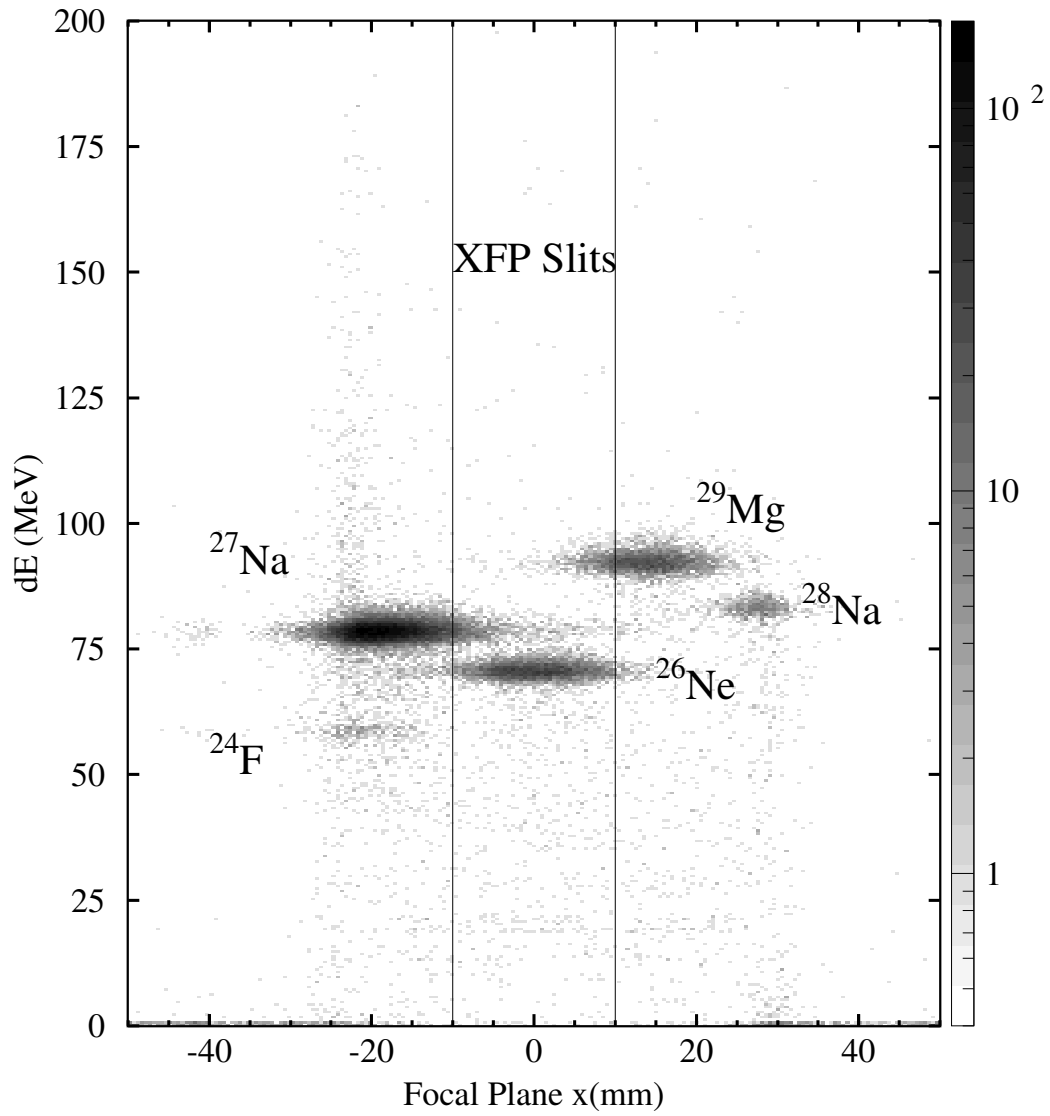


Figure 4.2: Energy loss versus the A1900 Fragment Separator focal plane dispersive position.

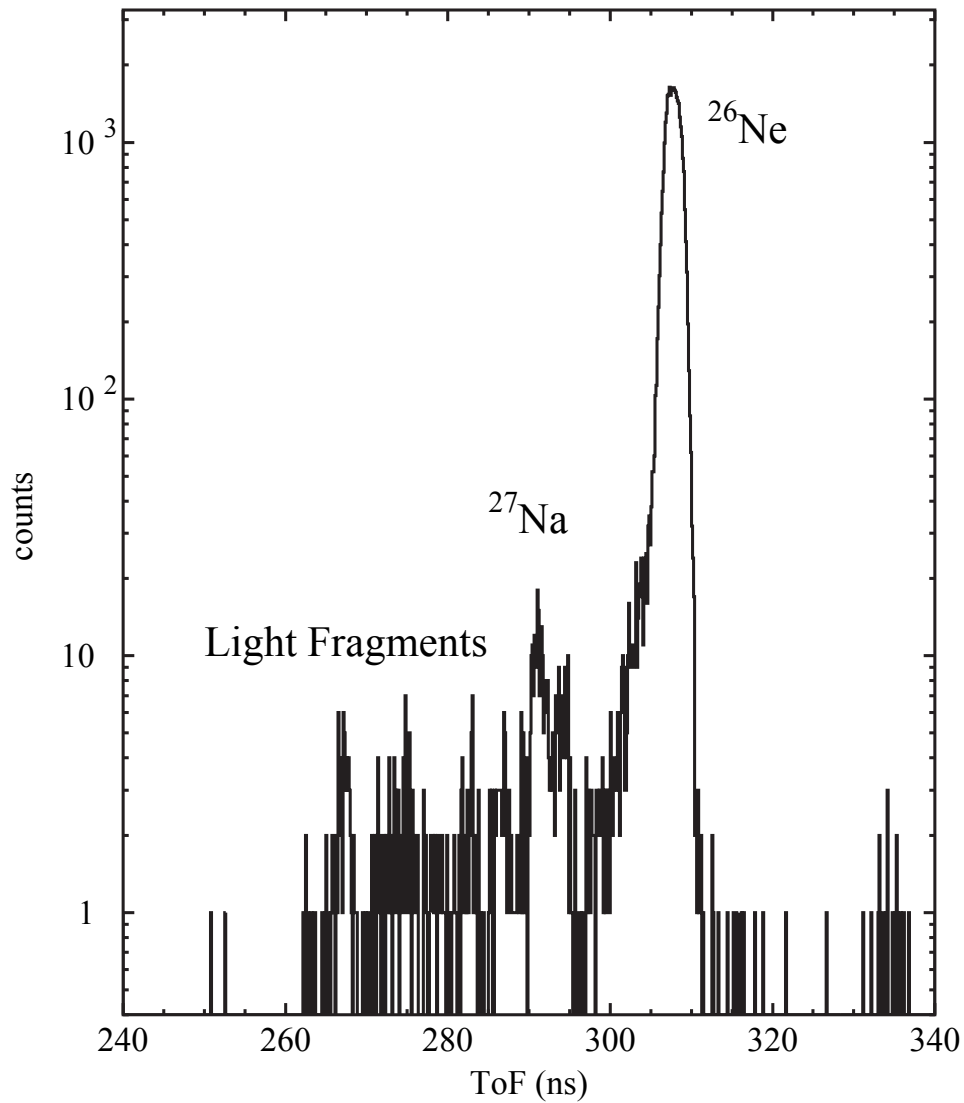


Figure 4.3: Time-of-Flight (ToF) secondary beam identification plot

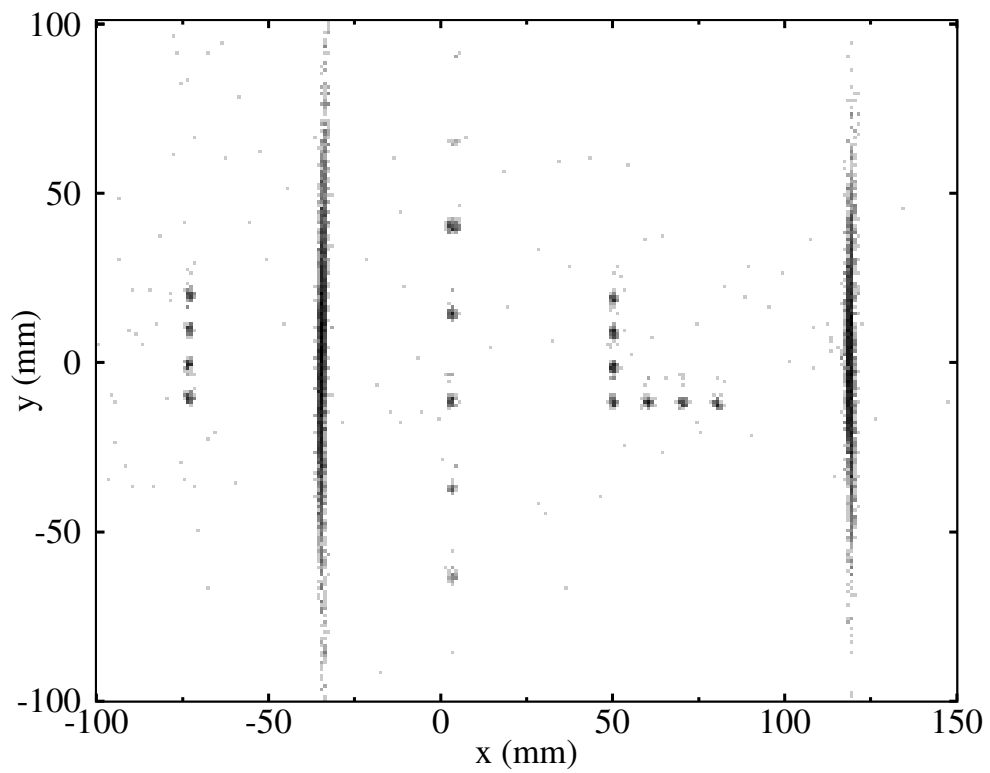


Figure 4.4: y -position versus x -position for the mask of CRDC2

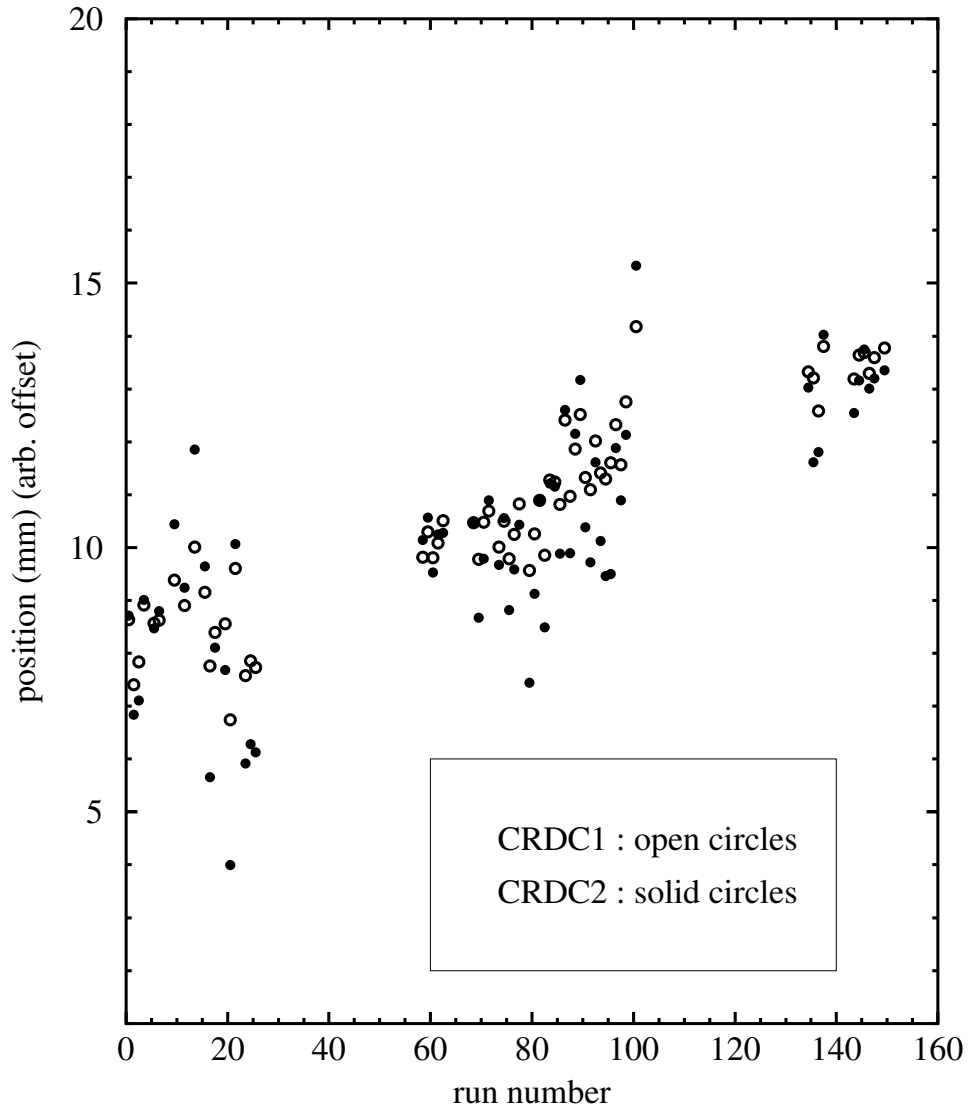


Figure 4.5: Mean y-position of both CRDCs versus run number for all charged fragments in coincidence with incoming ^{26}Ne secondary beam. The arbitrary offset is for display purposes.

x -position was calculated by taking the mean μ_{pad} of the approximately gaussian distribution of charge on the 128 pads:

$$\mu_{\text{pad}} = \frac{\sum_{i=0}^{127} i q_i}{\sum_{i=0}^{127} q_i} \quad (4.1)$$

Similarly the total charge summed for the same time intervals from different pads was also approximately gaussian distributed. Thus distributions along sample (time interval) or pad number were characterized by calculating a σ_{sample} or σ_{pad} using:

$$\sigma = \sqrt{\mu_2 - \mu_1^2} \quad (4.2)$$

where μ_2 and μ_1 were calculated using:

$$\mu_j = \frac{\sum_i i^j q_i}{\sum_i q_i} \quad (4.3)$$

where q_i is the total charge for a pad or a sample.

Cuts placed on σ_{sample} and σ_{pad} ensured that the distribution of charge along pad and sample number were of similar width, event by event. The independent parameter of total integrated charge was chosen to demonstrate the consistency after the cuts, where similar events should have similar total charges. The spectra for each CRDC shown in Figure 4.6 show a peak around a mean of three pads for σ_{pad} . The cuts shown in Figure 4.6 were applied to the σ_{sample} spectra shown in Figure 4.7 for each CRDC separately. Similarly, the σ_{sample} spectrum for each CRDC show a peak around a mean of three samples. Cuts on the σ_{sample} spectra were applied to the total integrated charge spectrum for each CRDC shown in Figure 4.8. The distributions for each CRDC were approximately the same which indicates that the cuts were effective. The events shown in the total integrated charge spectra shown in Figure 4.8 were used for the rest of the data analysis.

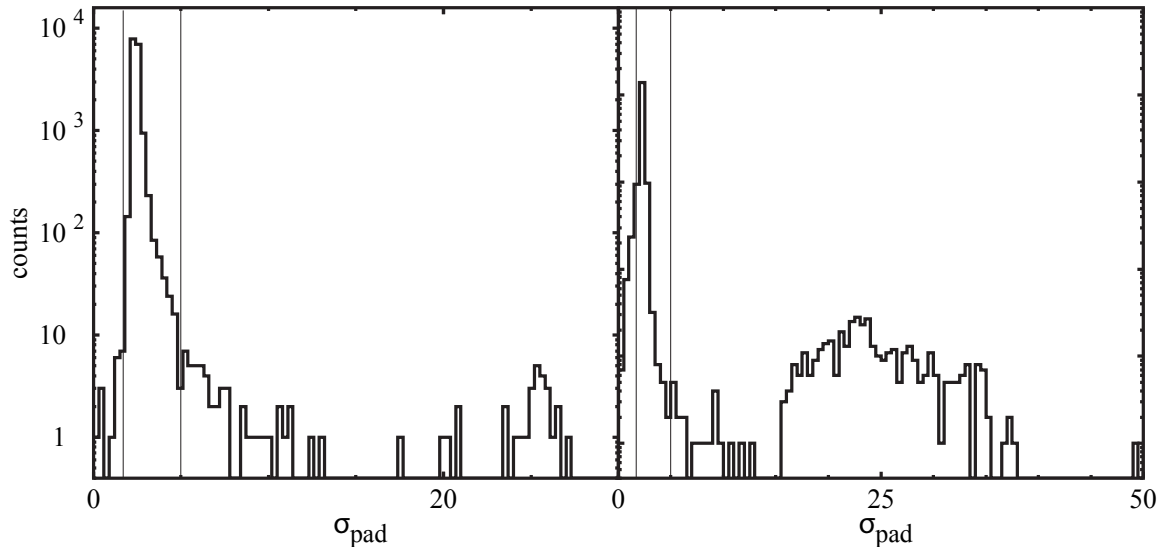


Figure 4.6: Pad width σ_{pad} for CRDC1 (left) and CRDC2 (right). The events between the lines in each spectrum were accepted for the next cut for each CRDC separately.

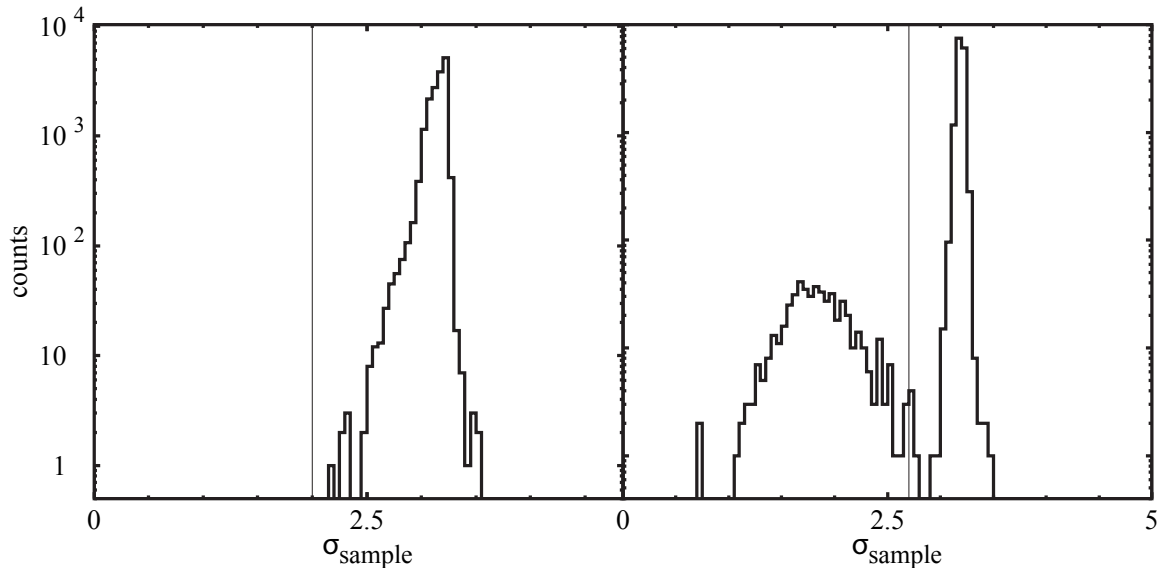


Figure 4.7: Sample width σ_{sample} for CRDC1 (left) and CRDC2 (right). The events to the right of the lines in each spectrum were accepted for each CRDC separately.

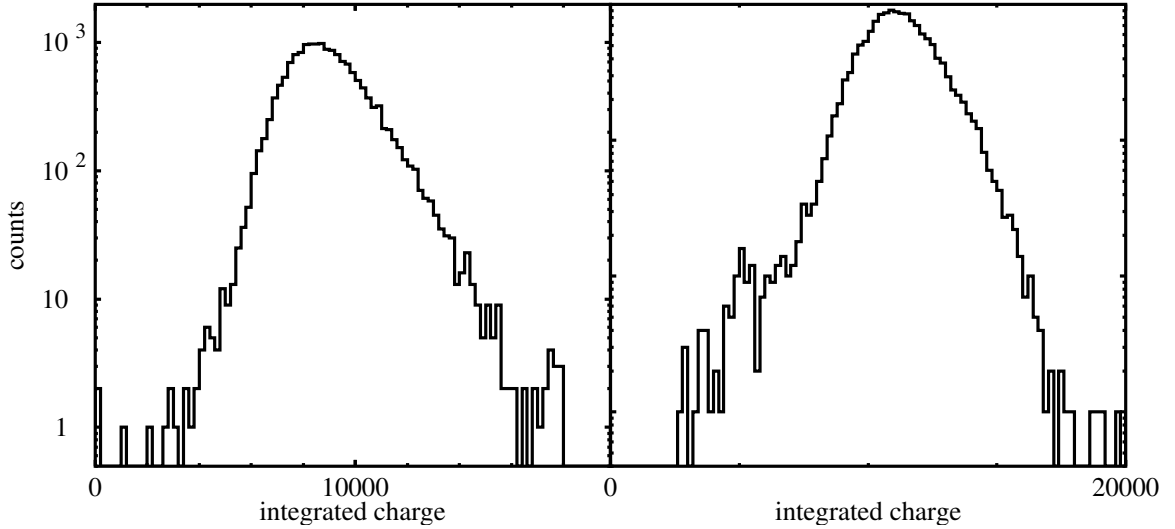


Figure 4.8: Integrated charge for CRDC1 (left) and CRDC2 (right).

4.4 PPAC Calibration

The calibrations for the PPACs used the pad pitch of 1.27 mm in both directions. The distribution of charge on the pads of the PPAC were used to calculate the x and y -positions with Equation 4.1. The pad data were digitized with a time sampling period of 250 ns (see Section 3.4.1). The total charge on each pad was then calculated from the sum of all time intervals after the subtraction of an electronic offset. The pads along each direction were calibrated to the same gain.

The same quality parameters for the CRDC pads were constructed for the PPAC pads. However, the parameters were not as useful because the PPAC is an avalanche detector which produces a large range of induced charge on the pads. The spectra shown in Figure 4.9 show the large integrated charge distributions for each direction x_{PPAC1} , y_{PPAC1} , x_{PPAC2} , and y_{PPAC2} . The spectra in Figures 4.10 and 4.11 show the quality parameters of σ_{sample} and σ_{pad} , respectively. Each PPAC direction x_{PPAC1} , y_{PPAC1} , x_{PPAC2} , and y_{PPAC2} show wide distributions of σ_{sample} and σ_{pad} . Due to the wide distributions in the parameters, determining reasonable cuts was difficult. The one cut that was employed was on σ_{pad} for values near zero. This cut eliminated events where only one pad had a digitized charge value resulting in spikes on the position

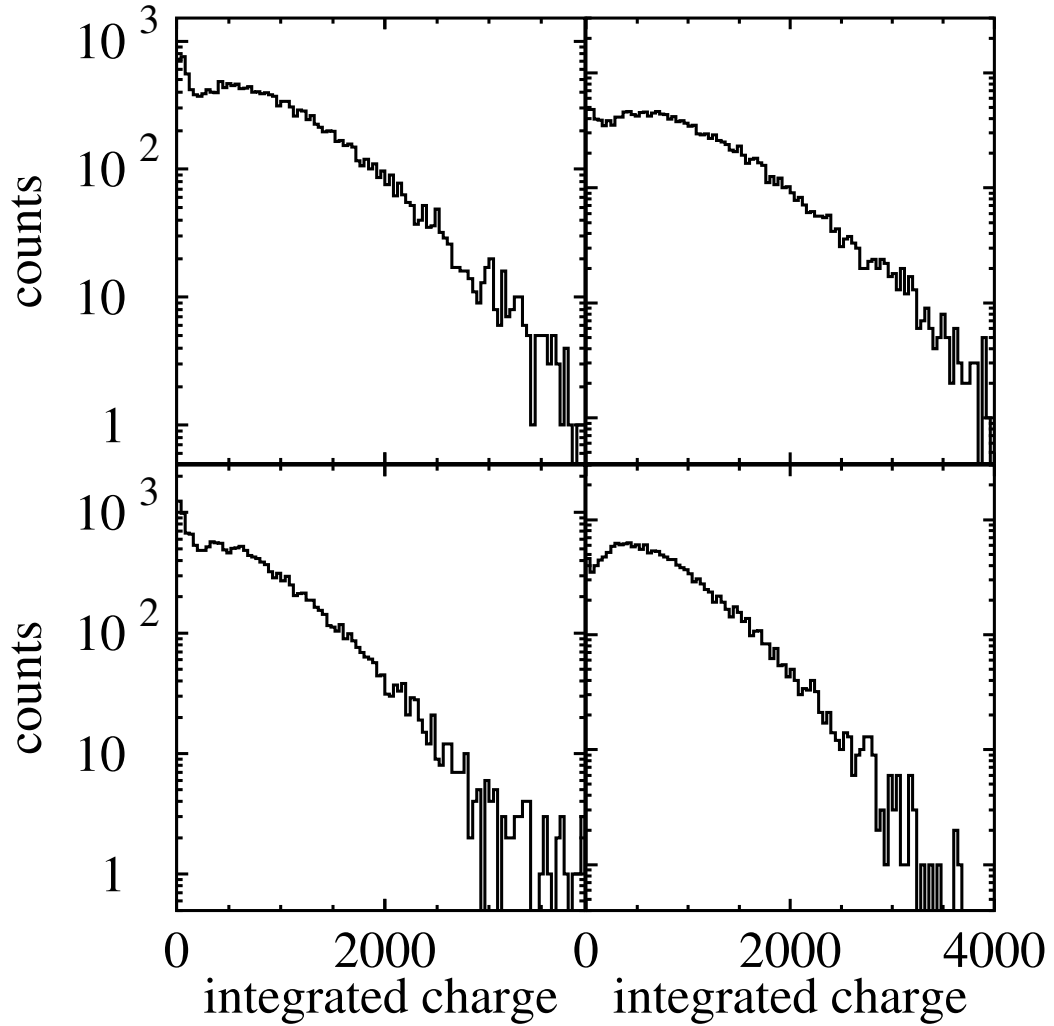


Figure 4.9: Integrated charge for x_{PPAC1} (upper-left), y_{PPAC1} (upper-right), x_{PPAC2} (lower-left), y_{PPAC2} (lower-right).

spectra.

4.5 Element Identification

Element separation was achieved by using the measured energy loss which depends on the charge (q) of the nucleus ([42] pg. 24). Unambiguous element separation required both properly calibrated ionization chamber and dE scintillator energy losses.

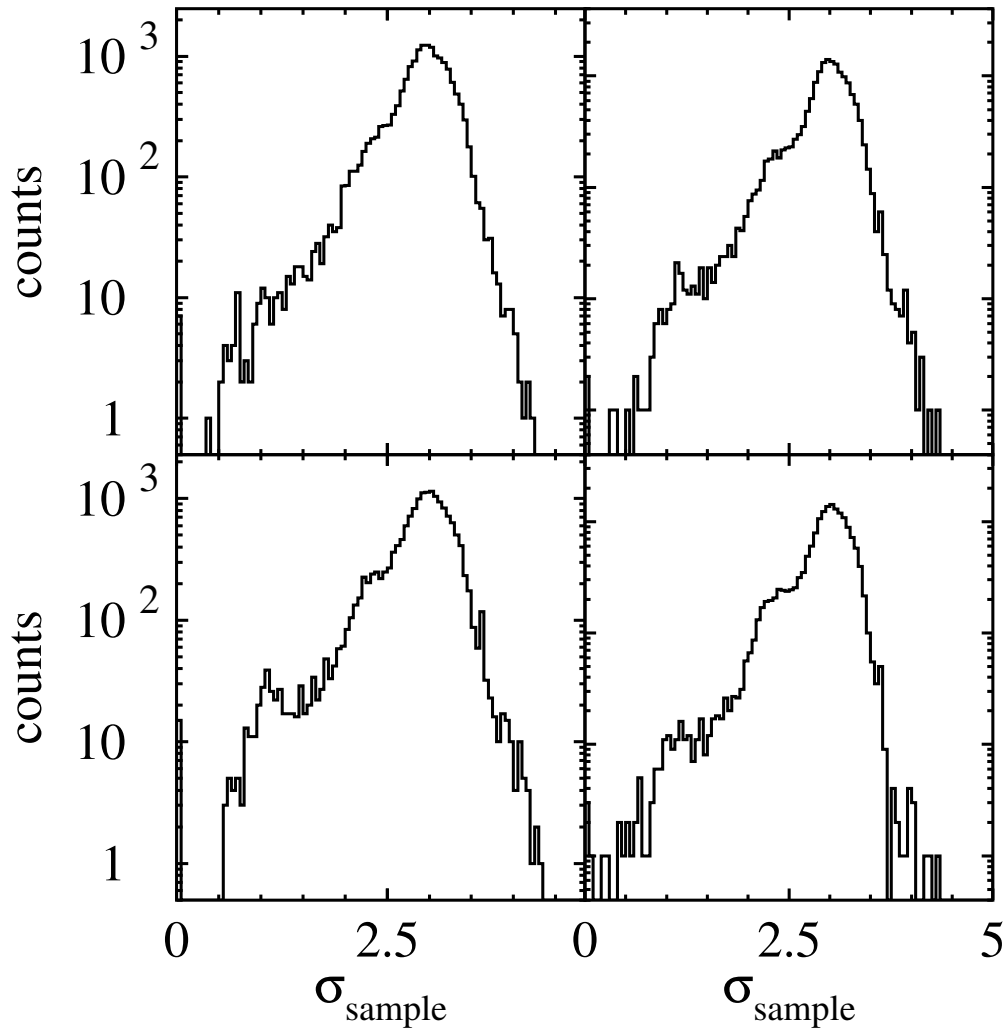


Figure 4.10: Sample width σ_{sample} for x_{PPAC1} (upper-left), y_{PPAC1} (upper-right), x_{PPAC2} (lower-left), y_{PPAC2} (lower-right).

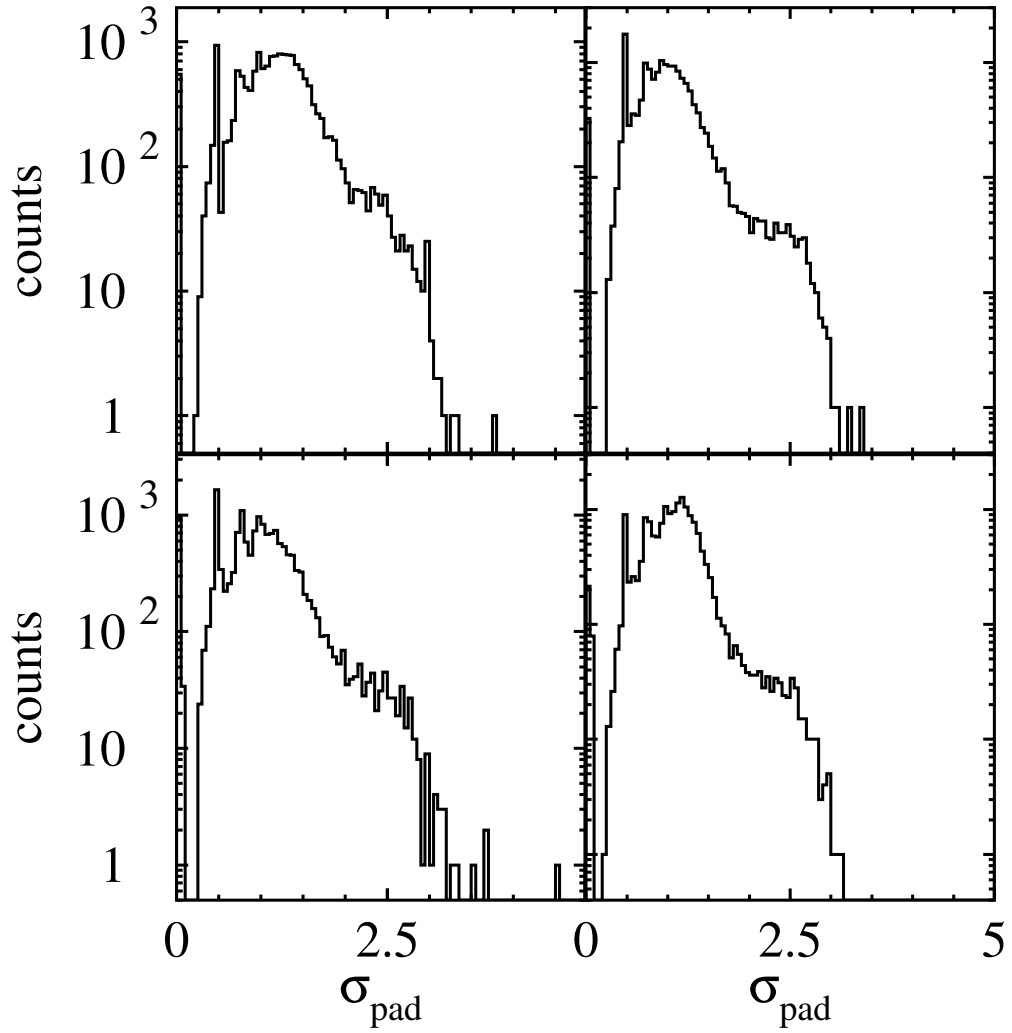


Figure 4.11: Pad width σ_{pad} for x_{PPAC1} (upper-left), y_{PPAC1} (upper-right), x_{PPAC2} (lower-left), y_{PPAC2} (lower-right).

4.5.1 Ionization Chamber Calibration

The calculation and calibration of the energy loss in MeV for the ionization chamber was performed using:

$$\Delta E(\text{MeV}) = \sum_{i=2}^{15} (q_i m_i(t) + b_i) E_{cal} c(y) \quad (4.4)$$

The summation excluded the first and last pads (i) because of incomplete charge (q_i) collection near the upstream and downstream drift foils. The correction factor variables that contained the gain match and drift over time ($m_i(t)$ and b_i) were determined for each pad (see Figure 4.12). The overall energy calibration for the detector (E_{cal}) was determined with a secondary beam tune that included ^{26}Ne and ^{23}O . The spectrum shown in Figure 4.13 shows the y -direction dependence (y_{dE}), which was corrected ($c(y)$) to be used for the final element separation. The y -position spectrum shown in Figure 4.13 was calculated in the non-dispersive direction at the dE scintillator.

4.5.2 dE Scintillator Calibration

The corrections necessary to obtain the energy loss from the dE scintillator were due to light attenuation in the detector. The PMT raw energy signals were corrected for drifts of the signals with time. The two left side PMTs digitized charge signals were gain matched to each other with beam particles interacting at the spatial center of the scintillator. The left side PMT average charge after gain matching and the down-right PMT charges were position corrected for light attenuation in the scintillator. The up-right PMT charge was not used because the PMT did not work. The parameters for the position dependent correction were calculated at the dE scintillator dispersive (x_{dE}) and non-dispersive (y_{dE}) directions, from the positions measured by the CRDCs. The position dependent attenuation was different for each PMT depending on the mounted position on the scintillator (see Figure 3.9). The left side PMTs correspond

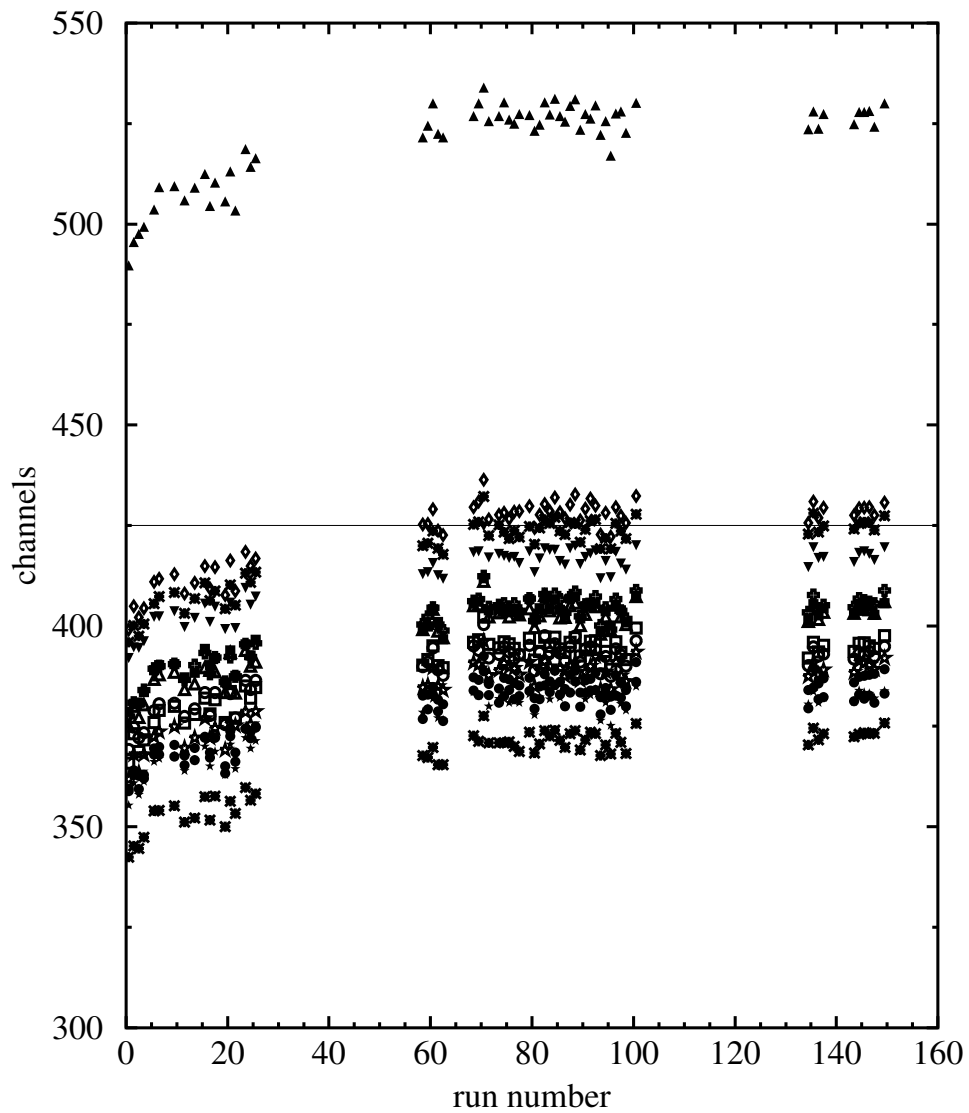


Figure 4.12: Ionization chamber pad peaks versus run number. The symbols represent each pad used from the ionization chamber.

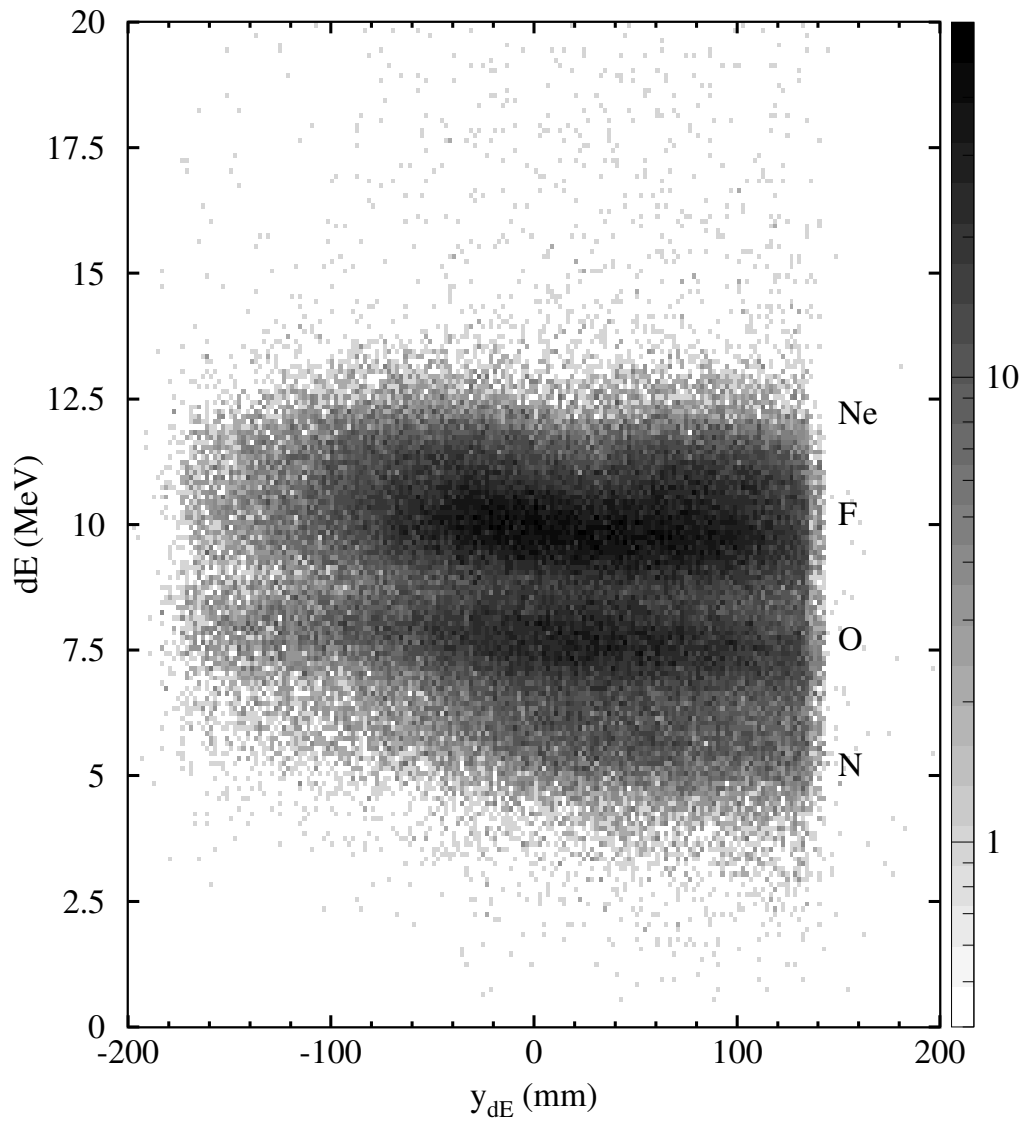


Figure 4.13: Energy loss in ionization chamber versus vertical position at the dE scintillator (y_{dE}).

to positive x_{dE} and the right side PMTs to negative x_{dE} . The y_{dE} parameter is positive for up PMTs and negative for down PMTs. The corrections were performed with the production data. To show the position dependence, the spectra before and after correction are shown in Figures 4.14 and 4.15 for the down-right PMT. The position dependence was corrected for the y_{dE} position shown in Figure 4.14 and then the x_{dE} position shown in Figure 4.15. The y_{dE} correction was larger than the x_{dE} correction for the down-right PMT charge because the particles in the experiment were located at negative x_{dE} position. After correcting for the position dependence, the left side PMT average and down-right PMT charges were averaged together to generate the final spectrum shown in Figure 4.16.

The spectrum shown in Figure 4.17 shows the final element separation using the ionization chamber and dE scintillator energy losses. The cut shown in Figure 4.17 was used to identify the oxygen elements.

4.6 Isotopic Identification

The two parameters that provide isotopic separation are a corrected Time-of-Flight (ToF) and energy deposited in the TKE scintillator. The ToF was the dominant parameter to obtain isotopic separation and was corrected for several measured parameters before and after the Sweeper Magnet.

4.6.1 TKE Scintillator Calibration

The up-right and down-left PMTs of the TKE scintillator worked properly and these were used to produce the energy deposited spectrum. The PMT spectra were corrected for drifts over time. The position correction for light attenuation as a function of x_{dE} and y_{dE} was performed in two iterations in the same way as the dE scintillator. Figure 4.18 shows the final energy loss plot hinting that there are two oxygen isotopes.

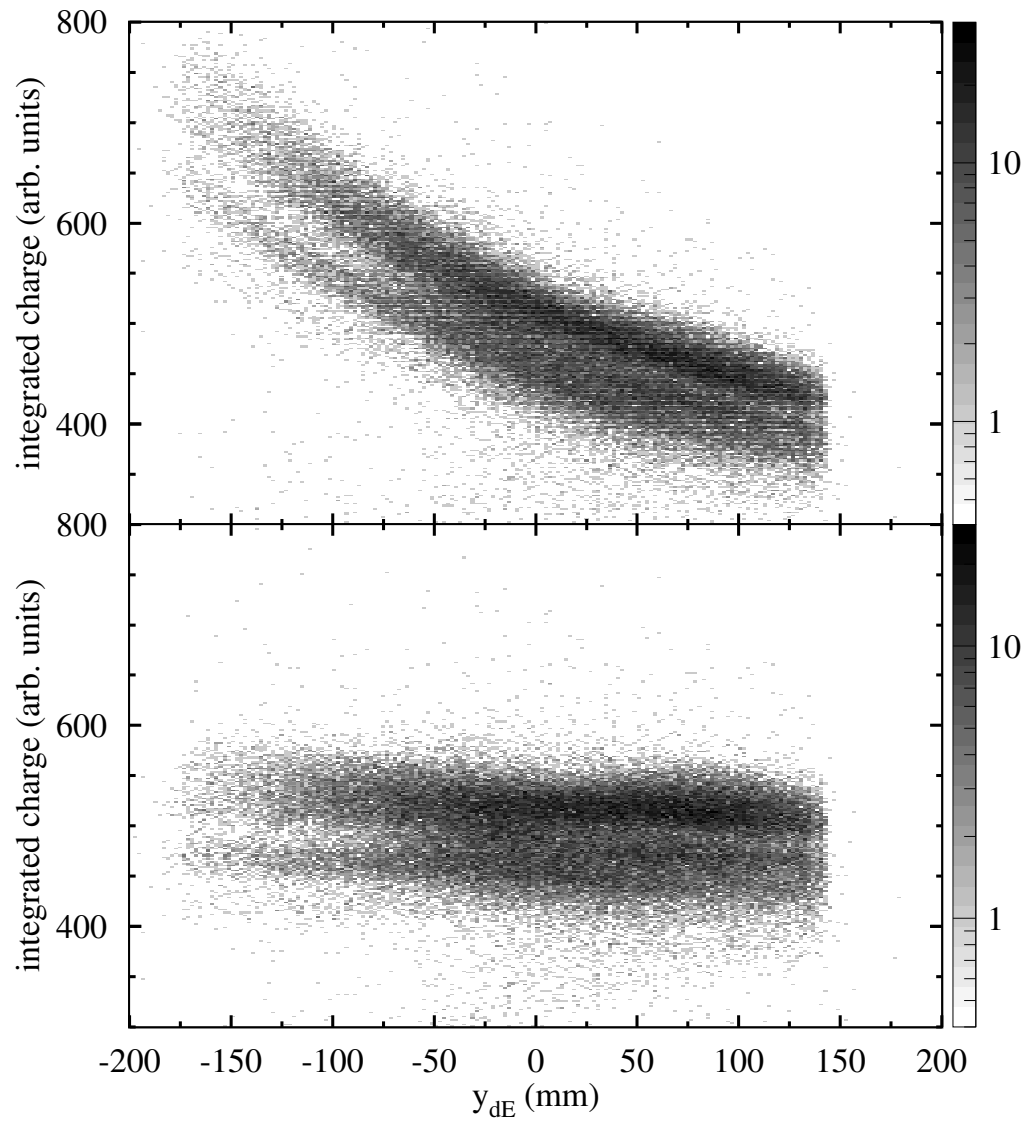


Figure 4.14: Down-right PMT integrated charge versus y_{dE} . No position correction (top) and with position correction (bottom) using the y_{dE} parameter.

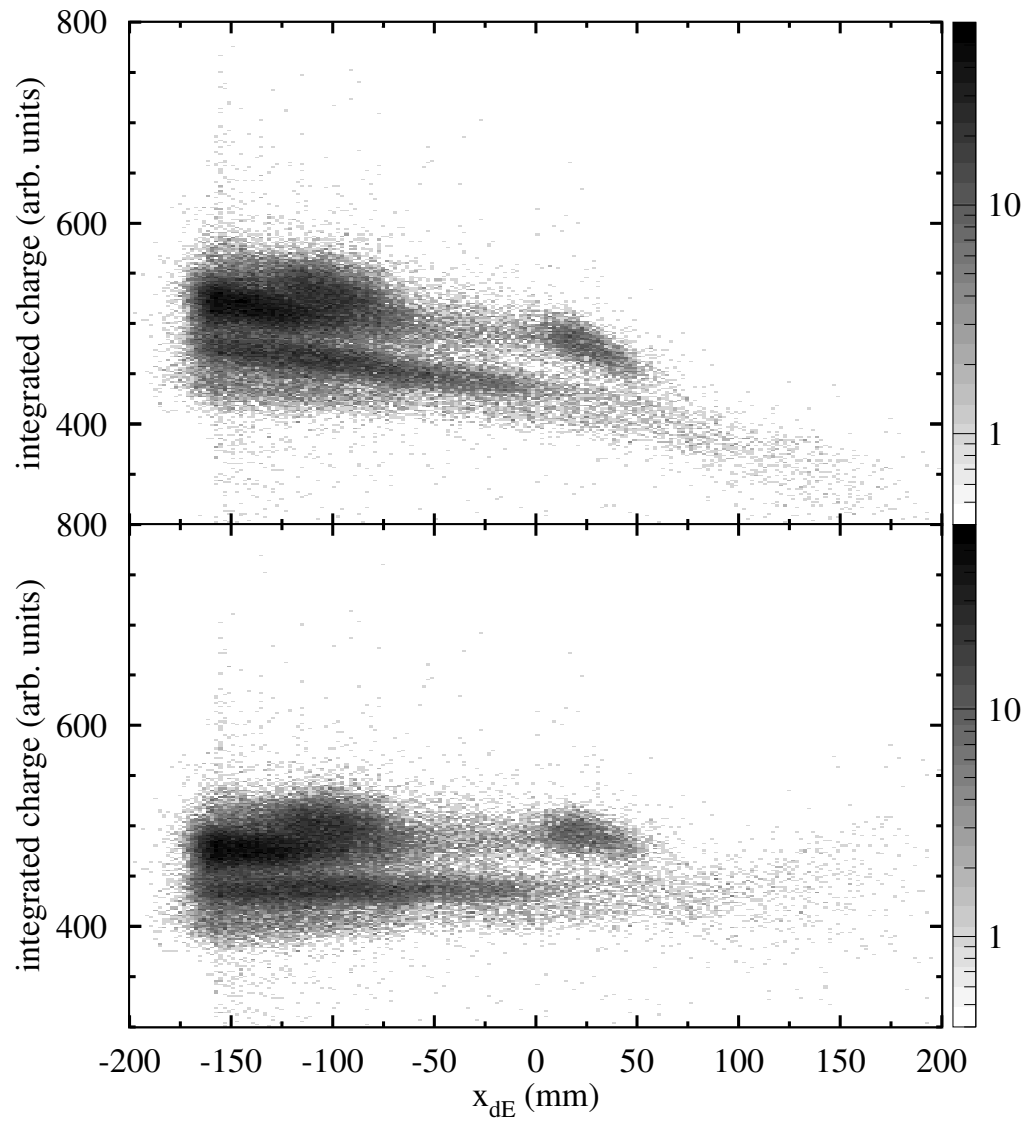


Figure 4.15: Down-right PMT integrated charge versus x_{dE} . No position correction (top) and with position correction (bottom) using the x_{dE} parameter.

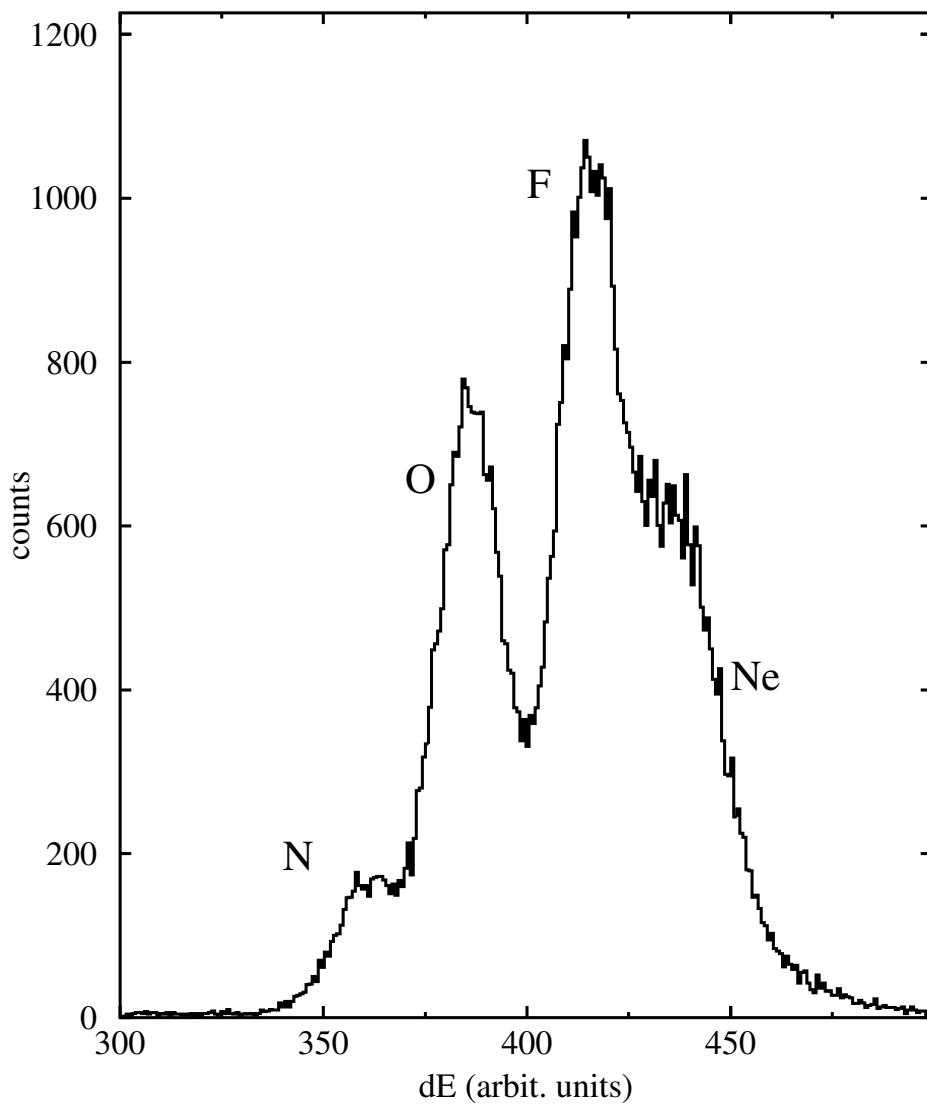


Figure 4.16: dE scintillator energy loss

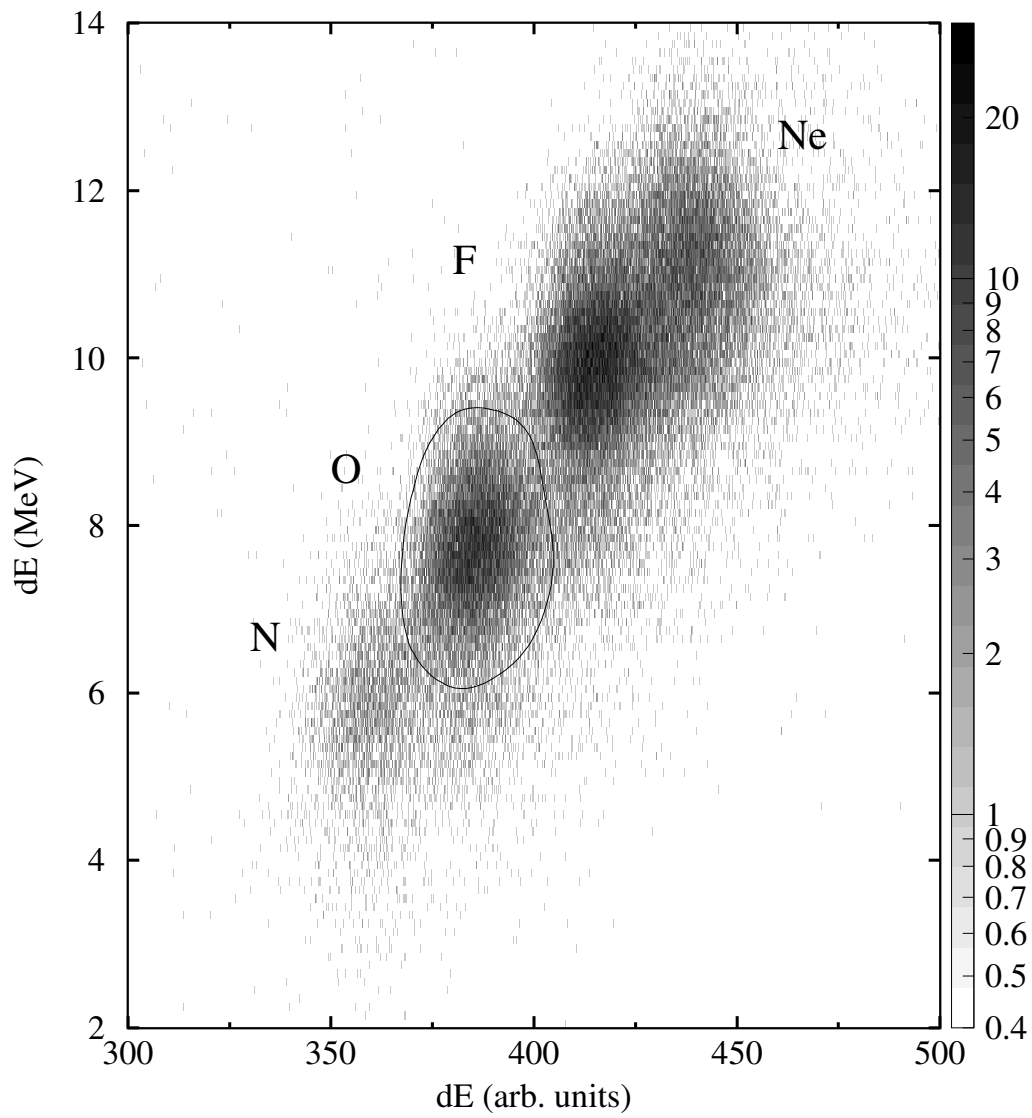


Figure 4.17: Energy loss (ionization chamber) versus energy loss (dE scintillator). The cut for oxygen isotopes is shown by the curve.

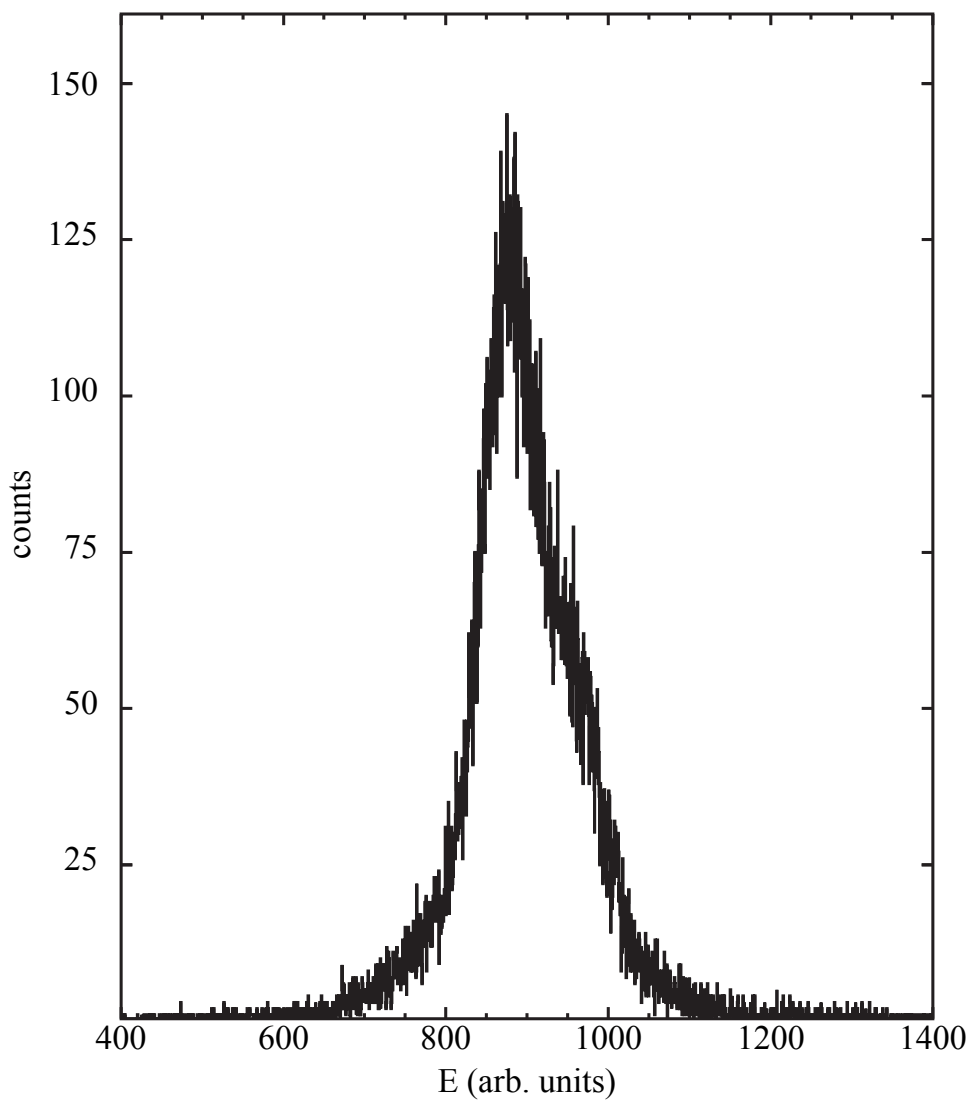


Figure 4.18: TKE scintillator energy loss (arbit. units)

4.6.2 Time-of-Flight Corrections

The ToF for the charged fragments was constructed as a difference between the calibrated time signals of the timing detector in front of the reaction target and each of the dE scintillator PMTs. Three of the PMTs, down-left, down-right and up-left, were working properly. Down-right was the trigger, resulting in a self triggered spike in its ToF spectrum. The ToF for a given PMT includes the travel time of the particle between the timing detector in front of the reaction target and the dE scintillator, and the light travel time from the position that the particle entered the dE scintillator to the location of the PMT. Therefore the first correction for the ToF construction was to correct for the light travel time in the dE scintillator relative to each PMT. The distance to each PMT (d_i) was assumed to be a straight line:

$$d_i = \sqrt{((x_{dE} - x_i)^2 + (y_{dE} - y_i)^2)} \quad (4.5)$$

where (x_{dE}, y_{dE}) are the positions calculated at the dE scintillator. The index i represents each PMT with positions of (x_i, y_i) of (in mm) (137.5, 275), (137.5, -275), (-137.5, 275), and (-137.5, -275), for up-left (ul), down-left (dl), up-right (ur), and down-right (dr), respectively. The speed of light in BC-404 scintillator with an index of refraction 1.58 is given by:

$$t_i = d_i \frac{1.58}{c} \quad (4.6)$$

The final ToF for a given PMT used its calibrated time with the light travel time subtracted from it. The time average of the dr and dl PMTs used the travel time subtracted ToFs. The spectrum shown in Figure 4.19 shows the comparison of the t_{dr} and t_{dl} PMT subtracted ToFs. The events between the two parallel lines were used for the next set of ToF corrections. The events outside of the parallel lines come from events where the ToF signal for a given PMT was generated after light reflection within the scintillator. A straight line light travel time correction from the point of

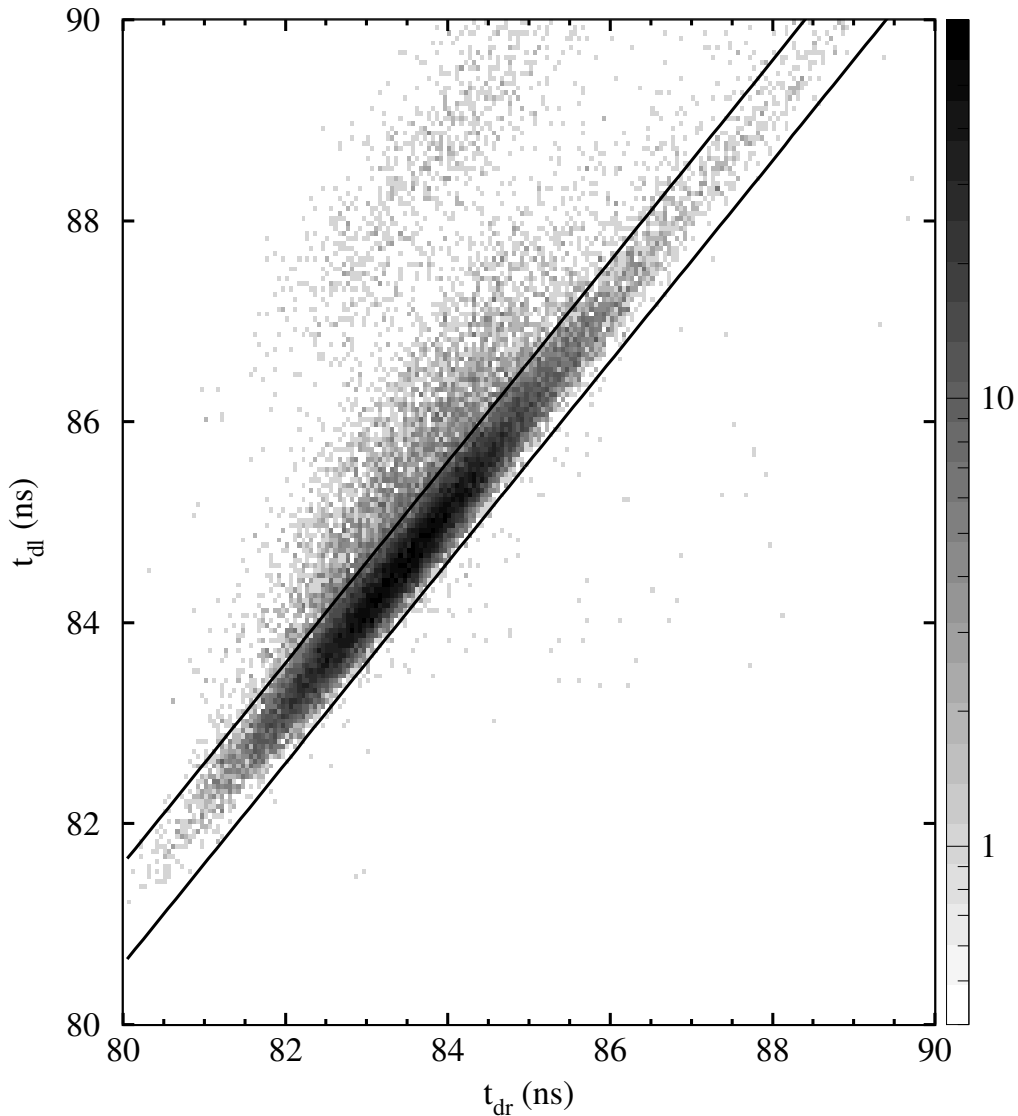


Figure 4.19: ToF of down-left PMT versus down-right PMT after travel time correction.

interaction to the PMT cannot correct for light reflection, so the events outside the parallel lines are not used for subsequent corrections to the average ToF.

The averaged ToF includes particles that are moving at different velocities over varying distances. The exact velocity and distance a particle travels from the reaction target to the dE scintillator is determined by the energy, angle, and position that the particle has when entering the Sweeper Magnet. The Sweeper Magnet bends and separates particles of different magnetic rigidities. For isotopes with the same

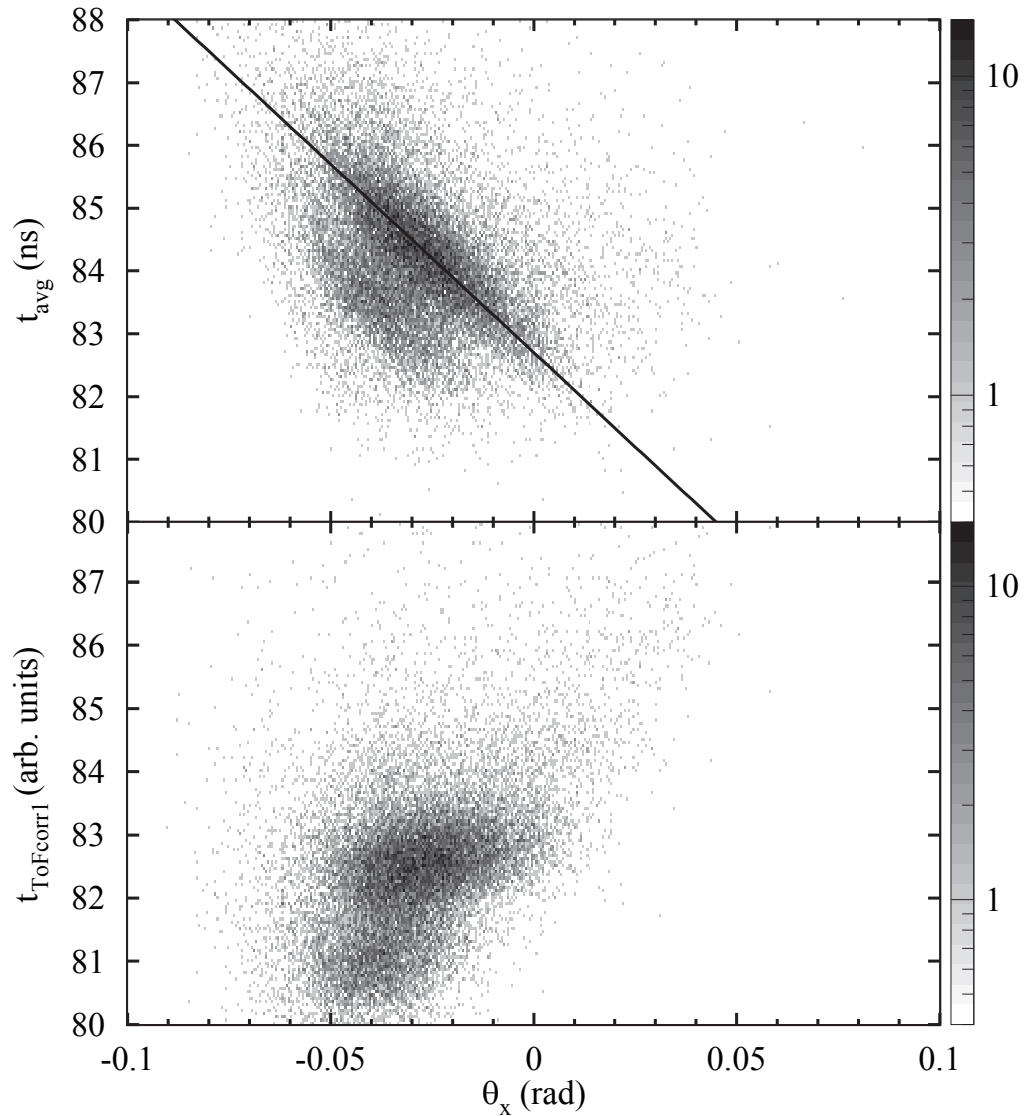


Figure 4.20: Average ToF versus θ_x without (top) and with (bottom) θ_x correction. The line in the upper spectrum indicates the corrected trend.

magnetic rigidity or momentum, the heavier ones will be slower giving a longer average ToF. Therefore isotope separation can be achieved by using a parameter that is proportional to the magnetic rigidity of the particle. The dispersive position and angle measured in the CRDCs provide two such parameters. The dispersive angle θ_x was chosen for the first correction to the average ToF as shown in Figure 4.20.

The θ_x correction was applied to the average ToF, t_{avg} , using:

$$t_{\text{ToFcorr1}} = t_{\text{avg}}(\text{ns}) + \theta_x(\text{rad}) 62(\text{ns/rad}) \quad (4.7)$$

where t_{ToFcorr1} is the θ_x corrected ToF. After the θ_x correction, the isotopic separation can be improved with the constructed dispersive position (x') in the CRDCs, measured positions x_{ta} and y_{ta} at the reaction target, and the measured non-dispersive angle θ_y using the CRDCs.

The spectra shown in Figure 4.21 shows the dependence of the t_{ToFcorr1} on dispersive position (x') calculated using:

$$x'(mm) = x_1(mm) - 433(mm) \tan(\theta_x) \quad (4.8)$$

The x' dispersive position was chosen at a plane upstream from CRDC1 near the edge of the Sweeper Magnet's magnetic field. The plane chosen provided the least dependence of x' on θ_x after the particle traveled through the magnetic field. The position x' is proportional to second order effects of different momenta as well as the expected parabolic function dependence on different path lengths from the reaction target to the dE scintillator. The x' dispersive position provides the correction to t_{ToFcorr1} using:

$$t_{\text{ToFcorr2}} = t_{\text{ToFcorr1}} - (5.0 \times 10^{-4} (ns/mm)^2 x'(mm)^2 + 6.5 \times 10^{-3} (ns/mm) x'(mm)) \quad (4.9)$$

where t_{ToFcorr2} is after the x' correction.

The ToF dependence on the x_{ta} and y_{ta} positions at the reaction target are expected to be linear. The x_{ta} and y_{ta} positions are tracked forward to the reaction target using the PPACs and matrix generated for the quadrupole triplet. The linear dependence of t_{ToFcorr2} on x_{ta} position, and t_{ToFcorr3} on y_{ta} position are shown in the spectra in Figures 4.22 and 4.23.

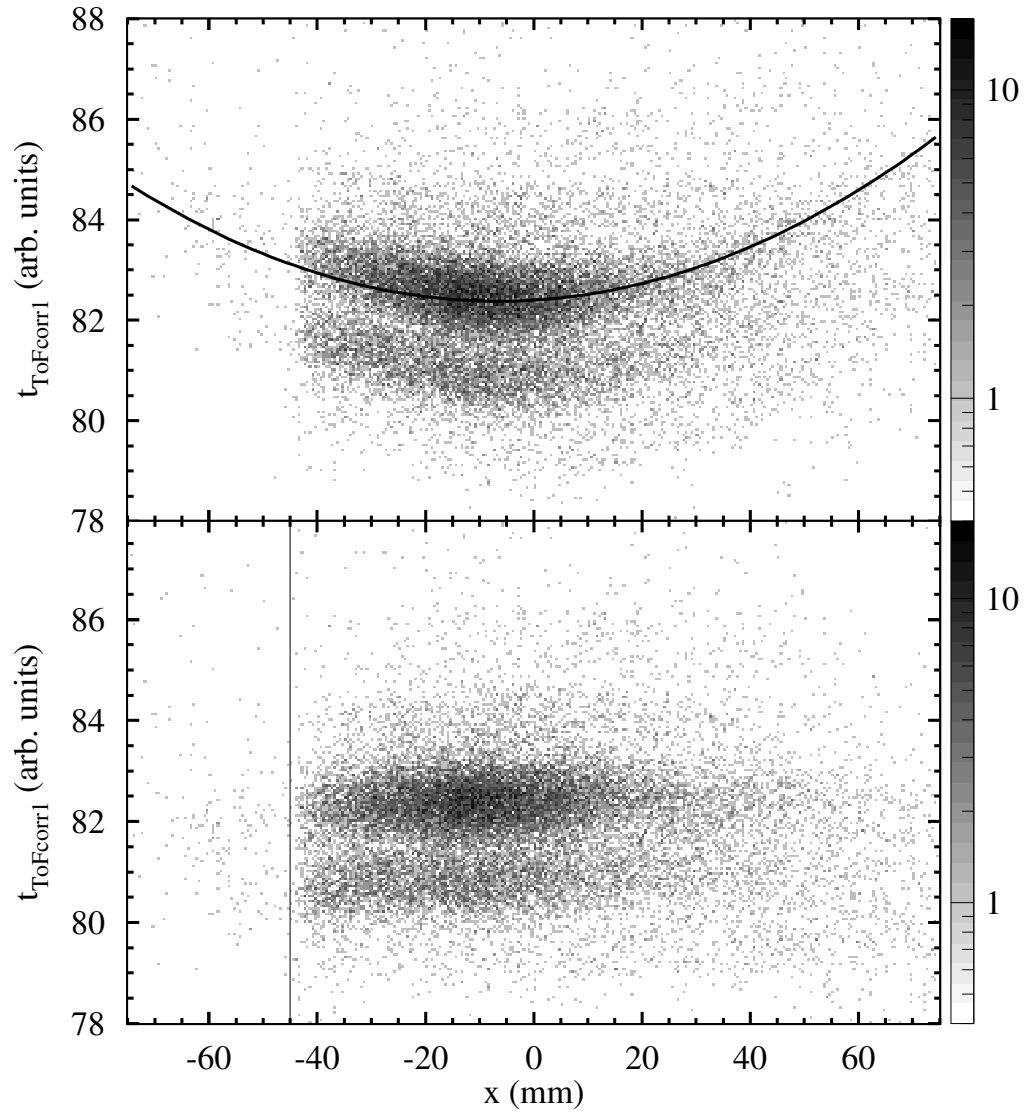


Figure 4.21: Corrected ToF t_{ToFcorr1} versus constructed dispersive position x' uncorrected (top) and corrected (bottom). All events to the left the line on the bottom plot were scattered beam events and rejected.

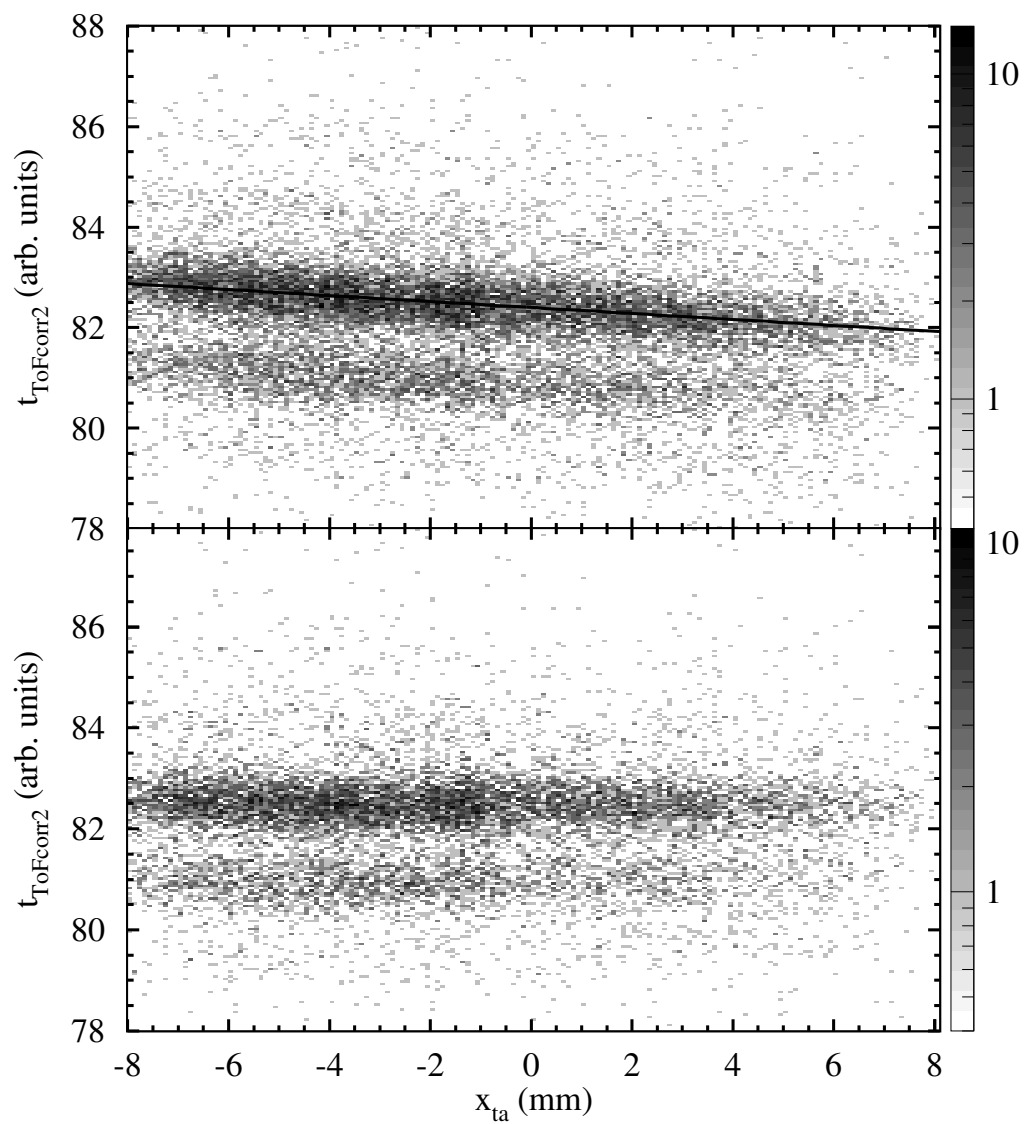


Figure 4.22: Corrected ToF $t_{ToFcorr2}$ versus x -position at the reaction target uncorrected (top) and corrected (bottom).

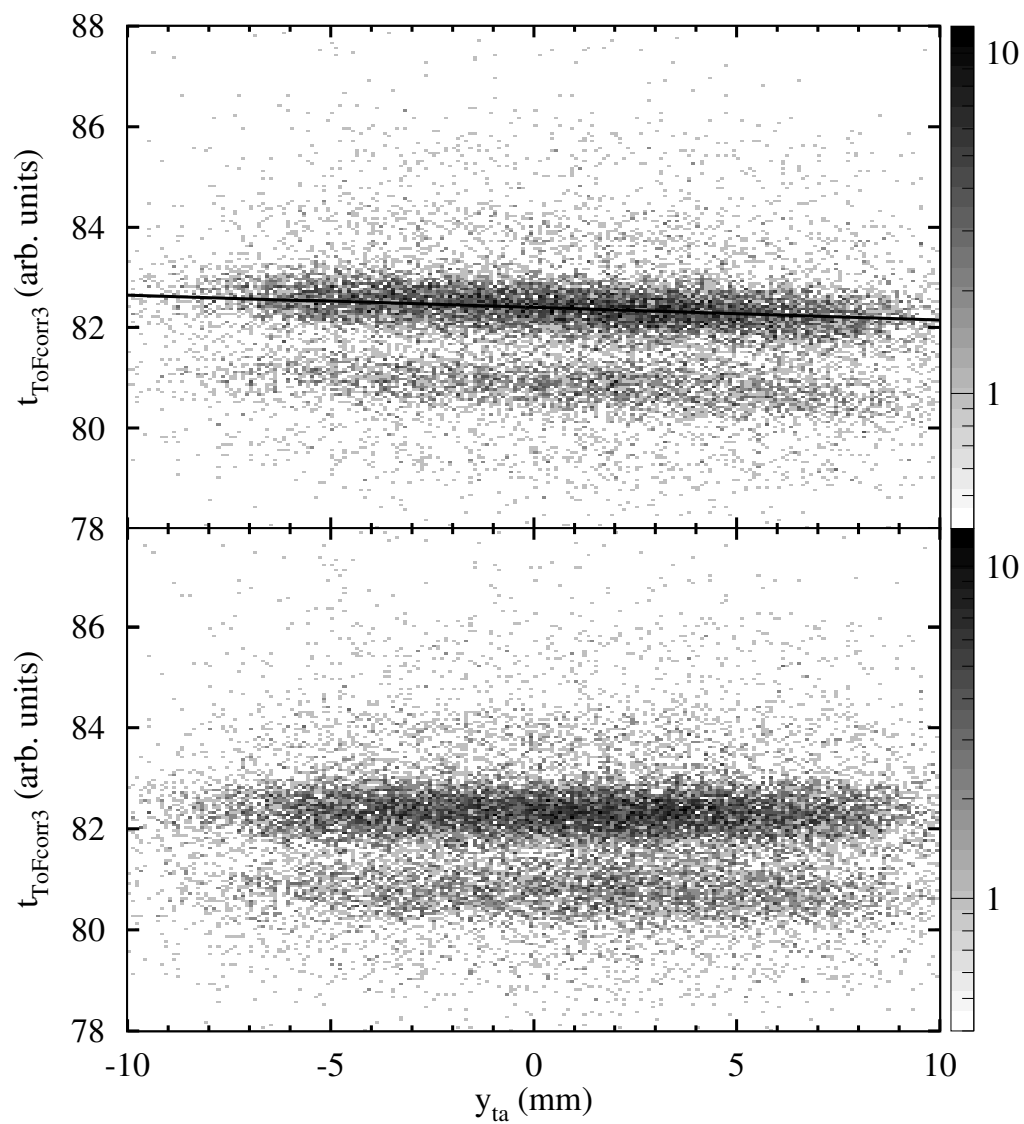


Figure 4.23: Corrected ToF $t_{ToFcorr3}$ versus y -position at the reaction target uncorrected (top) and corrected (bottom).

The linear correction of t_{ToFcorr2} with x_{ta} position was performed using:

$$t_{\text{ToFcorr3}} = t_{\text{ToFcorr2}} + 0.0595(ns/m)x_{\text{ta}}(m) \quad (4.10)$$

where t_{ToFcorr3} was then corrected by the linear dependence on y_{ta} position using:

$$t_{\text{ToFcorr4}} = t_{\text{ToFcorr3}} + 0.02495(ns/m)y_{\text{ta}}(m) \quad (4.11)$$

The last correction involved the non-dispersive angle (θ_y) constructed using measured non-dispersive positions in the CRDCs. The parabolic dependence is shown in the spectra shown in Figure 4.24 and the correction using:

$$t_{\text{final}} = t_{\text{ToFcorr4}} + 170(ns/rad)^2\theta_y(rad)^2 - 9.732(ns/rad)\theta_y(rad) \quad (4.12)$$

provided the final ToF, t_{final} .

The final corrected ToF t_{final} spectrum shown in Figure 4.25 shows the separation of oxygen isotopes. The FWHM for each isotope was approximately 0.8 ns and the separation between the isotopes were approximately 1.5 ns. The spectrum shown in Figure 4.26 shows the linear relationship of the TKE to the corrected ToF in the spectrum. Since the $B\rho$ acceptance of the Sweeper Magnet and nucleus charge q are constant, the nucleus mass m and velocity v will be inversely proportional to one another as shown in:

$$B\rho = \frac{mv}{q} \quad (4.13)$$

Therefore, shorter ToF t_{final} correspond to faster particles which then have to be higher in mass. This relationship along with the expected dispersive positions and angles for different oxygen isotopes compared to measured dispersive positions and angles in coincidence with each group provides our isotope identification.

The isotope cuts for $^{21,22}\text{O}$ were two-dimensional as taken from the spectrum shown

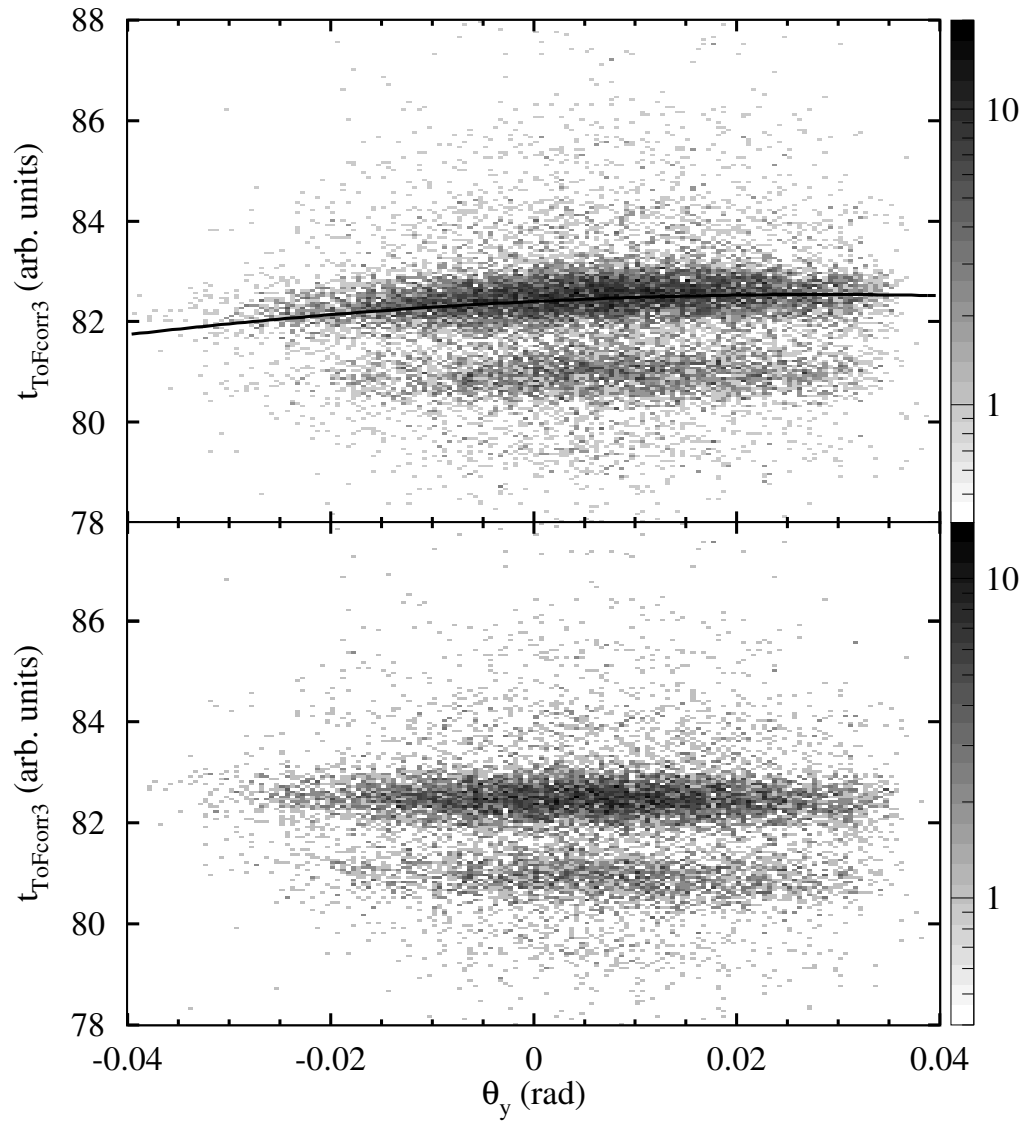


Figure 4.24: Corrected ToF t_{ToFcorr4} versus θ_y uncorrected (top) and corrected (bottom).

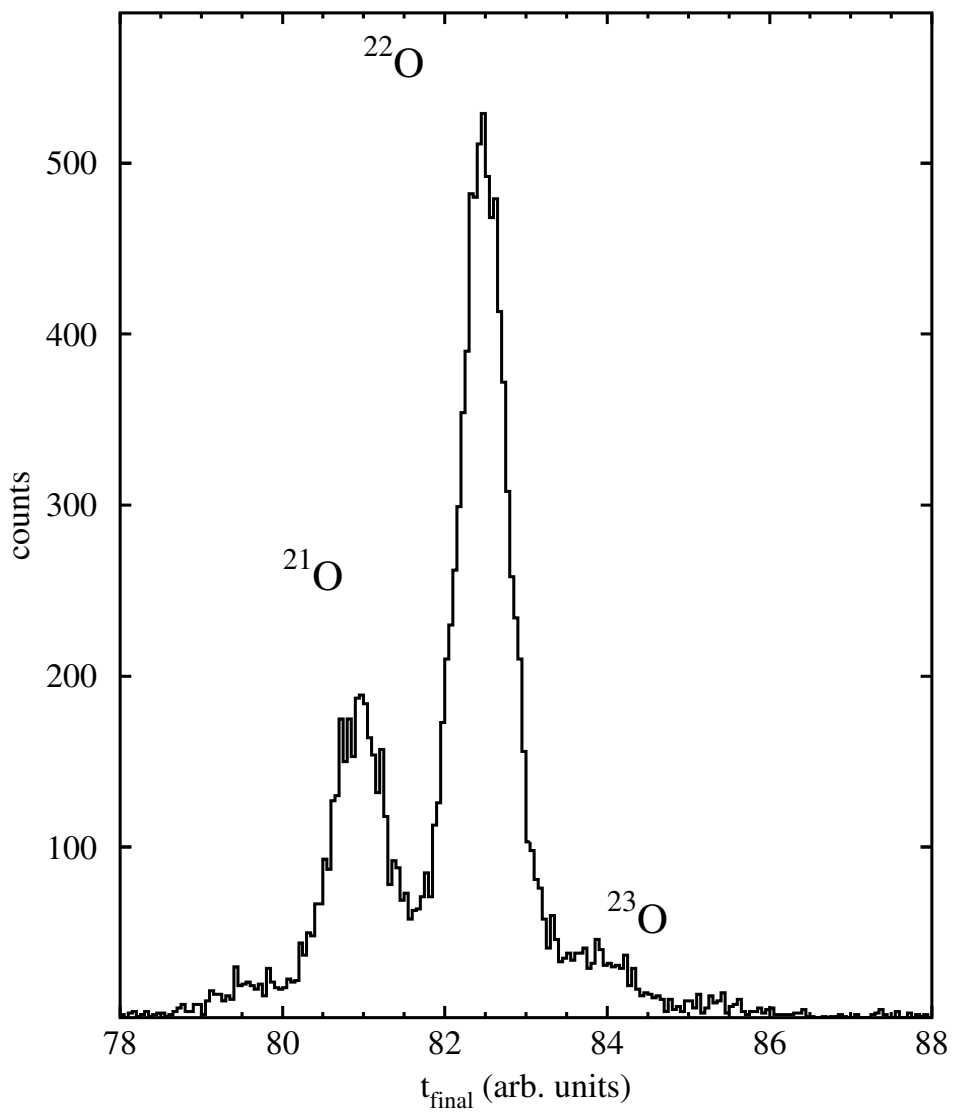


Figure 4.25: Final corrected ToF t_{final}

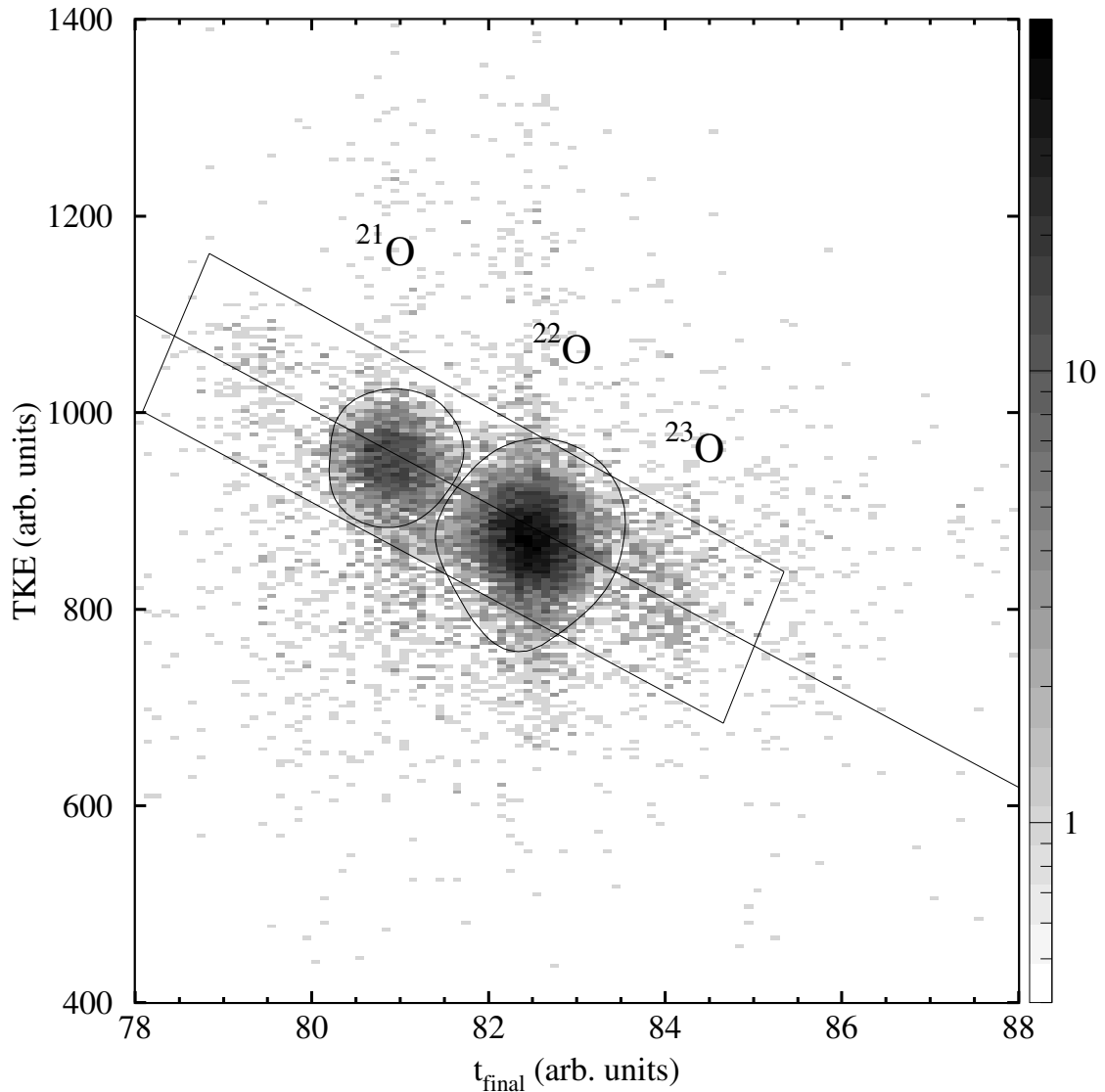


Figure 4.26: TKE energy versus ToF t_{final}

in Figure 4.26. The ^{23}O two-dimensional cut would include contamination from the ^{22}O fragment distribution. Since the final decay energy spectrum would have contamination from the ^{22}O fragment, the ^{23}O cut was taken from a projection onto a diagonal line passing through each isotope in the spectrum shown in Figure 4.26. The tilted box shows the events allowed in the projected spectrum. The cut for ^{23}O fragments is marked on the spectrum shown in Figure 4.27. Based on three Gaussian fits to the spectrum, the contamination of ^{22}O fragment in the ^{23}O cut is approximately

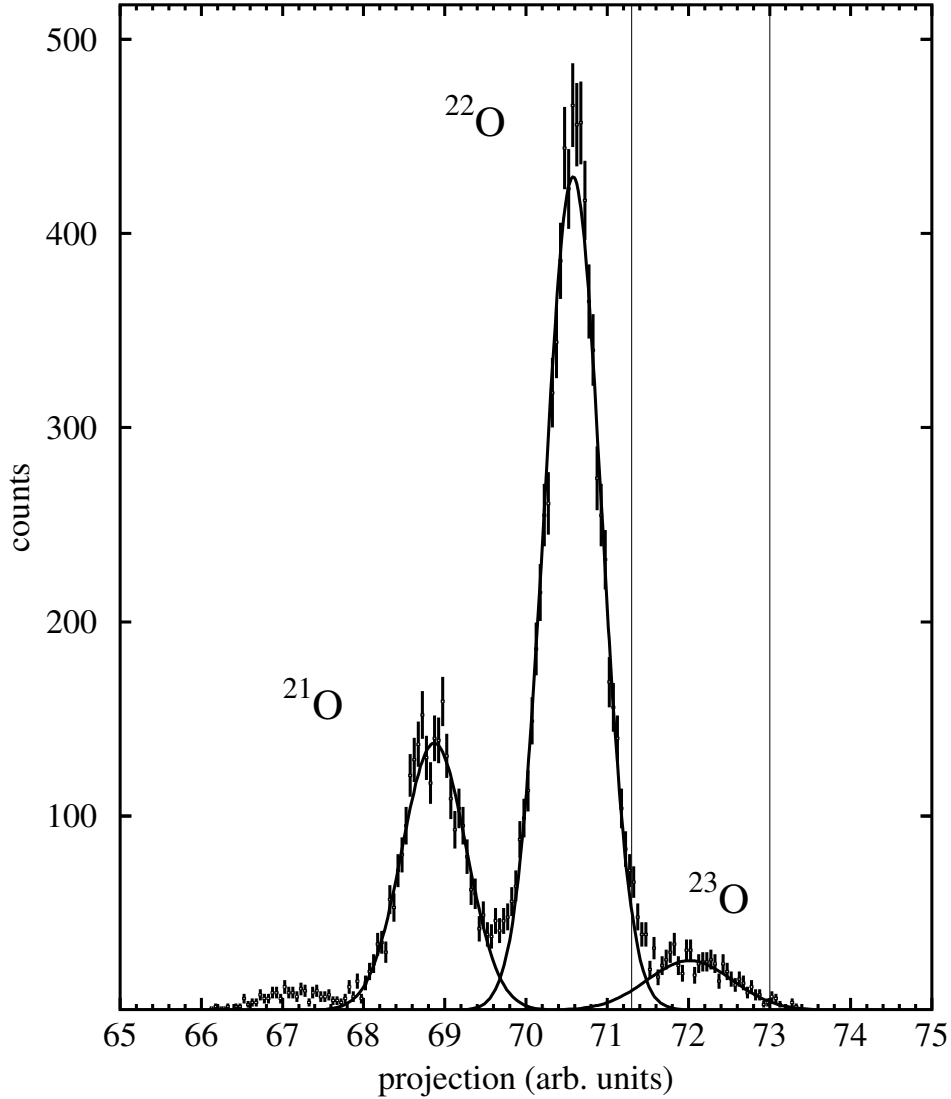


Figure 4.27: Projection from TKE versus corrected ToF plot where the solid lines represent Gaussian fits of the $^{21,22,23}\text{O}$ isotopes. The reduced χ^2 of the nine parameter fit is 1.257.

20% of the total counts in the cut. The contamination will be subtracted out of the final decay spectrum.

4.7 Neutron Processing

The momentum vector of the neutron was calculated based on the ToF and position information from MoNA. The calibrations of the TDCs, x -position, and time offsets

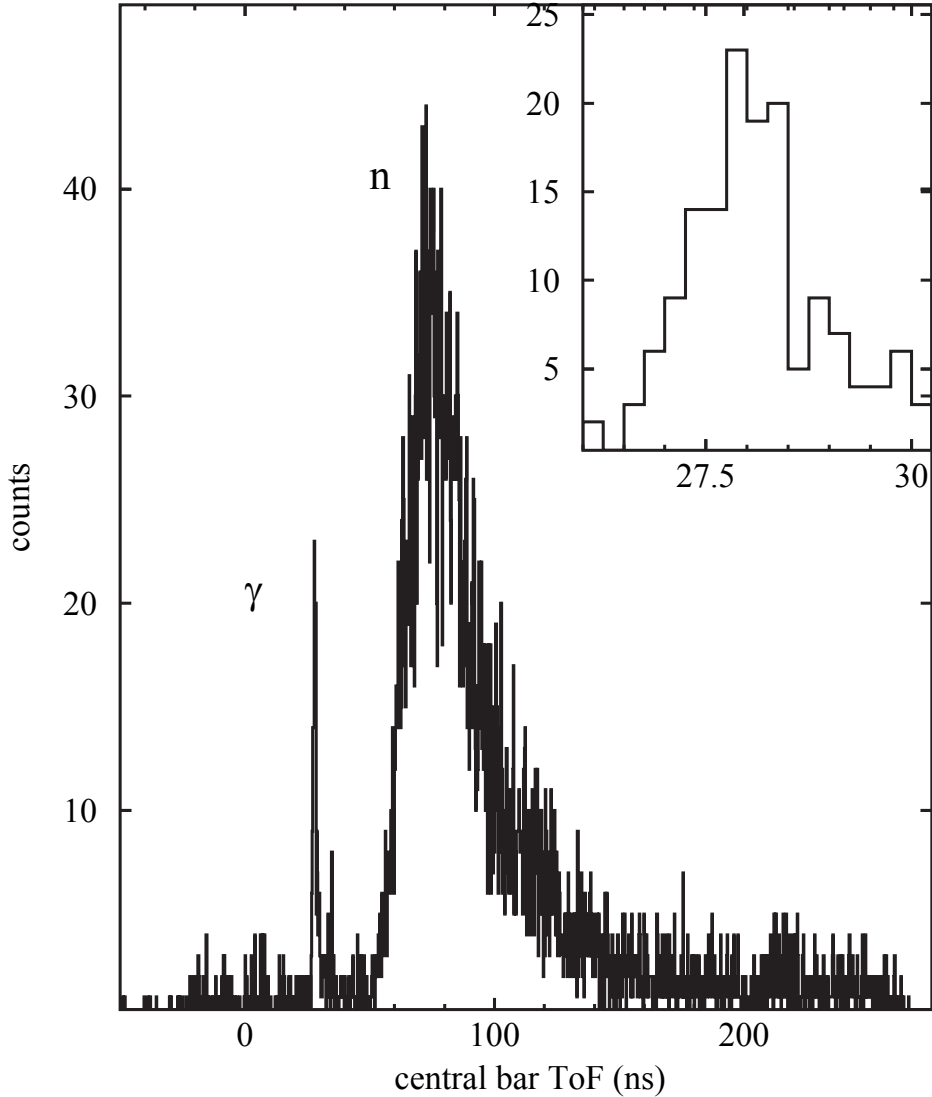


Figure 4.28: Prompt γ -ray and neutron peaks in the neutron ToF spectrum. The high yield of prompt γ -rays was produced using a thick reaction target. The upper-right insert is zoomed in on the prompt γ -ray peak.

for each bar were performed before the experiment started using cosmic muons and time calibrator (see Ref. [37] and Section 4.1).

After the time calibrations, the overall time offset of MoNA was determined using the prompt γ -ray peak in the neutron ToF spectrum, see Figure 4.28. The prompt γ -ray peak was produced when the incoming beam struck a thick reaction target which stopped the secondary beam. The time offset was set so that the ToF of the

γ -ray peak was at 27.75 ns which corresponds to the flight time of the γ -rays from the reaction target to MoNA. The x -position of the neutrons was calculated from the calibrated time difference between the left t_L and right t_R PMTs of each detector module:

$$x = (t_L - t_R)m_x(cm/ns) + b_x(cm) \quad (4.14)$$

where m_x and b_x are the calibration coefficients for each detector module. The cosmic muons were employed to determine the calibration coefficients m_x and b_x by locating the edge of each detector module on the time difference spectrum between the left and right PMTs. The time-of-flight for the neutron t_n was the calibrated time average of the left and right PMTs of each detector module:

$$t_n = \frac{t_L + t_R}{2} \quad (4.15)$$

The y - and z -positions were determined by the y and z centers of the detector module the neutron interacted with. The velocity of the neutron v_n was calculated with the measured neutron ToF t_n , and position of the neutron specified by the x -, y -, and z -positions as shown:

$$v_n = \frac{\sqrt{x^2 + y^2 + z^2}}{t_n} \quad (4.16)$$

The velocity v_n was used to calculate the energy of the neutron and to sort events with more than one recorded hit in MoNA. The first hit chosen for the reconstruction was the fastest hit after 45 ns to eliminate choosing a γ -ray or a velocity that was not physical. The spectrum shown in Figure 4.29 shows the physical acceptance of MoNA. The horizontal width of MoNA is completely filled and the vertical position shows a noticeable cut at ± 50 cm. The vertical acceptance is from the opening of the downstream end of the Sweeper Magnet. Neutron events were accepted within the ± 50 cm vertical acceptance.

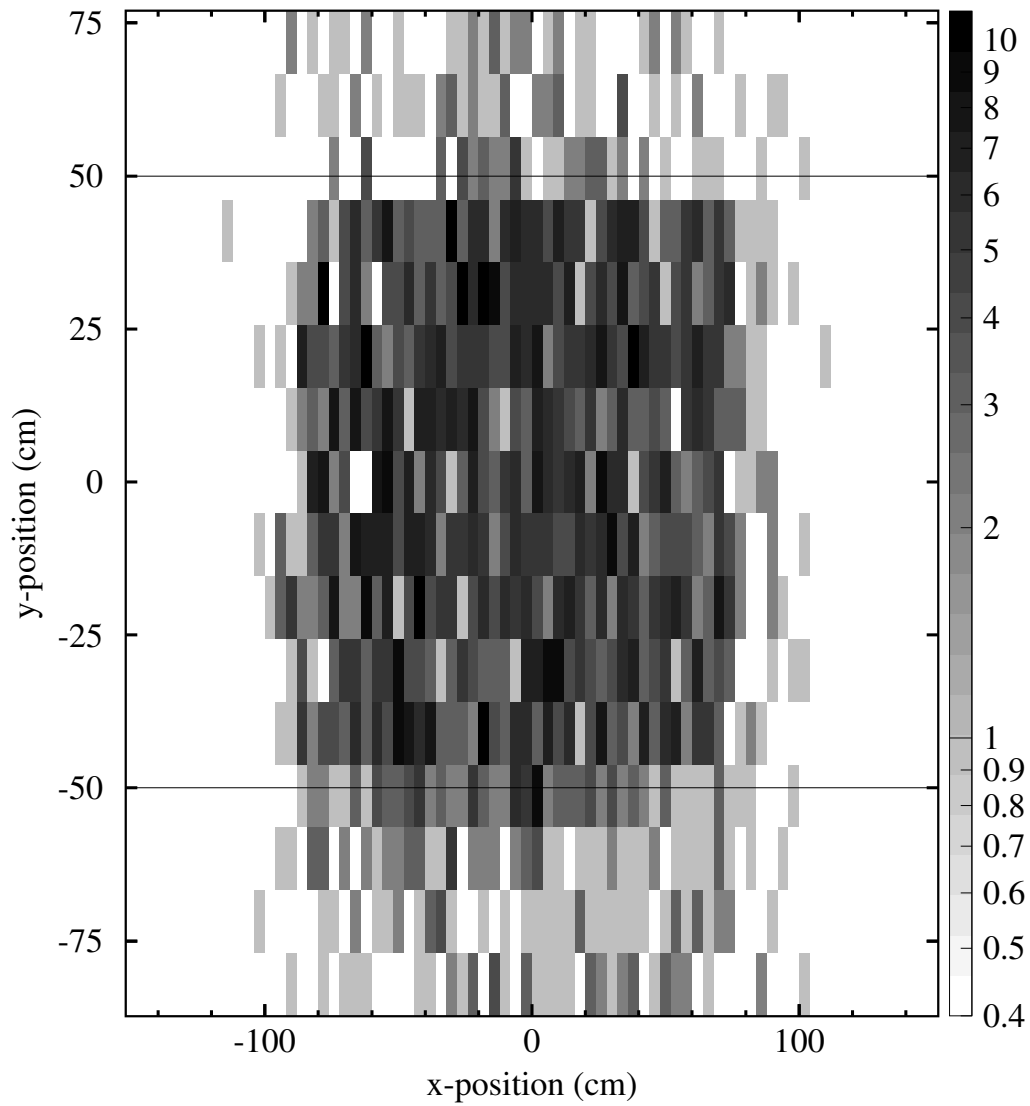


Figure 4.29: y -position versus x -position on MoNA. The lines are drawn to indicate the vertical acceptance due to the opening at the end of the Sweeper Magnet.

4.8 Fragment Reconstruction

The Sweeper Magnet's magnetic field was mapped to produce an ion-optical matrix using COSY Infinity [41]. The magnetic field was mapped using seven Hall probes mounted vertically to a movable cart to measure the field across the gap. The cart moved on top of a plate along arcs of fixed radius through the magnet. A stepper motor was used to move the cart along the arc and the cart required manual assistance to move from one arc to the next one. There were 45 arcs with a spacing of 2.54 mm and 568 measurements along an arc with an interval of approximately 2 mm yielding a total of around 25,000 data points per probe. The mapping was performed with 12 evenly spaced field settings all recorded at the same time. A reference Hall probe mounted between the top and bottom coils was used for recording the magnet's field setting. The Hall probe was used instead of the current readout of the power supply, because the probe would indicate any hysteresis in the magnet for low currents. Before mapping, the coordinate systems of both the reaction target and charged particle detectors were measured on the mapping plate. The error in the magnetic field measurement due to the Hall probes and electronics was half of the least significant bit in the electronics or approximately 3 Gauss. Since the Hall probes measurement uncertainty was so small, a temperature probe was placed next to the Sweeper Magnet to monitor temperature change. The error for multiple measurements along the same arc was a maximum of approximately 30 Gauss, where the uncertainty is dominated by the position placement uncertainty of the stepper motor.

The maps were processed by performing individual fits for each measured Hall probe at each position against the reference Hall probe. The functions calculated by the fit were the starting point for any magnetic field map calculation. For a given field setting of the Sweeper Magnet, magnetic field values were calculated for each position along the arc, radius, and Hall probe vertical position. The central field plane magnetic field values were then calculated from fits vertically across several Hall probes.

The central field plane or midplane is the where there are only perpendicular field components to the horizontal direction. The Sweeper Magnet map shown in Figure 4.30 is an example of a calculated midplane field. A field map of this character was used by COSY to calculate matrices. To make a matrix with COSY, a specific trajectory or reference trajectory needs to be specified. The reference trajectory connects the coordinate system at the reaction target to the charged particle detectors. The reference trajectory is defined by a magnetic rigidity, length of the reference trajectory and the starting position and angle into the magnetic field map. Before calculating matrices, a consistent coordinate system was determined for the reaction target, charged particle detectors, and the reference trajectory for the matrix calculation. The Runge-Kutta method within COSY to track particles through the magnetic field was employed to compare calculated trajectories with measured trajectories. Based on the comparisons, a consistent coordinate definition was determined.

Based on the coordinate system definition, the magnetic field measurements of the Sweeper Magnet were used to produce two types of ion-optical matrices, forward and inverse. Forward ion-optical matrices propagated properties of the charged particles from the reaction target to the plane of CRDC1 with matrix terms up to third order. Inverse ion-optical matrices propagated properties of the charged fragments from the plane of CRDC1 to the reaction target, where the inverse matrix is defined as the inverse of the forward matrix. The parameters needed at the reaction target to propagate through the forward ion optical matrix were positions (x_{ta}, y_{ta}) , angles $(\theta_{x-ta}, \theta_{y-ta})$ and relative energy difference (δ_{ta}) which gave positions (x_{crdc}, y_{crdc}) and

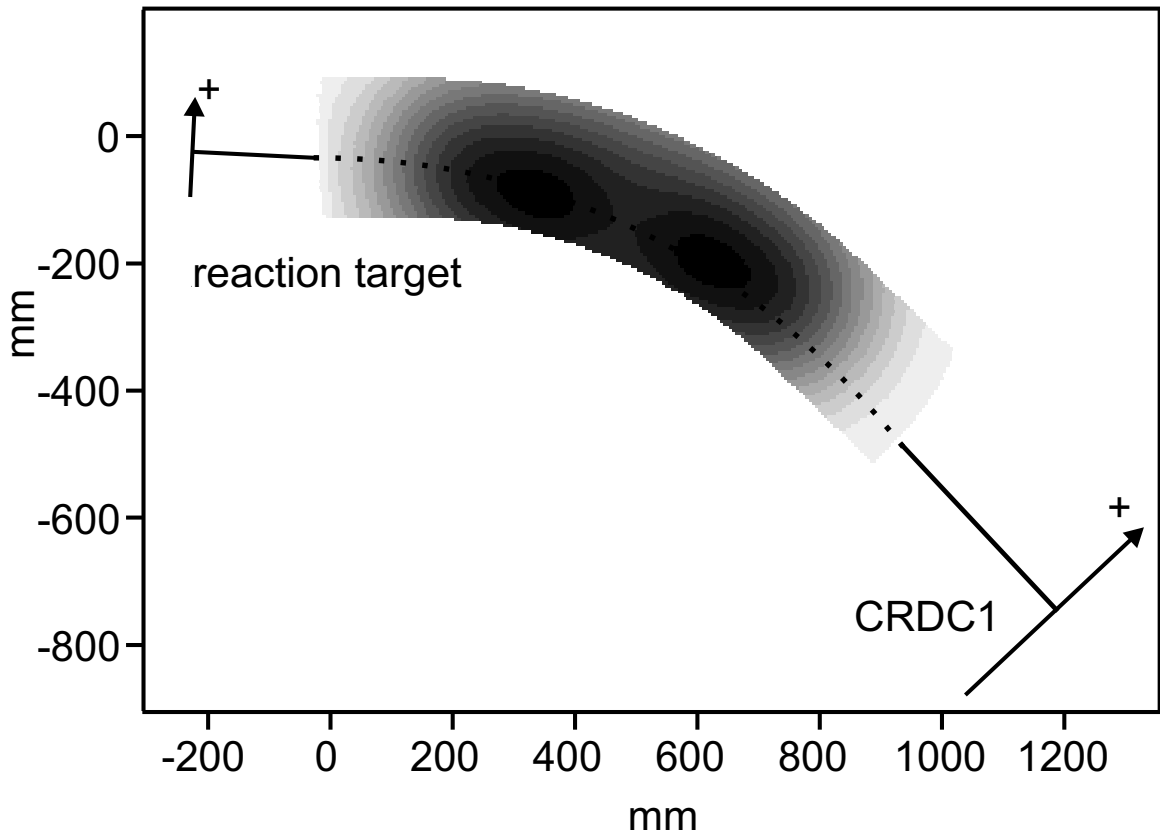


Figure 4.30: A Sweeper Magnet map with positive dispersive position marked at both the reaction target and CRDC1. The beamline and charged particle detector axis are indicated by lines perpendicular to the arrows. The dashed line represents a possible trajectory through the field. The two peaks are approximately 4 Tesla.

angles $(\theta_{x\text{-crdc}}, \theta_{y\text{-crdc}})$ at CRDC1 using:

$$\begin{pmatrix} x_{\text{crdc}} \\ \theta_{x\text{-crdc}} \\ y_{\text{crdc}} \\ \theta_{y\text{-crdc}} \\ \Delta l \end{pmatrix}_{out} = M_{\text{for}} \begin{pmatrix} x_{\text{ta}} \\ \theta_{x\text{-ta}} \\ y_{\text{ta}} \\ \theta_{y\text{-ta}} \\ \delta_{\text{ta}} \end{pmatrix}_{in} \quad (4.17)$$

where M_{for} is the forward transformation matrix. The Δl parameter not mentioned previously is used to calculate path length difference to the reference trajectory length, but cannot be measured and is therefore not relevant to this work. The positions $(x_{\text{ta}}, y_{\text{ta}})$ and angles $(\theta_{x\text{-ta}}, \theta_{y\text{-ta}})$ at the reaction target were calculated by using a forward ion-optical matrix for the quadrupole triplet propagating parameters from the PPACs to the reaction target. The energy difference, δ_{ta} , was calculated with the secondary beam energy using:

$$\delta_{\text{ta}} = \frac{E_{\text{beam}} - E_{\text{rt}}}{E_{\text{rt}}} \quad (4.18)$$

where E_{beam} is the calculated energy of the incoming beam event-by-event and E_{rt} is the energy of the reference trajectory for ^{26}Ne for a given magnetic field setting of the Sweeper Magnet.

The inverse ion optical matrices calculated from the positions and angles at CRDC1 and x_{ta} position to angles, energy difference, and the y -position parameters at the reaction target using:

$$\begin{pmatrix} \theta_{x\text{-ta}} \\ y_{\text{ta}} \\ \theta_{y\text{-ta}} \\ \delta_{\text{ta}} \\ \Delta l \end{pmatrix}_{out} = M_{\text{inv}} \begin{pmatrix} x_{\text{crdc}} \\ \theta_{x\text{-crdc}} \\ y_{\text{crdc}} \\ \theta_{y\text{-crdc}} \\ x_{\text{ta}} \end{pmatrix}_{in} \quad (4.19)$$

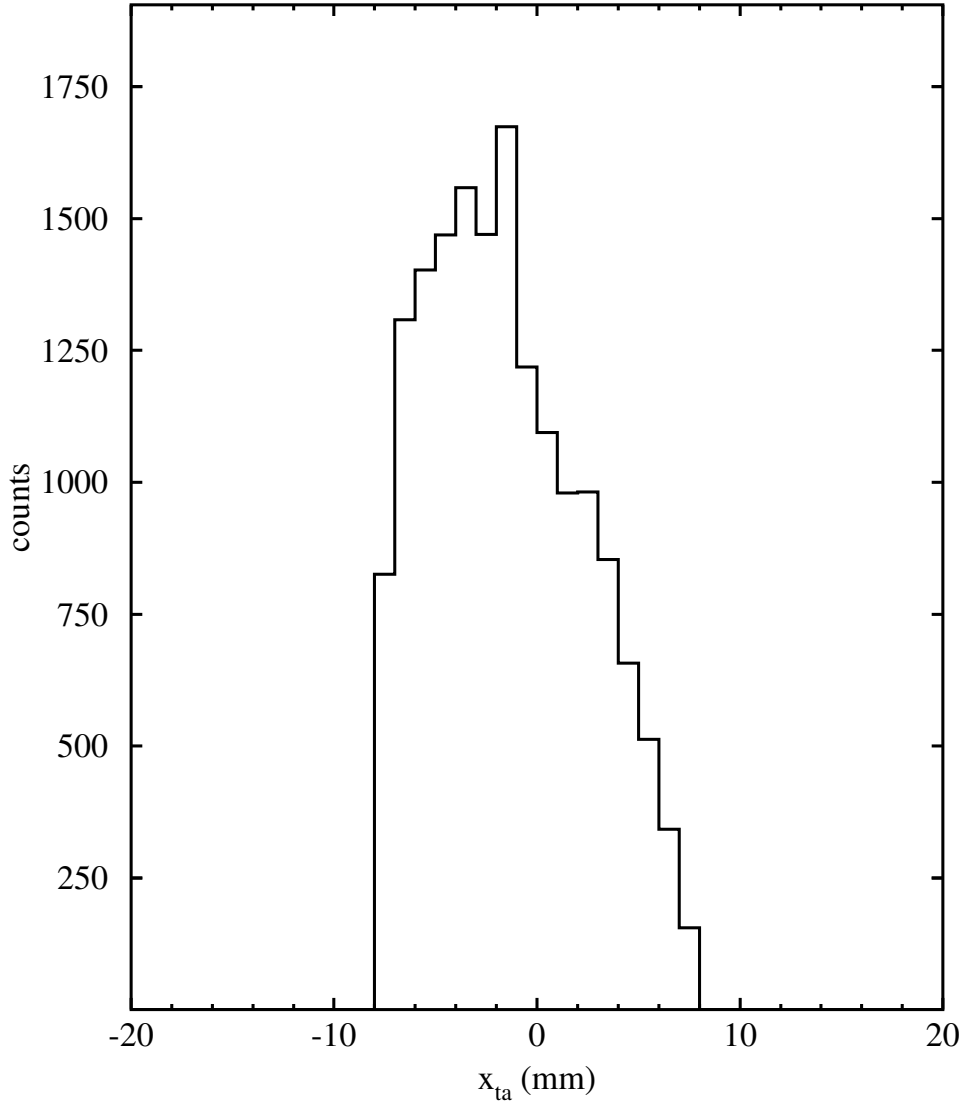


Figure 4.31: Dispersive position distribution x_{ta} at the reaction target.

This is different than the process in COSY for making backward (inverse) ion-optical matrices as shown in Reference [43]. COSY assumes that all particles enter the magnetic field at the same dispersive target position x_{ta} . However, this assumption is incorrect for this case as shown in the spectrum shown in Figure 4.31.

Since the dispersive position x_{ta} distribution had a FWHM width of approximately 12 mm wide, the x_{ta} position was included in the inverse matrix using a different process than in COSY. Starting with the forward matrix input and output

vectors specified in Equation 4.17, the partial inversion process exchanged specific pairs of parameters between the input and output vectors. The non-dispersive parameters were exchanged, y_{ta} and $\theta_{y\text{-ta}}$ with y_{crdc} and $\theta_{y\text{-crdc}}$. The dispersive direction parameters were exchanged by swapping $\theta_{x\text{-ta}}$ with x_{crdc} and then δ_{ta} with $\theta_{x\text{-crdc}}$. The x_{ta} parameter is left in the input vector available for inclusion in the inverse matrix transformation. With the inverse and forward matrices calculated, the accuracy of the matrices was tested for three different magnetic field settings. The comparison of parameters measured and calculated with the matrices characterized the uncertainty of the matrices beyond the charged particle detector resolutions. Comparisons for relevant parameters at the reaction target and CRDC1 were made by propagating the secondary ^{26}Ne beam through the forward and inverse matrices.

First a set of comparisons was performed to check the forward matrix output at the coordinate system of CRDC1 (Figures 4.32-4.35) and a second set to check the inverse matrix output at the reaction target (Figures 4.36-4.39). The reaction target and CRDC1 dispersive direction parameters (x_{ta} , $\theta_{x\text{-ta}}$, δ_{ta} , x_{crdc} , and $\theta_{x\text{-crdc}}$) and non-dispersive direction parameters (y_{ta} , $\theta_{y\text{-ta}}$, y_{crdc} and $\theta_{y\text{-crdc}}$) do not mix for the first-order matrix elements which are the most important, so any inconsistency in a reconstructed parameter at CRDC1 will be seen as an inconsistency in a reconstructed parameter at the reaction target in the same direction. The comparisons for propagated parameters to measured parameters both at the reaction target and at CRDC1 for the data-taking rigidity setting show good agreement for all parameters. The high-rigidity setting shows good agreement in all parameters except for x_{crdc} and $\theta_{x\text{-ta}}$. This represents a problem in reconstructing to and from very negative dispersive positions on CRDC1. The non-dispersive plane reconstruction forward and backward compare well for both the data and high rigidity settings.

It can be concluded from the comparisons that the matrix calculation works well for the phase space covered by the ^{26}Ne secondary beam. The error for reconstructing from negative dispersive positions at CRDC1 has been determined and is included

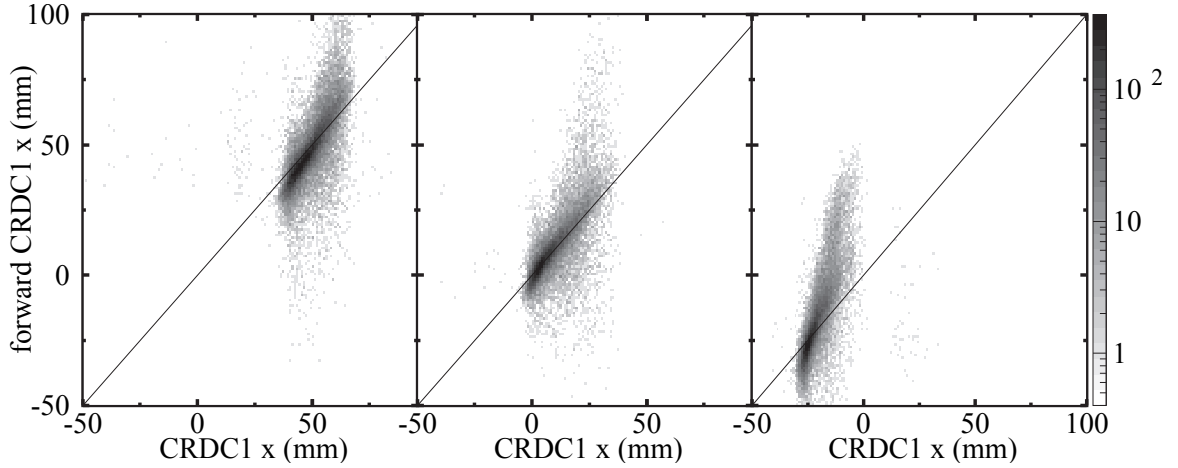


Figure 4.32: Forward-tracked CRDC1 x -position versus measured CRDC1 x -position. Low $B\rho$ setting (left), data-taking $B\rho$ setting (center), and high $B\rho$ setting (right).

in the experimental resolution. The comparison of data for the low rigidity setting does exhibit problems in reconstructing several parameters with both reconstruction in the dispersive and non-dispersive directions. The most likely issue is that the matrix elements do not reproduce the trajectory of charged particles that take a path through the edges of the peaks shown in Figure 4.30. A trajectory off of the peaks passes through a region where the field lines bend particles in the non-dispersive direction, which results in changes to higher than first order matrix elements that are not represented well. Since the reconstructed data rigidity setting does not cover the large positive dispersive position on CRDC1, the inaccuracies of the matrices presented for the low rigidity setting are not issues for this particular reconstruction.

4.9 Neutron Decay Spectra

Figure 4.40 shows the spectra of the charged fragment and the neutron kinetic energies for the unbound decays of $^{22}\text{O}^*$, $^{23}\text{O}^*$, and $^{24}\text{O}^*$. The three fragment energy spectra appear very similar. From a simple reaction mechanism picture one would expect that all fragments are produced at almost the same velocity, thus leading to a higher kinetic energy for the heavier oxygen isotopes. However, the detected fragments are

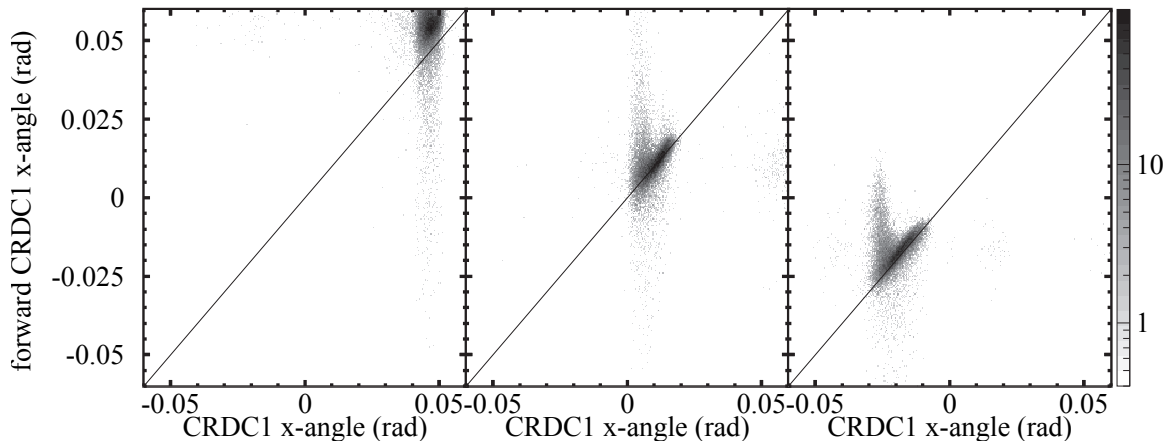


Figure 4.33: Forward-tracked CRDC1 x -angle versus measured CRDC1 x -angle. Low $B\rho$ setting (left), data-taking $B\rho$ setting (center), and high $B\rho$ setting (right).

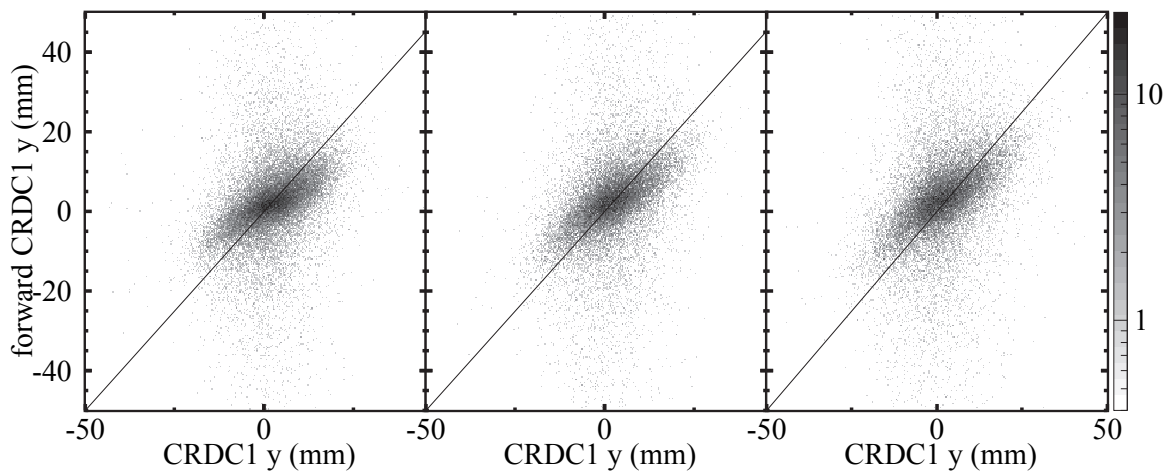


Figure 4.34: Forward-tracked CRDC1 y -position versus measured CRDC1 y -position. Low $B\rho$ setting (left), data-taking $B\rho$ setting (center), and high $B\rho$ setting (right).

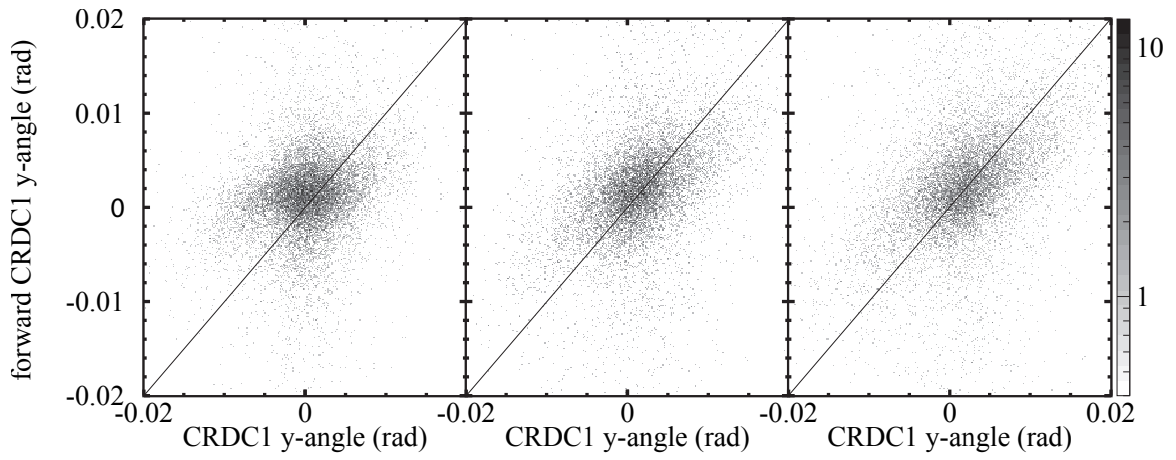


Figure 4.35: Forward-tracked CRDC1 y -angle versus measured CRDC1 y -angle. Low $B\rho$ setting (left), data-taking $B\rho$ setting (center), and high $B\rho$ setting (right).

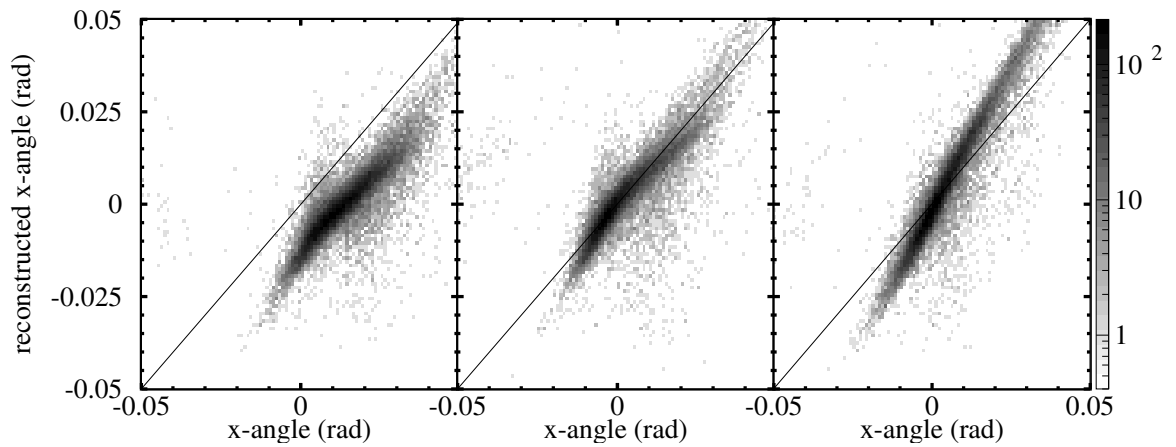


Figure 4.36: Backward reconstructed target x -angle versus measured target x -angle. Low $B\rho$ setting (left), data-taking $B\rho$ setting (center), and high $B\rho$ setting (right).

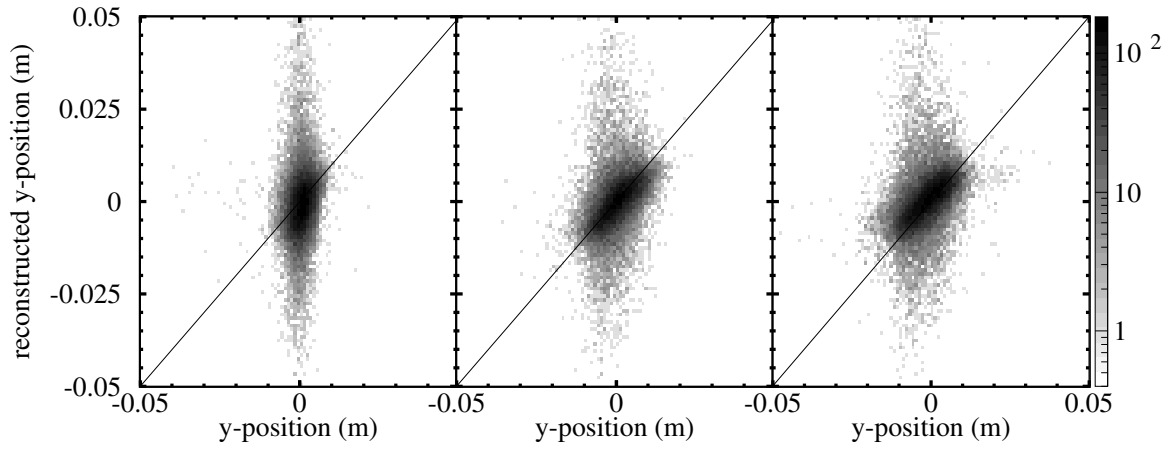


Figure 4.37: Backward reconstructed target y -position versus measured target y -position. Low $B\rho$ setting (left), data-taking $B\rho$ setting (center), and high $B\rho$ setting (right).

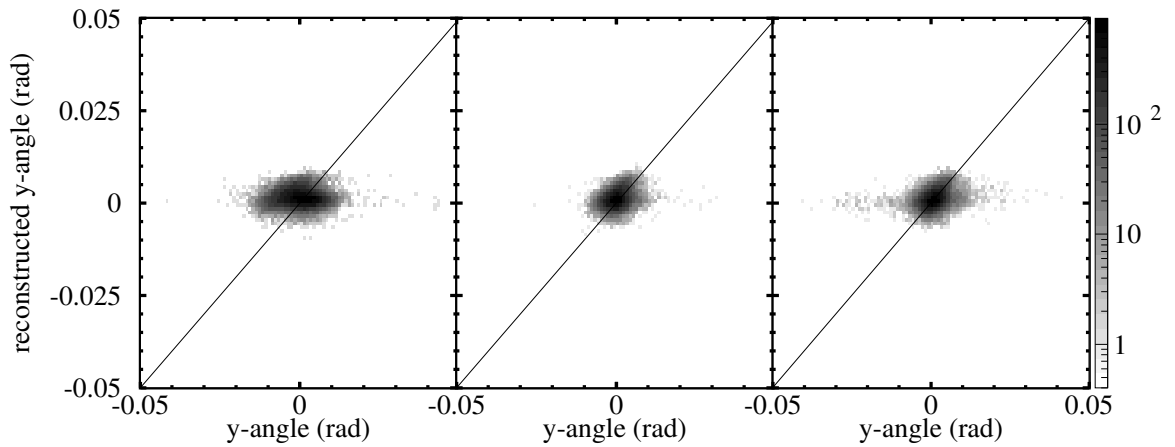


Figure 4.38: Backward reconstructed target y -angle versus measured target y -angle. Low $B\rho$ setting (left), data-taking $B\rho$ setting (center), and high $B\rho$ setting (right).

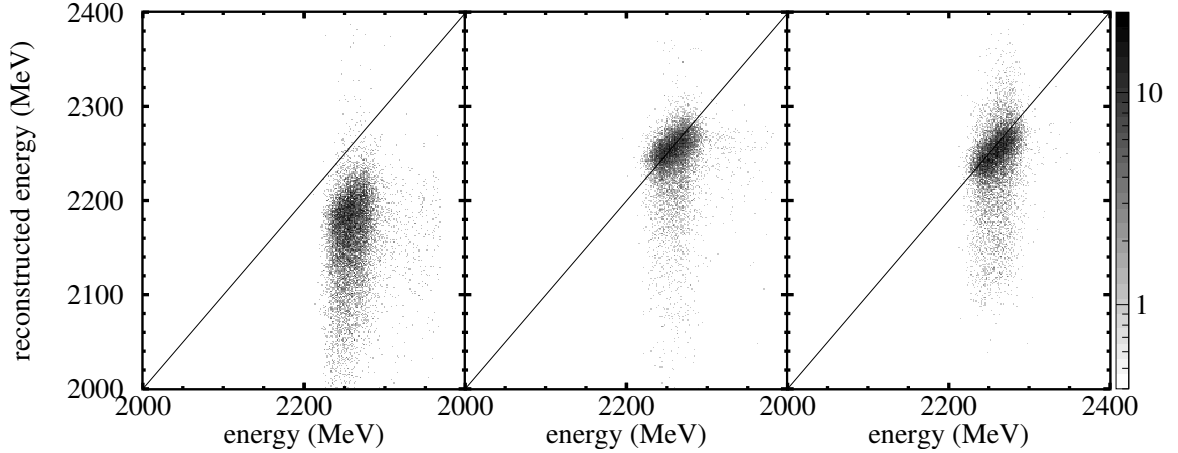


Figure 4.39: Backward reconstructed secondary beam energy versus measured secondary beam energy. Low $B\rho$ setting (left), data-taking $B\rho$ setting (center), and high $B\rho$ setting (right).

limited to the same momentum acceptance of the Sweeper Magnet which corresponds to lower energies for the heavier isotopes. The fragment kinetic energy spectrum for the decay of $^{24}\text{O}^*$ is broader because of the contamination of fragments from the decay of $^{23}\text{O}^*$ which are incorrectly reconstructed as $^{24}\text{O}^*$.

The neutron kinetic energies are much more sensitive to the decay of the unbound excited oxygen isotopes than the resulting fragment energies. Momentum conservation in the center-of-mass system transforms into much larger velocity (and therefore energy) differences in the lab-system. While the decay spectra of $^{24}\text{O}^*$ and $^{23}\text{O}^*$ show fairly narrow peaks, the decay of $^{22}\text{O}^*$ is substantially broader indicating a significantly different decay pattern.

Further evidence for differences for the decay of the three oxygen isotopes can be seen in the angular distributions of the fragments and neutrons as shown in Figure 4.41. Again, the fragment angular distributions only show minor differences, the decays of $^{24}\text{O}^*$ and $^{23}\text{O}^*$ seem to peak at slightly smaller angles compared to the $^{22}\text{O}^*$ decay. In contrast, the neutron angular distribution of the $^{23}\text{O}^*$ decay peaks at significantly smaller angles than $^{22}\text{O}^*$ or $^{24}\text{O}^*$ which is a first indication of a small decay energy. $^{24}\text{O}^*$ seems only slightly more forward-peaked relative to the almost sym-

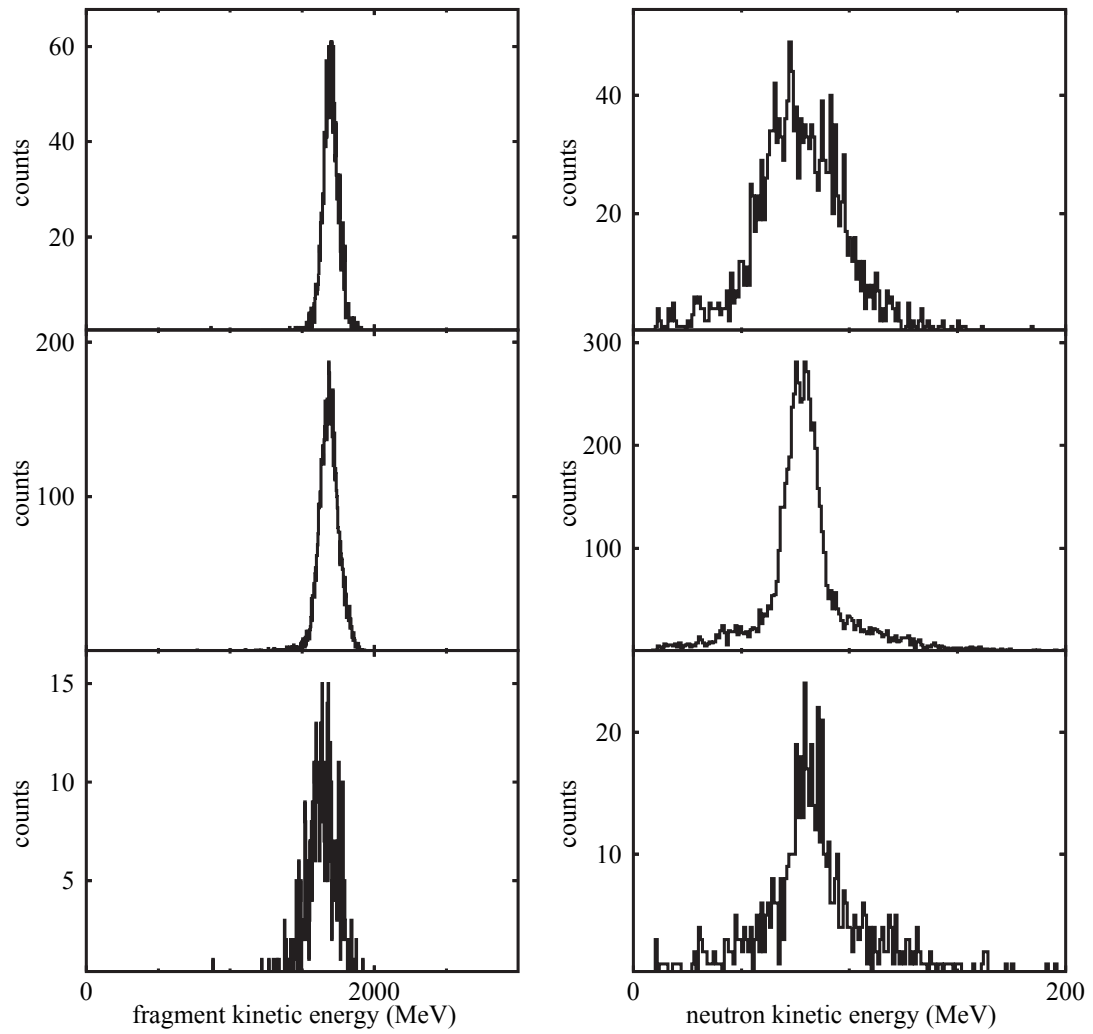


Figure 4.40: Reconstructed fragment kinetic energy spectrum (left) and neutron kinetic energy spectrum (right) for $^{22}\text{O}^*$ (top), $^{23}\text{O}^*$ (middle), and $^{24}\text{O}^*$ (bottom).

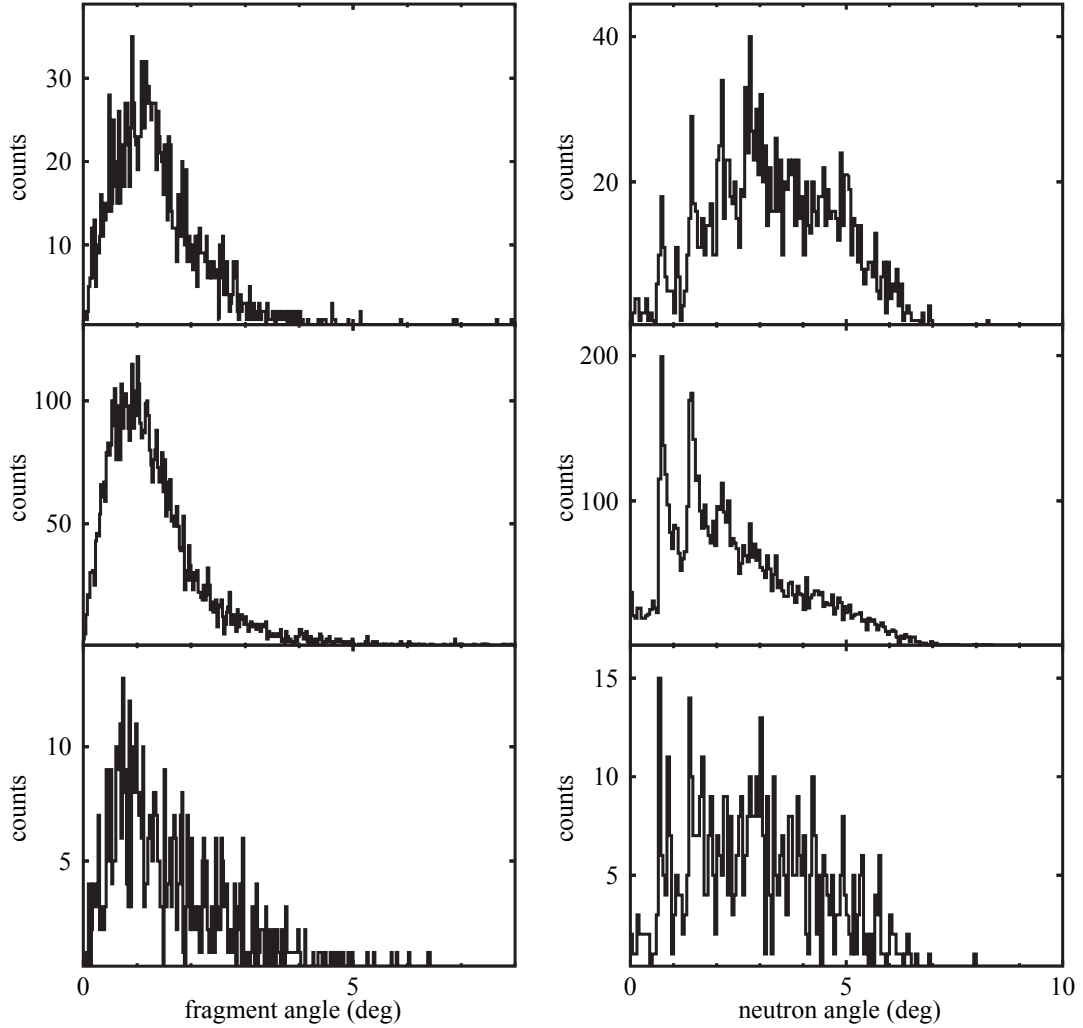


Figure 4.41: Reconstructed fragment angle spectrum (left) and neutron angle spectrum (right) for unbound $^{22}\text{O}^*$ (top), $^{23}\text{O}^*$ (middle), and $^{24}\text{O}^*$ (bottom).

metrically (around 3.5 degrees) $^{22}\text{O}^*$ angular distribution. The spikes in the neutron angular distribution spectra are due to the discrete position of the detector modules in MoNA along the y -direction.

Finally, from the neutron and fragment kinetic energies and angles, the opening angle θ_{open} and decay energy spectra were calculated according to Equation 3.4. The measured fragment energies had to be corrected for the energy loss in the target. Because the location of the interaction within the target was unknown it was as-

sumed that the reaction took place in the center of the target and an energy loss corresponding to half the target thickness was added to the fragment energies.

Figure 4.42 shows the spectra for the opening angle between the charged fragment and neutron θ_{open} and the decay energy spectra of $^{22}\text{O}^*$, $^{23}\text{O}^*$, and $^{24}\text{O}^*$. The opening-angle spectra reinforce the evidence seen in the neutron angular distribution. The decay from $^{23}\text{O}^*$ is very sharply peaked below one degree, and the $^{24}\text{O}^*$ decay shows a narrower distribution peaked at smaller angles compared to the $^{22}\text{O}^*$ decay.

The decay energy spectra show a sharp peak for the decay of $^{23}\text{O}^*$ at an energy very close to the threshold. Although not as distinct the decay energy spectrum of $^{24}\text{O}^*$ is significantly different from the $^{22}\text{O}^*$ decay energy spectrum. It peaks at smaller decay energies and is not as broad as the $^{22}\text{O}^*$ spectrum.

Before comparing the data with simulations it was instructive to create “mixed-event” spectra. These spectra were created by calculating the decay energy from the relevant fragment parameters from one event with the neutron parameters from the previous, thus unrelated event. The analysis will reveal if the observed coincidence events are truly correlated or not. Figure 4.43 shows a comparison of the decay energy spectra of $^{23}\text{O}^*$ and $^{24}\text{O}^*$ with the corresponding spectra created by event mixing.

There is no difference between the real data and the event-mixed data for the decay of $^{22}\text{O}^*$ indicating that the detected neutrons and fragments were not directly correlated. This can be understood by the many different possibilities to populate $^{22}\text{O}^*$ from ^{26}Ne and will be described in detail in the next section. In contrast, the “real and mixed $^{23}\text{O}^*$ decay energy spectra are significantly different. This is further strong evidence that the neutrons and fragments are strongly correlated and result from a discrete state in $^{23}\text{O}^*$. The limited statistics for the $^{24}\text{O}^*$ decay did not allow for a similar analysis.

As mentioned before, the $^{24}\text{O}^*$ data could not be cleanly separated from the very strong $^{23}\text{O}^*$ data and thus the decay energy spectra for $^{24}\text{O}^*$ contain contributions from $^{23}\text{O}^*$. From the spectrum shown in Figure 4.27 (see Section 4.6.2) it was es-

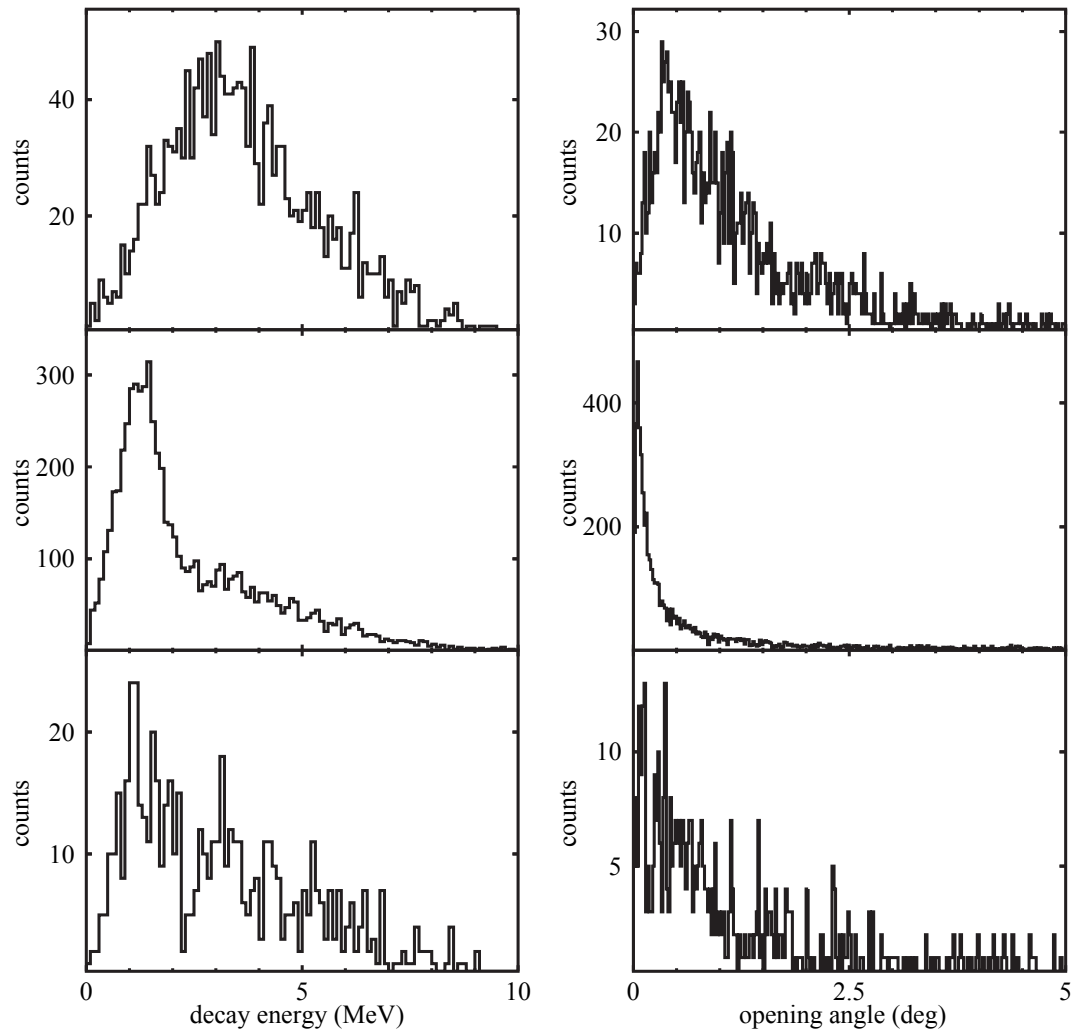


Figure 4.42: Opening angle (θ_{open}) between neutron and charged fragment (left) and reconstructed decay energy spectrum (20 keV/bin) (right) for $^{22}\text{O}^*$ (top), $^{23}\text{O}^*$ (middle), and $^{24}\text{O}^*$ (bottom).

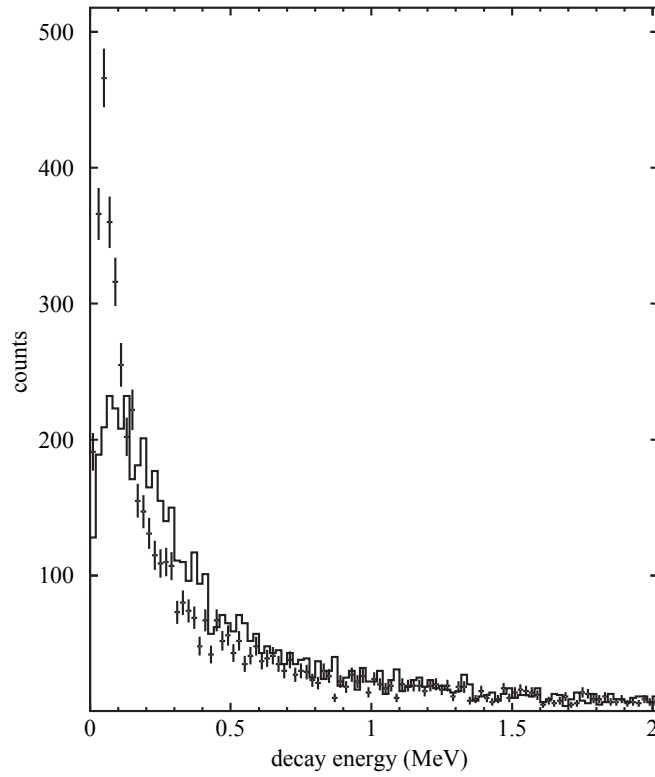
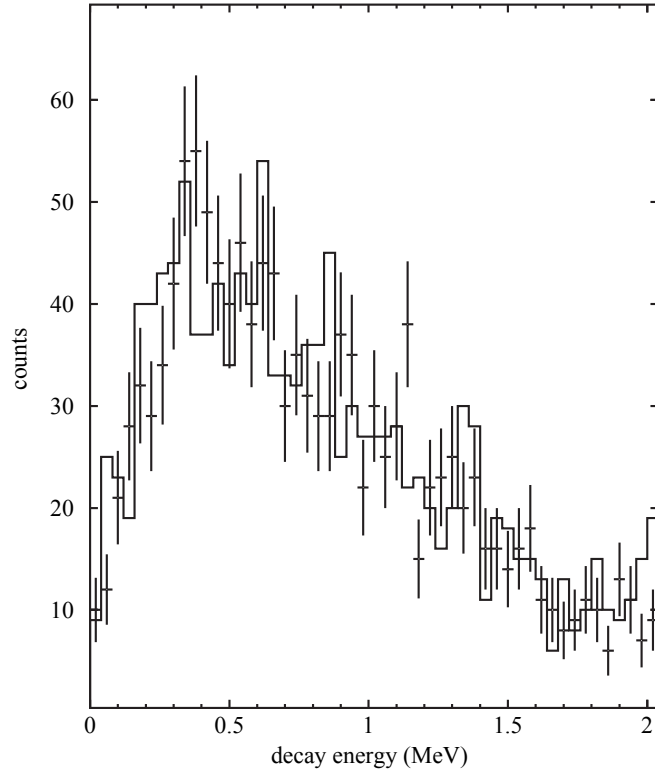


Figure 4.43: Decay energy spectra for correlated (points with error bars) and uncorrelated (histogram) neutron and charged fragment events for $^{22}\text{O}^*$ (top) and $^{23}\text{O}^*$ (bottom).

estimated that about 20% of the total events in the charged fragment gate of ^{23}O (corresponding to the decay of $^{24}\text{O}^*$) were ^{22}O (corresponding to the decay of $^{23}\text{O}^*$). This estimate was based on Gaussian fits of ^{23}O and ^{22}O in the spectrum shown in Figure 4.27.

The top panel shown in Figure 4.44 shows the decay energy spectrum of $^{24}\text{O}^*$ together with the $^{23}\text{O}^*$ spectrum scaled to 20% of the $^{24}\text{O}^*$ events. The $^{23}\text{O}^*$ spectrum appears broader than the decay energy spectra shown in Figure 4.42 because for the subtraction the events were reconstructed assuming the decay of $^{24}\text{O}^*$ and not $^{23}\text{O}^*$. The final (subtracted) $^{24}\text{O}^*$ decay energy spectrum is shown in the bottom panel shown in Figure 4.44. Even though the statistics is limited and the shape of the spectrum at low energies is uncertain due to the uncertainties of the contributions of $^{23}\text{O}^*$ a peak at about 600 keV is clearly evident.

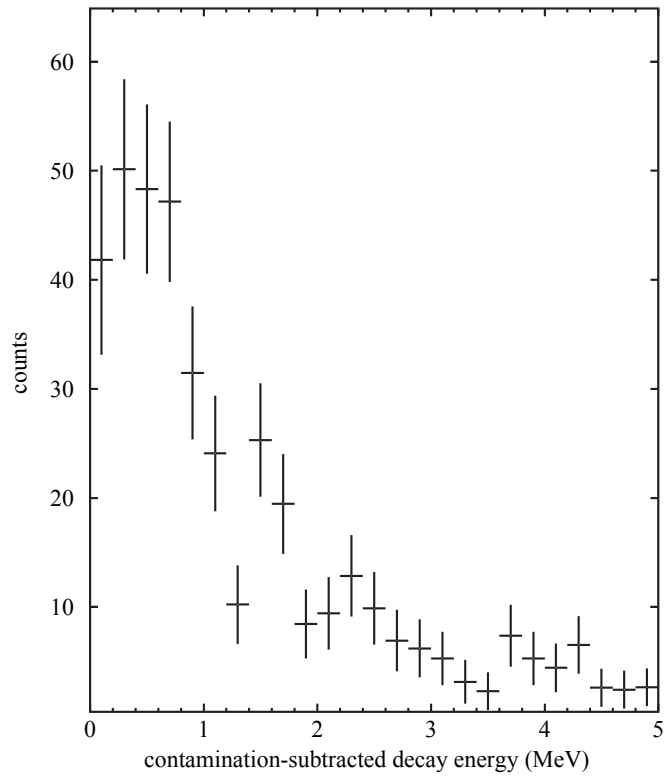
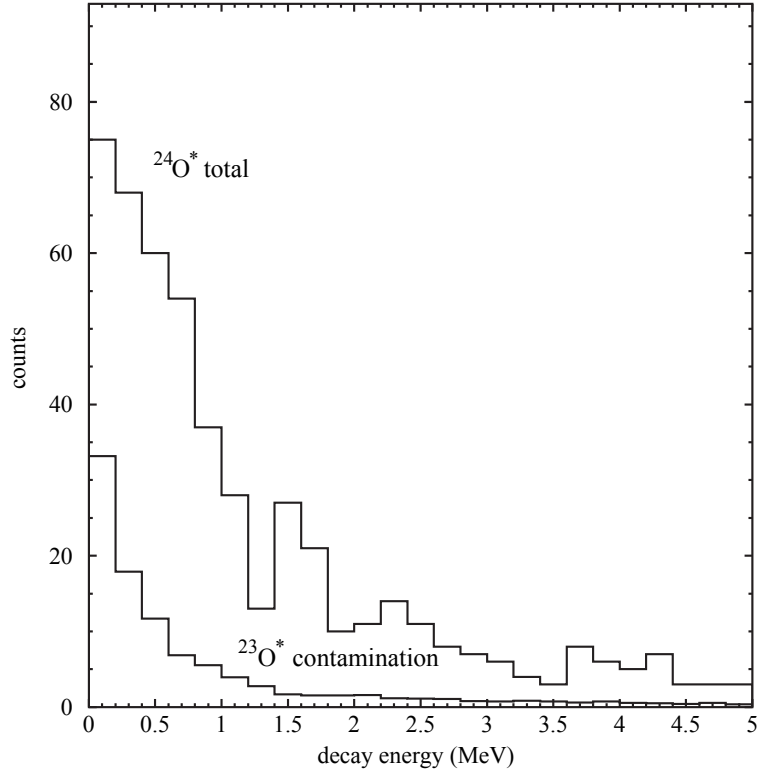


Figure 4.44: Top: $^{24}\text{O}^*$ spectrum with scaled $^{23}\text{O}^*$ spectrum used for the subtraction. Bottom: Subtracted decay energy spectrum of $^{24}\text{O}^*$.

Chapter 5

Discussion

5.1 Simulation

To extract the unbound decay energies and widths, the physical acceptances and efficiencies of the detector setup need to be taken into account in a simulation. A Monte Carlo code was written that simulated an 86 MeV/A ^{26}Ne secondary beam reacting on a 721.3 mg/cm² thick beryllium target. The beam position, angle and energy distributions, the position and time resolution of MoNA, and the position and angle resolution of the CRDCs were included as listed in Tables 5.1 and 5.2.

A gaussian distributed uncertainty was used for the charged particle parameters and the x -position and time-of-flight of the neutrons. The y - and z -positions of the

Table 5.1: Position and angle resolution in the x and y direction of the ^{26}Ne secondary beam at the target. ΔE is energy uncertainty.

Beam Parameter	σ
x_{ta}	5 mm
$\theta_{x\text{-ta}}$	10 mrad
y_{ta}	12 mm
$\theta_{y\text{-ta}}$	1.5 mrad
ΔE	2.6 MeV

Table 5.2: The charged particle and MoNA detector resolutions used in the simulation.

Charged Particle Parameter	σ	MoNA Parameter	σ
x_{crdc}	1.3 mm	x	5 cm
$\theta_{x\text{-crdc}}$	1 mrad	y	5 cm*
y_{crdc}	1.3 mm	z	5 cm*
$\theta_{y\text{-crdc}}$	1 mrad	t_i	0.1 ns
x_{ta}	0.7 mm		

*flat distribution of ± 5 cm

neutron were descritized and randomized with a flat probability distribution. The physical acceptance of MoNA was included in the tracking of the neutrons. Presently interactions of the neutrons in MoNA are not yet included in the simulations so that it is not possible to extract cross sections. The neutrons were assumed to stop in the first layer of MoNA.

A flat probability distribution for the point of interaction within the natural beryllium reaction target was assumed. The energy of the outgoing fragment was assumed to be the same energy per nucleon as the incoming ^{26}Ne . The directions of the emitted neutrons and charged particles were assumed to be isotropic and back-to-back in the center-of-mass frame. The decay energy distribution was modeled by a Breit-Wigner lineshape [44]:

$$\frac{d\sigma}{dE} = \frac{\Gamma}{(E - E_r)^2 + \frac{1}{4}\Gamma^2} \quad (5.1)$$

where the state is specified by the resonance energy (E_r) and width (Γ). In addition, neutron emission from the continuum at higher excitation energies was simulated by a thermalized neutron source of the shape [10, 45]:

$$F(E) = \sqrt{E}e^{-E/T} \quad (5.2)$$

where T is the nuclear temperature.

The simulation produced positions and angles of the secondary beam at the reaction target, positions and angles at CRDC1 for the charged fragment, and positions and time-of-flight for the neutrons at MoNA. The simulation produced event data in the same format as the actual data so that both could be analyzed with the same code.

5.2 Comparisons to Simulated Spectra

The spectra in Figures 5.1, 5.2 and 5.3 are comparisons of the simulated and measured decay energy spectra for $^{22}\text{O}^*$, $^{23}\text{O}^*$ and $^{24}\text{O}^*$, respectively.

As mentioned in Section 4.9, the neutron energies and angles as well as the opening angle between the neutrons and fragments of $^{22}\text{O}^*$ exhibited different shapes compared to $^{23}\text{O}^*$ and $^{24}\text{O}^*$ indicating a different decay pattern. The decay energy spectrum shows a broad distribution with no clear resonance structure. A simulation assuming a thermalized neutron source with a temperature of 2 MeV resulted in a good description of the data as shown in Figure 5.1.

The measured decay energy spectrum of $^{23}\text{O}^*$ is dominated by a strong narrow resonance close to the threshold. The data could be well described with a single resonance located at $E_r = 45$ keV with a width of $\Gamma = 20$ keV. In addition, a small contribution from a thermalized neutron source with a temperature of 1 MeV could account for the broad background (see Figure 5.2). A reduced χ^2 search yielded the best fit for $E_r = 48 \pm 10$ keV. The width of the simulated peak is dominated by the experimental resolution. Based on the fits, an upper limit for the width of the observed state is found to be approximately 30 keV.

The measured decay energy spectrum of $^{24}\text{O}^*$ shown in Figure 5.3 was fit by a simulated state with a resonance energy $E_r = 600$ keV and width $\Gamma = 300$ keV. From a reduced χ^2 search the resonance energy was determined to be $E_r = 670 \pm 150$ keV.

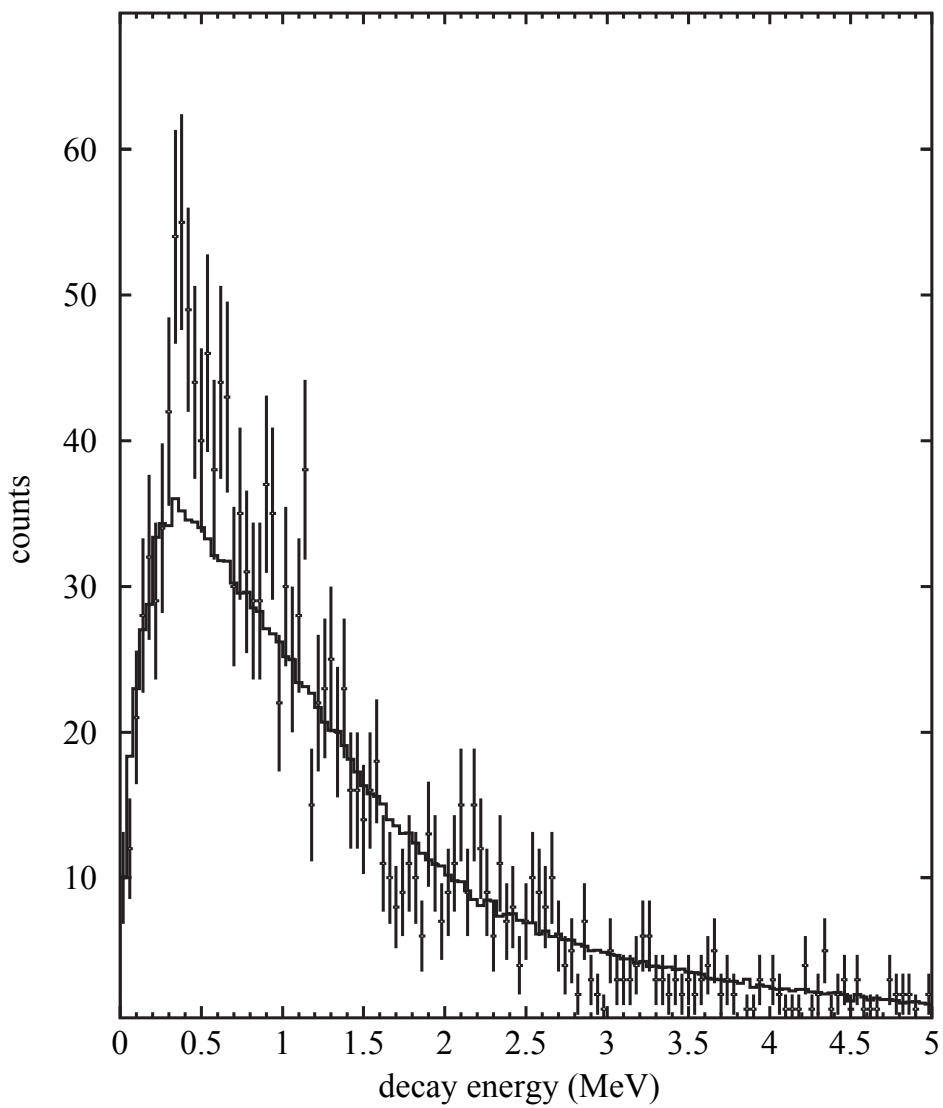


Figure 5.1: Decay energy spectrum of $^{22}\text{O}^*$. The histogram corresponds to fit assuming a thermalized neutron source of nuclear temperature $T = 2$ MeV.

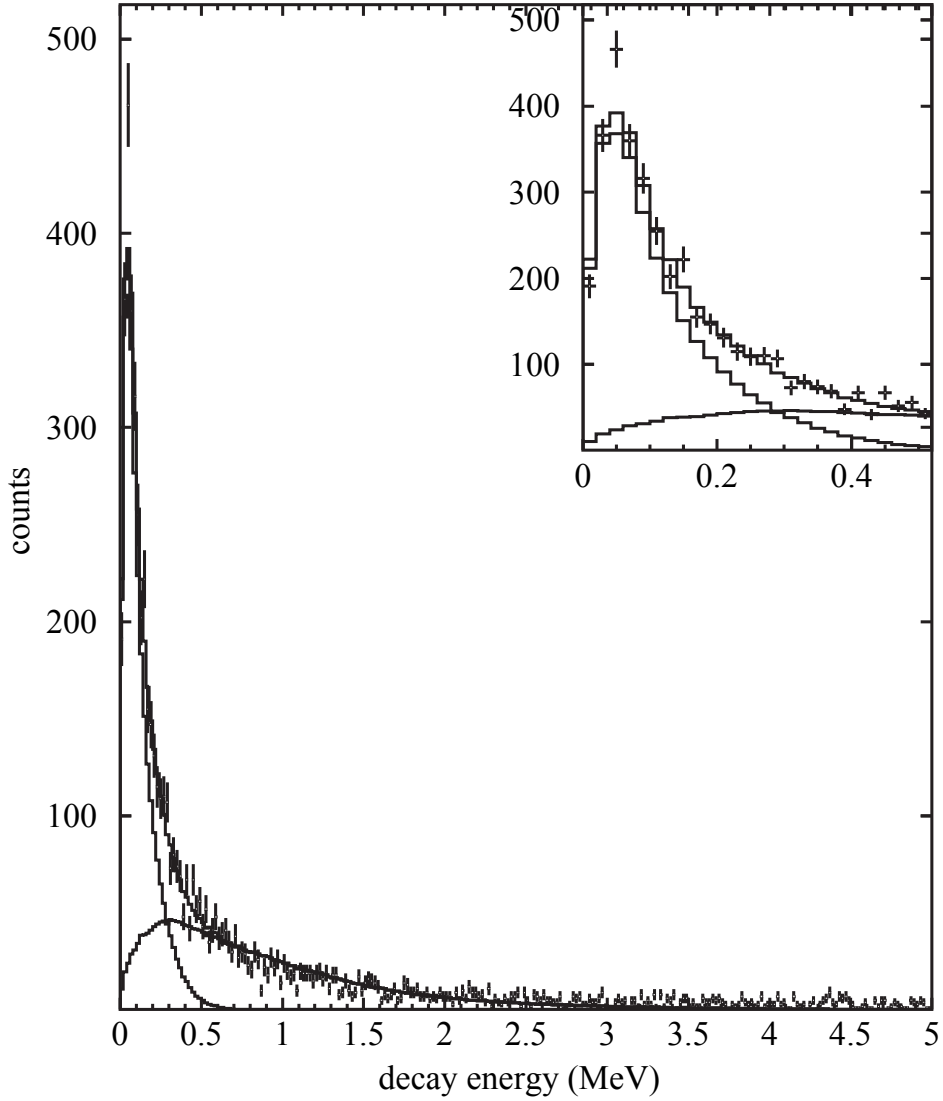


Figure 5.2: Decay energy spectrum of $^{23}\text{O}^*$. The upper histogram is the result of a simulation including contributions from a resonant state ($E_r = 45$ keV, $\Gamma = 20$ keV, middle histogram) and background with a thermalized neutron source (lower histogram).

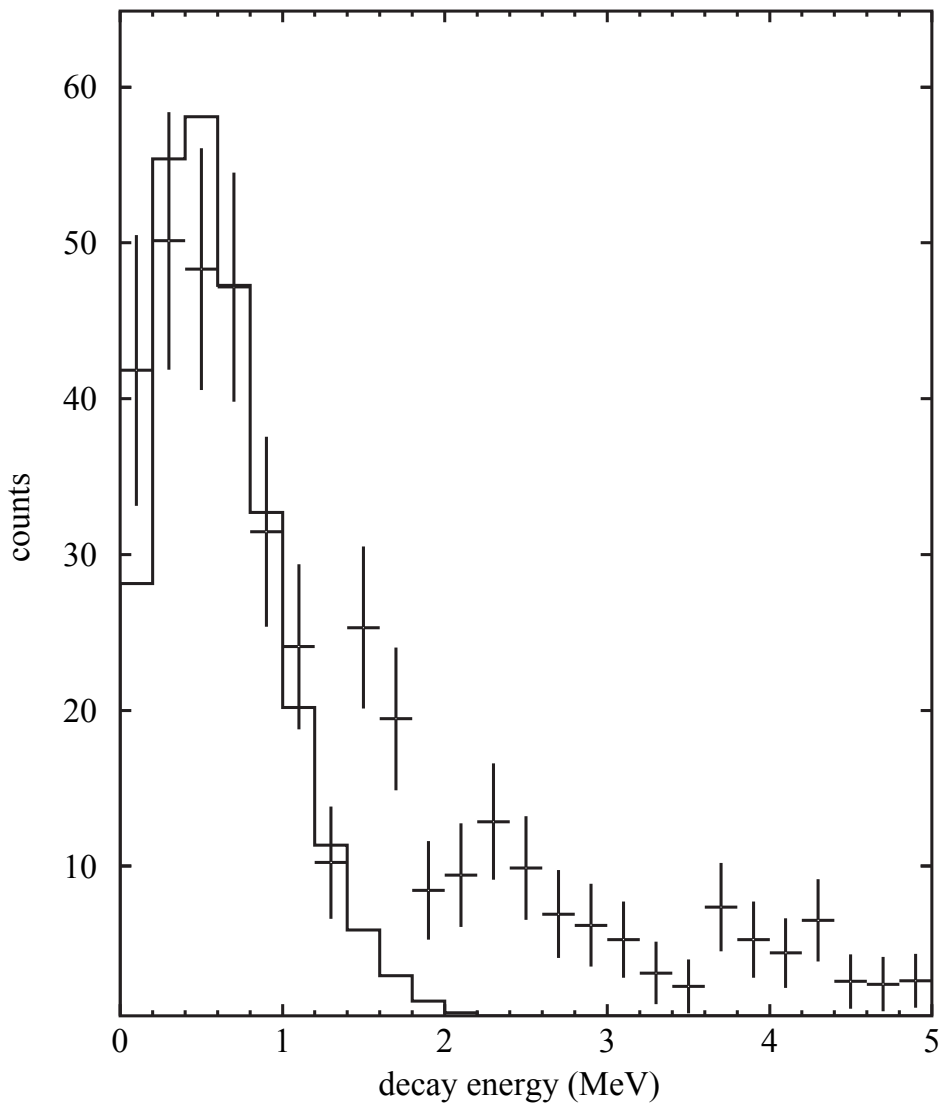


Figure 5.3: Decay energy spectrum of $^{24}\text{O}^*$. The fit assumes a resonance with a resonance energy of $E_r = 600$ keV and a width of $\Gamma = 300$ keV.

The width of the simulated peak in the spectrum shown in Figure 5.3 is due to the experimental resolution and the width of the state. The width of the resonance was kept constant. It should be mentioned that the $^{24}\text{O}^*$ decay energy spectrum is also consistent with a thermalized neutron source, but the neutron energy and angle as well as the opening angle between the neutrons and the fragments do not support this conclusion. In addition, in the population of $^{24}\text{O}^*$ from the breakup of ^{26}Ne there are no thermalized neutrons available as will be described in the next section.

5.3 Physics Interpretation

The broad decay energy spectrum of $^{22}\text{O}^*$ can be explained with the emission of neutrons from a continuum of unbound states. $^{22}\text{O}^*$ can be populated from ^{26}Ne in several different ways as shown in Figure 5.4. It can be produced directly by 2p2n (or α) knock-out or it can be populated by one- or two-neutron evaporation following the population of highly excited states in $^{23}\text{O}^*$ and $^{24}\text{O}^*$ via the 2p1n or 2p knock-out reactions, respectively. In either case, the neutron separation energy of $^{22}\text{O}^*$ is very high (6.85 MeV [29]), which also implies a high level density. Thus it is unlikely to observe individual resonances in the decay of $^{22}\text{O}^*$. Also, ^{21}O has several bound excited states and the present decay energy measurement cannot distinguish between decays to the ground state or any of the excited states. Finally, the neutron measured in coincidence with ^{21}O could also be one of the evaporated neutrons from highly excited $^{23}\text{O}^*$ or $^{24}\text{O}^*$. Thus the overall decay spectrum can be approximated with the emission of a spectrum of thermalized neutrons as described in Section 4.9.

The situation for the decay of $^{23}\text{O}^*$ is slightly different. Again $^{23}\text{O}^*$ can be produced directly into highly excited continuum states via a 2p1n reaction or by evaporation of one neutron following the population of excited states in $^{24}\text{O}^*$. However, the neutron separation energy is only 2.74 MeV, so that the spectrum just above the threshold is still consisting of discrete states and not by a high level density. Thus the present ob-

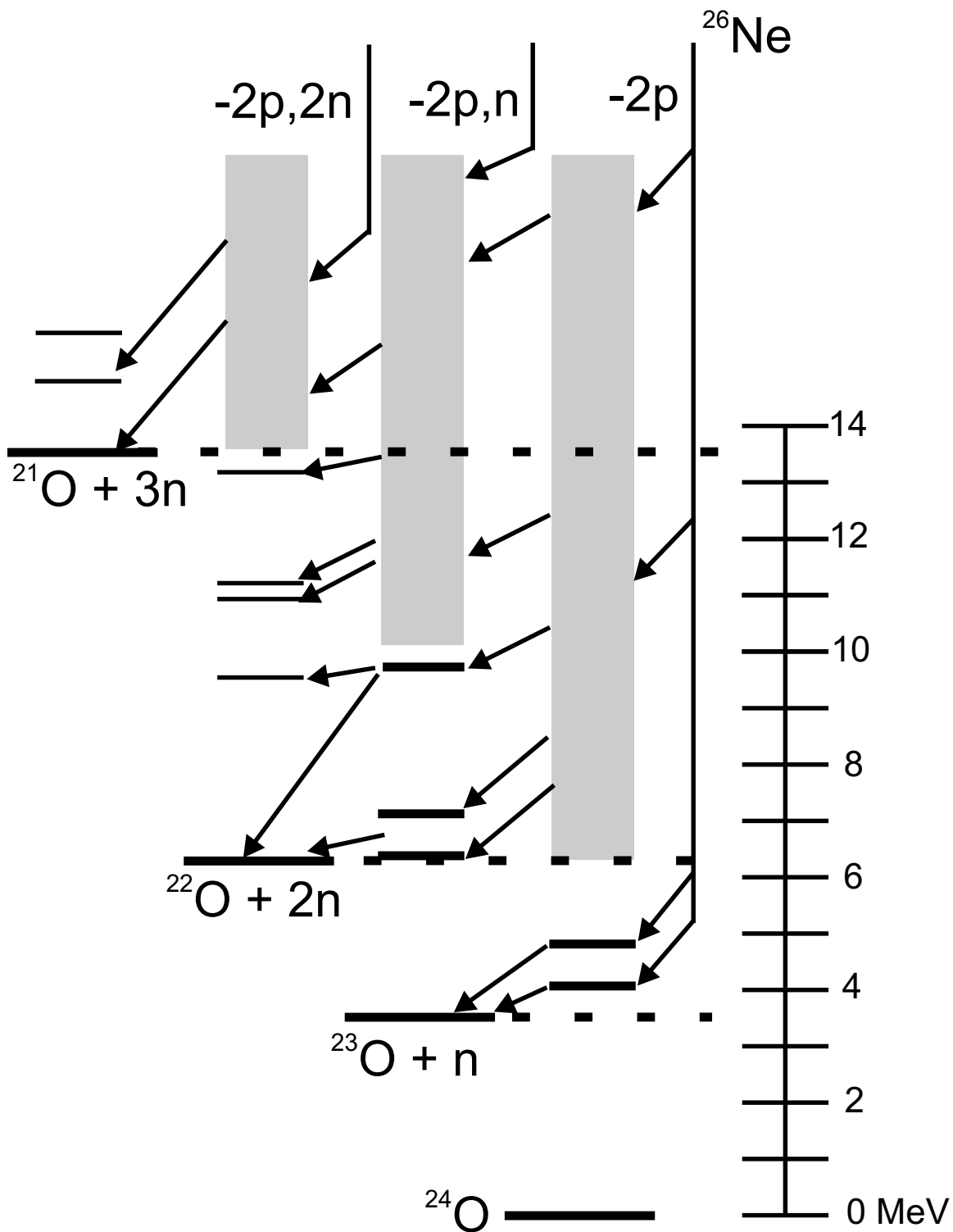


Figure 5.4: Separation energies of three-, two-, and one-neutron relative to ^{24}O calculated using Reference [29]. The gray boxes represent a continuum of unbound states, the dashed lines indicate three-, two-, and one-neutron separation energy relative to ^{24}O , the thick solid lines represent predicted unbound states, and the thin solid lines are measured excited states. The arrows indicate possible paths for producing neutrons with a charged fragment.

Table 5.3: Mass excess [29], E_{decay} and resulting excitation energies in keV for observed states in $^{23}\text{O}^*$ and $^{24}\text{O}^*$. The mass excess values and extracted decay energy uncertainties are rounded to the nearest 10 keV. The excitation uncertainty is rounded up to the nearest 10 keV.

	$^{23}\text{O}^*$	$^{24}\text{O}^*$
Parent mass excess	14610 ± 120	19070 ± 240
Daughter mass excess	9280 ± 60	14610 ± 120
E_{decay} ¹	48 ± 10	670 ± 150
E^*	2788 ± 140	4280 ± 310
¹ this work		

ervation of a narrow resonance just above threshold is strong evidence for an excited state in $^{23}\text{O}^*$ just above threshold. The simulation shown in Figure 5.2 including a narrow resonance and a broad thermal background confirms the observation.

The excitation energy of this state can be calculated with Equation 5.3 and requires the knowledge of the decay energy (E_{decay}) as well as the masses of the parent nucleus (^{23}O), the daughter nucleus (^{22}O), and neutron (M_n).

$$E^* = E_{decay} + M(^{22}\text{O}) + M_n - M(^{23}\text{O}) \quad (5.3)$$

Table 5.3 shows the masses and the decay energy including the uncertainties. The resulting excitation energy of the state in $^{23}\text{O}^*$ is 2788 ± 140 keV. It can be seen from Table 5.3 that the main uncertainty of the excitation energy is not determined by the present decay energy measurement but by the uncertainty of the measured masses.

$^{23}\text{O}^*$ does not have any bound excited states [21], thus the measured energy of the state in $^{23}\text{O}^*$ of 2788 ± 140 keV corresponds to the first excited state of ^{23}O . The observed unbound state(s) of ^{23}O are predicted to have strong single-particle character. Based on the theoretical calculations there are two states with low decay energy, $5/2^+$ and $3/2^+$ [11]. Figure 5.5 shows the single particle configurations of the $5/2^+$ and $3/2^+$ unbound excited states. The $5/2^+$ state is expected to be a configuration with two neutrons in the $1s_{1/2}$ shell and a hole in the $0d_{5/2}$ shell. The $5/2^+$ state in

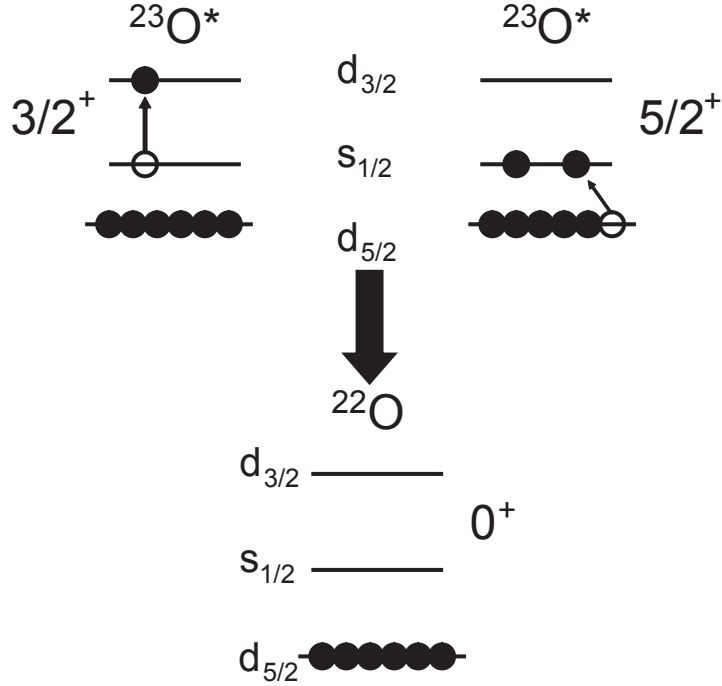


Figure 5.5: Single particle configurations for $5/2^+$ and $3/2^+$ unbound states in ^{23}O . The ^{23}O unbound state(s) emits a neutron and populates the 0^+ ground state of ^{22}O . The empty circles with arrows indicate which sub-shell neutrons were promoted. The solid circles indicate where neutrons are for a given configuration.

^{23}O decays via a second order transition to the 0^+ ground state of ^{22}O which would correspond to a narrow width for the $5/2^+$ state. The $3/2^+$ state is expected to be a configuration with one neutron in the $0d_{3/2}$ which decays to the 0^+ ground state of ^{22}O . The transition involves removing the neutron from the $0d_{3/2}$ sub-shell which would correspond to a wide width for the $3/2^+$ state.

The observed unbound state can be assigned the predicted $5/2^+$ level in $^{23}\text{O}^*$, which is in good agreement in the excitation energy with shell model calculations using the USD interaction [11] as shown in the right side of Figure 5.6. The expected theoretical width for a decay energy of 48 keV from the $5/2^+$ state would be approximately 5 eV according to theory [28]. The experimental resolution of the width dominates the data and so an upper limit of 30 keV for the width of the state is reasonable. The measured state of $^{23}\text{O}^*$ probes the gap between the $0d_{5/2}$ and $1s_{1/2}$

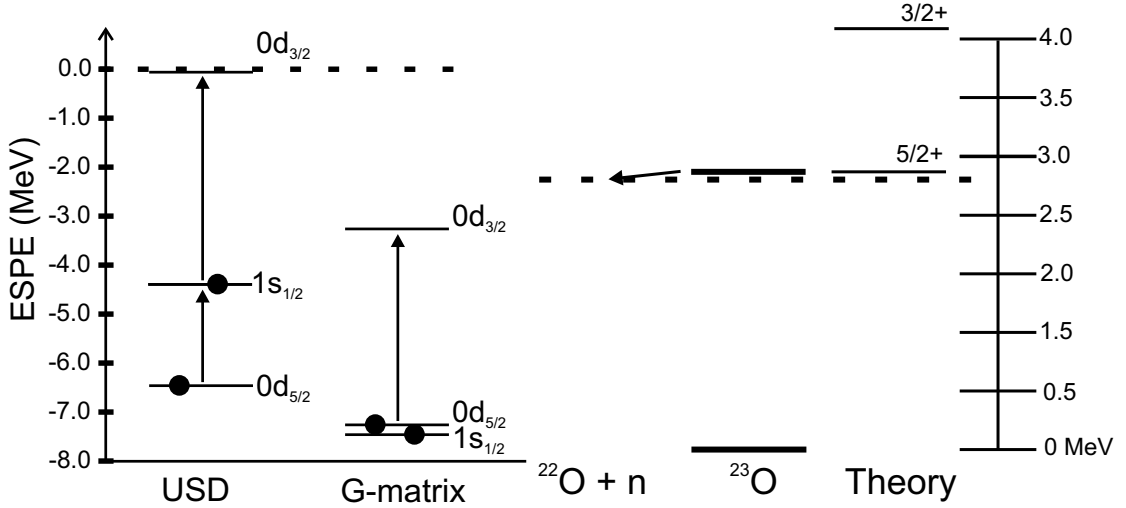


Figure 5.6: Left: Effective single particle energies of the sd shell for USD and G-matrix calculation from Reference [11]. Right: Comparison of the shell model [28] to the extracted decay energy (solid line) for the first unbound excited state of ^{23}O . The dashed line marks the one-neutron separation energy of 2.74 MeV.

shells. The left panel of Figure 5.6 shows the USD and G-matrix calculation of the Effective Single Particle Energies (ESPEs) for $^{24}\text{O}^*$ from [11]. Based on the good agreement to the USD calculation, the sub-shell gap between the $1s_{1/2}$ and $0d_{5/2}$ is well represented. In contrast, the G-matrix calculation predicts a much smaller level spacing between the $1s_{1/2}$ and $0d_{5/2}$ sub-shells. This measurement confirms that the USD calculations represent the level spacing better than the G-matrix calculations as presented in Reference [11]. In the future it would be interesting to search for the second predicted unbound excited state of $3/2^+$ which is not observed in the present data. It should be mentioned that the narrow resonance could in principle also correspond to a decay from a higher lying state in ^{23}O to a bound excited state in ^{22}O .

The simplest decay of the three observed isotopes is ^{24}O because it only can be produced directly by two-proton removal from ^{26}Ne . ^{24}O itself does not have any bound excited states and the number of levels between the one- and two-neutron separation energy are predicted to be low. The continuum of states is only expected to start above the two-neutron separation energy [26]. ^{23}O does not have any bound

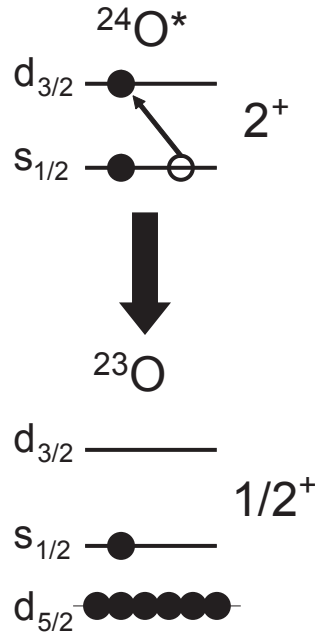


Figure 5.7: Single particle configuration for the 2^+ unbound state in ^{24}O . The ^{24}O unbound state emits a neutron and populates the $1/2^+$ ground state of ^{23}O . The empty circles with arrows indicate which sub-shell neutrons were promoted. The solid circles indicate where neutrons are for a given configuration.

excited states either so that any observed resonance is a unique decay to the ground state and the ambiguity of possible excited state to excited state decay possible in ^{23}O is not present in ^{24}O .

Similar to ^{23}O , the observed decay energy can be converted to an excitation energy in ^{24}O . The relevant masses and the decay energy listed in Table 5.3 result in an excitation energy of 4280 ± 310 keV. The relatively large uncertainty is equal between the uncertainty of the present decay energy measurement and the uncertainty of the mass measurements.

The comparison of the unbound decay energy for $^{24}\text{O}^*$ to theory is shown in Figure 5.8. The measured resonance decay energy from the first excited state from $^{24}\text{O}^*$ is predicted by shell model calculations to be a 2^+ state decaying to the $1/2^+$ ground state of ^{23}O . Figure 5.7 shows the expected configuration of the 2^+ state consisting of one neutron in the $1s_{1/2}$ shell and one neutron in the $0d_{3/2}$ shell. The expected theoretical width for a decay energy of 600 keV from the 2^+ state would be

Table 5.4: Comparison of theoretical calculations of the first neutron unbound excited 2^+ state in ^{24}O .

2_1^+ (MeV)	Calculation
3.81	Obertelli [27]
4.0	Khan [23]
4.18	Siiskonen [25]
4.85	Volya [26]
5.1	Utsuno [24]
5.16	Brown [28]
8.5	Thiamova [22]

approximately 46 keV [28]. The extracted width of approximately 300 keV is larger than that of theory. Table 5.4 shows the theoretical calculations shown in Figure 5.8. The Obertelli [27], Khan [23], and Siiskonen [25] calculations are in agreement within the uncertainty of the measured unbound first excited 2^+ state in this work. The measurement confirms the doubly-magic nature of ^{24}O which is the first direct input to theory for oxygen isotopes measuring the energy gap between the $0d_{3/2}$ and $1s_{1/2}$ sub-shells.

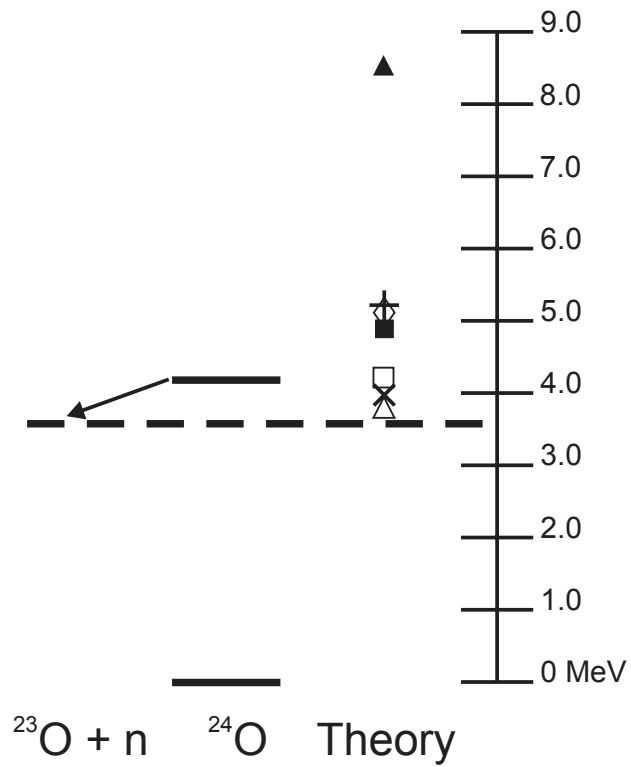


Figure 5.8: Comparison of theory to the extracted decay energy (solid line) for the first unbound excited state of ^{24}O . Theoretical calculations Δ : Obertelli [27], \times : Khan [23], \square : Siiskonen [25], \blacksquare : Volya [26], \diamond : Utsuno [24], $+$: Brown [28], \blacktriangle : Thiamova [22]. The dashed line marks the one-neutron separation energy of 3.61 MeV ^{24}O .

Chapter 6

Summary and Conclusions

Spectroscopy of neutron-unbound states was employed to measure the first excited states in $^{23}\text{O}^*$ and $^{24}\text{O}^*$. The recently commissioned Sweeper Magnet, including the subsequent charged-particle detectors and the Modular Neutron Array, MoNA, were used to detect the charged fragments and neutrons in coincidence. The nuclei were produced by a ^{26}Ne secondary beam impinging on a beryllium target.

The reconstructed decay energy spectra of $^{22}\text{O}^*$, $^{23}\text{O}^*$, and $^{24}\text{O}^*$ were compared to simulations. The decay of excited $^{22}\text{O}^*$, which was produced through one, two, and three neutron emission channels could be explained by the emission from the continuum with a thermal distribution [45, 46]. The $^{23}\text{O}^*$ decay exhibited a strong peak close to the threshold. The resonance energy of 48 ± 10 keV corresponds to an excited state of 2788 ± 140 keV which is consistent with the population of a neutron in the $0d_{5/2}$ sub-shell as predicted by the shell model with the USD interaction [28]. An upper limit for the width of approximately 30 keV for the narrow resonance is established. The uncertainty of the decay energy is dominated by the uncertainty of the mass measurements of ^{23}O and ^{22}O . The $^{24}\text{O}^*$ decay was characterized by a resonance at 670 ± 150 keV with a width of 300 keV. This corresponds to an excited state at 4280 ± 310 keV and can be attributed to the first 2^+ state based on the shell model calculations. The current measurement in connection with the

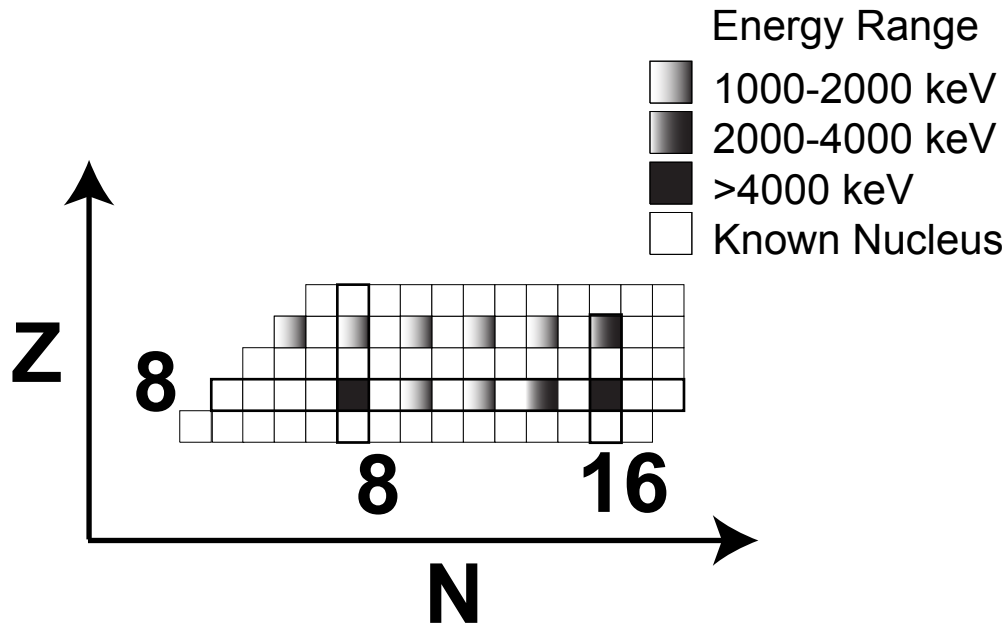


Figure 6.1: First excited 2^+ state trends for nuclei near $Z = 8$. The excitation is marked for some even Z and N isotopes where the measurement of this work has been added to the known data from Reference [3]. $Z = 8$, $N = 8$, and $N = 16$ are outlined with dark black lines.

currently accepted masses of ^{24}O and ^{23}O rules out several shell-model calculations which predict a larger gap between the $1s_{1/2}$ and the $0d_{3/2}$ sub-shells. Figure 6.1 shows the known first 2^+ excited states with the measurement from this work of ^{24}O included. The magic numbers of $N = 8$ near stability and $N = 16$ far from stability are clearly indicated by the high lying first excited state. The high lying excited state of ^{24}O confirms the doubly-magic nature of oxygen for $N = 16$.

Further investigation of the neutron-rich oxygen isotopes is necessary to fully characterize the shell structure in this region of the nuclear chart. The present experiment observed the first unbound excited states in $^{23}\text{O}^*$ and $^{24}\text{O}^*$. In order to reduce the uncertainty of the comparisons to theory, more accurate mass measurements of ^{22}O , ^{23}O , ^{24}O should be performed. New unpublished mass measurements for ^{23}O and ^{24}O have been performed which would reduce the uncertainty in the excitation energy of

^{24}O by approximately 100 keV [47] as well as make the shell model calculations of Volya [26], Utsuno [24] and Brown [28] agree within the uncertainty of the observed state (see Figure 5.8). In addition, new experiments to populate higher-lying excited states in these nuclei are needed. For example, a dedicated experiment for ^{23}O should be able to observe the excited $3/2^+$ state due to a neutron in the $0d_{3/2}$ sub-shell. In order to test the evolution of the shell model even farther away from stability one has to cross the dripline and study the decay of the neutron-unbound ground-state of ^{25}O . This experiment, where ^{25}O was populated via the one-proton stripping reaction from a secondary beam of ^{26}F , has recently been performed and is currently being analyzed [48].

Bibliography

- [1] B.A. Brown. The Nuclear Shell Model Towards the Drip Lines. *Prog. in Part. and Nucl. Phys.*, 47:517, 2001.
- [2] Bohr, A. and Mottleson, B.R. *Nuclear Structure Volume I: Single Particle Motion*. World Scientific, 1998.
- [3] Firestone, R.B. *Table of Isotopes, 8th ed.* Wiley-Interscience, New York, 1996.
- [4] J.A. Cameron and B. Singh. Nuclear Data Sheets for $A = 40$. *Nucl. Data Sheets*, 102:293, 2004.
- [5] B. Singh and J.A. Cameron. Nuclear Data Sheets for $A = 42$. *Nucl. Data Sheets*, 92:1, 2001.
- [6] J.A. Cameron and B. Singh. Nuclear Data Sheets for $A = 44$. *Nucl. Data Sheets*, 88:299, 1999.
- [7] T.W. Burrows. Nuclear Data Sheets for $A = 48$. *Nucl. Data Sheets*, 107:1747, 2006.
- [8] P. Navrátil, J.P. Vary, and B.R. Barrett. Large-basis ab initio no-core shell model and its application to ^{12}C . *Phys. Rev. C*, 62:054311, 2000.
- [9] Mayer, M. G. and Jensen, H.D. *Elementary Theory of Nuclear Shell Structure*. John Wiley and Sons, Inc., 1955.
- [10] P.G. Thirolf, B.V. Pritychenko, B.A. Brown, P.D. Cottle, M. Chromik, T. Glasmacher, G. Hackman, R.W. Ibbotson, K.W. Kemper, T. Otsuka, L.A. Riley, and H. Scheit. Spectroscopy of the 2_1^+ state in ^{22}O and shell structure near the neutron drip line. *Phys. Lett. B*, 485:16, 2000.
- [11] B.A. Brown. New Magic Nuclei Towards the Drip Lines. *Proceedings of the 10th International Conference on Nuclear Reaction Mechanisms (ed. by E. Gadioli) Ricerca Scientifica ed Educazione Permanente*, Supplemento N. 122:41, June 9-13, 2003 Varenna, Italy.
- [12] T.S.S. Kuo and G.E. Brown. Structure of Finite Nuclei and the Free Nucleon-Nucleon Interaction. *Nucl. Phys.*, 85:40, 1966.
- [13] T.S.S. Kuo. State Dependence of Shell-Model Reaction Matrix Elements. *Nucl. Phys. A*, 103:71, 1966.

- [14] B.H. Wildenthal. Empirical Strengths of Spin Operators in Nuclei. *Prog. in Part. and Nucl. Phys.*, 11:3, 1984.
- [15] B.A. Brown and B.H. Wildenthal. Status of the Nuclear Shell Model. *Annu. Rev. of Nucl. Part. Sci.*, 38:29, 1988.
- [16] M. Belleguic, M.-J. López-Jiménez, M. Stanoiu, F. Azaiez, M.-G. Saint-Laurent, O. Sorlin, N.L. Achouri, J.-C. Angélique, C. Bourgeois, C. Borcea, J.-M. Daugas, C. Donzaud, F. De Oliveira-Santos, J. Duprat, S. Grévy, D. Guillemaud-Mueller, S. Leenhardt, M. Lewitowicz, Yu.-E. Penionzhkevich, and Yu. Sobolev. In-beam γ -spectroscopy using projectile fragmentation: Structure of neutron-rich nuclei around $N = 20$. *Nucl. Phys. A*, 682:136c, 2001.
- [17] T. Otsuka, R. Fujimoto, Y. Utsuno, B.A. Brown, M. Honma, and T. Mizusaki. Magic Numbers in Exotic Nuclei and Spin-Isospin Properties of the NN Interaction. *Phys. Rev. Lett.*, 87:082502, 2001.
- [18] T. Otsuka, T. Suzuki, R. Fujimoto, H. Grawe, and Y. Akaishi. Evolution of Nuclear Shells due to the Tensor Force. *Phys. Rev. Lett.*, 95:232502, 2005.
- [19] A. Ozawa, T. Kobayashi, T. Suzuki, K. Yoshida, and I. Tanihata. New Magic Number, $N = 16$, near the Neutron Drip Line. *Phys. Rev. Lett.*, 84:5493, 2000.
- [20] T. Motobayashi, Y. Ikeda, K. Ieki, M. Inoue, N. Iwasa, T. Kikuchi, M. Kurokawa, S. Moriya, S. Ogawa, H. Murakami, S. Shimoura, Y. Yanagisawa, T. Nakamura, Y. Watanabe, M. Ishihara, T. Teranishi, H. Okuno, and R.F. Casten. Large deformation of the very neutron-rich nucleus ^{32}Mg from intermediate-energy Coulomb excitation. page 9, 1995.
- [21] M. Stanoiu, F. Azaiez, Zs. Dombrádi, O. Sorlin, B.A. Brown, M. Belleguic, D. Sohler, M.G. Saint Laurent, M.J. López-Jiménez, Y.E. Penionzhkevich, G. Sletten, N.L. Achouri, J.C. Angélique, F. Becker, C. Borcea, C. Bourgeois, A. Bracco, J.M. Daugas, Z. Dlouhý, C. Donzaud, J. Duprat, Zs. Fülöp, D. Guillemaud-Mueller, S. Grévy, F. Ibrahim, A. Kerek, A. Krasznahorkay, M. Lewitowicz, S. Leenhardt, S. Lukyanov, P. Mayet, S. Mandal, H. van der Marel, W. Mittig, J. Mrázek, F. Negoita, F. De Oliveira-Santos, Zs. Podolyák, F. Pougheon, M.G. Porquet, P. Roussel-Chomaz, H. Savajols, Y. Sobolev, C. Stodel, J. Timár, and A. Yamamoto. $N = 14$ and 16 shell gaps in neutron-rich oxygen isotopes. *Phys. Rev. C*, 69:034312, 2004.
- [22] G. Thiamova, N. Itagaki, and T. Otsuka. Study of the structure of light nuclei by AMD+GCM method. *Czech. JP*, 54:329, 2004.
- [23] E. Khan, N. Sandulescu, M. Grasso, and Nguyen Van Giai. Continuum quasiparticle random phase approximation and the time-dependent Hartree-Fock-Bogoliubov approach. *Phys. Rev. C*, 66:024309, 2002.
- [24] Y. Utsuno, T. Otsuka, T. Mizusaki, and M. Honma. Varying shell gap and deformation in $N = 20$ unstable nuclei studied by the Monte Carlo shell model. *Phys. Rev. C*, 60:054315, 1999.

- [25] T. Siiskonen, P.O. Lipas, and J. Rikovska. Shell-model and Hartree-Fock calculations for even-mass O, Ne, and Mg nuclei. *Phys. Rev. C*, 60:034312, 1999.
- [26] A. Volya and V. Zelevinsky. Discrete and Continuum Spectra in the Unified Shell Model Approach. *Phys. Rev. Lett.*, 94:052501, 2005.
- [27] A. Obertelli, S. Péru, J.-P. Delaroche, A. Gillibert, M. Girod, and H. Goutte. N = 16 subshell closure from stability to the neutron drip line. *Phys. Rev. C*, 71:024304, 2005.
- [28] B.A. Brown. private communication.
- [29] G. Audi, A.H. Wapstra, C. Thibault, J. Blachot, and O. Bersillon. The 2003 AME: (II). Tables, graphs and references. *Nucl. Phys. A*, 729:337–676, 2003.
- [30] J.-L. Lecouey. Is ^{24}O a doubly magic nucleus? *Proposal for PAC27*.
- [31] D. Bazin, B.A. Brown, C.M. Campbell, J.A. Church, D.C. Dinca, J. Enders, A. Gade, T. Glasmacher, P.G. Hansen, W.F. Mueller, H. Olliver, B.C. Perry, B.M. Sherrill, J.R. Terry, and J.A. Tostevin. New Direct Reaction: Two-Proton Knockout from Neutron-Rich Nuclei. *Phys. Rev. Lett.*, 91:012501, 2003.
- [32] P.G. Hansen and J.F. Tostevin. private communication.
- [33] A. Stolz, T. Baumann, T.N. Ginter, D.J. Morrissey, M. Portillo, B.M. Sherrill, M. Steiner, and J.W. Stetson. Production of rare isotope beams with the NSCL fragment separator. *Nucl. Instr. and Meth. B: Beam Interactions with Materials and Atoms*, 241 (1-4):858–861, 2005.
- [34] M.D. Bird, S.J. Kenney, J. Toth, H.W. Weijers, J.C. DeKamp, M. Thoennessen, and A. Zeller. System Testing and Installation of the NHMFL/NSCL Sweeper Magnet. *IEEE Trans. Appl. Supercond.*, 15 (2):1252–1254, 2005.
- [35] T. Baumann, J. Boike, J. Brown, M. Bullinger, J.P. Bychoswki, S. Clark, K. Daum, P.A. DeYoung, J.V. Evans, J. Finck, N. Frank, A. Grant, J. Hinnefeld, G.W. Hitt, R.H. Howes, B. Isselhardt, K.W. Kemper, J. Longacre, Y. Lu, B. Luther, S.T. Marley, D. McCollum, E. McDonald, U. Onwuemene, P.V. Pancella, G.F. Peaslee, W.A. Peters, M. Rajabali, J. Robertson, W.F. Rogers, S.L. Tabor, M. Thoennessen, E. Tryggestad, R.E. Turner, P.J. VanWylen, and N. Walker. Construction of a modular large-area neutron detector for the NSCL. *Nucl. Instr. and Meth. A*, 543:517–527, 2005.
- [36] B. Luther, T. Baumann, M. Thoennessen, J. Brown, P. DeYoung, J. Finck, J. Hinnefeld, R. Howes, K. Kemper, P. Pancella, G. Peaslee, W. Rogers, and S. Tabor. MoNA – The Modular Neutron Array. *Nucl. Instr. and Meth. A*, 505:33–35, 2003.
- [37] W.A. Peters. Ph. D. Thesis. *in preparation*, Michigan State University, 2006.

- [38] R. Fox, C. Bolen, K. Orji, and J. Venema. NSCLSpecTcl Meeting the Needs of Preliminary Nuclear Physics Data Analysis. <http://www.tcl.tk/community/tcl2004/Papers/RonFox/fox.pdf>.
- [39] CERN European Laboratory for Particle Physics. PAW, Physics Analysis Workstation. <http://paw.web.cern.ch/paw/>, 2006.
- [40] O. Tarasov and D. Bazin. LISE++ : design your own spectrometer. *Nucl. Phys. A*, 746:411, 2004.
- [41] M. Berz and J. Hoefkens. COSY INFINITY Version 8.1 Programming Manual. *Technical Report MSUCL-1196, National Superconducting Laboratory, Michigan State University, East Lansing, MI 48824*, see <http://cosy.nscl.msu.edu/>, 2001.
- [42] Leo, W.R. *Techniques for Nuclear and Particle Physics Experiments*. Springer-Verlag, 1994.
- [43] M. Berz, K. Joh, J.A. Nolen, B.M. Sherrill, and A.F. Zeller. Reconstructive correction of aberrations in nuclear particle spectrographs. *Phys. Rev. C*, 47:537–544, 1993.
- [44] A.M. Lane and R.G. Thomas. R-Matrix Theory of Nuclear Reactions. *Rev. of Mod. Phys.*, 30:257, 1958.
- [45] F. Deák, A. Kiss, Z. Seres, G. Caskey, A. Galonsky, and B. Remington. Method for the study of neutron emission from light fragments in intermediate energy heavy-ion collisions. *Nucl. Instr. and Meth. in Phys. Res. A*, 258:67–74, 1987.
- [46] R.A. Kryger, A. Azhari, A. Galonsky, J.H. Kelley, R. Pfaff, E. Ramakrishnan, D. Sackett, B.M. Sherrill, M. Thoennessen, J.A. Winger, and S. Yokoyama. Neutron decay of ^{10}Li produced by fragmentation. *Phys. Rev. C*, 47:R2439, 1993.
- [47] B. Jurado, H. Savajols, W. Mittig, N.A. Orr, P. Roussel-Chomaz, D. Baiborodin, W. Catford, M. Chartier, C.E. Demonchy, Z. Dlouhý, A. Gillibert, L. Giot, A. Khouaja, A. Lépine-Szily, S.M. Lukyanov, J. Mrazek, Y.E. Penionzhkevich, S. Pita, M. Rousseau, and A.C.C. Villari. Odd Even Staggering of Binding Energies and Evolution of the $N = 28$ Shell Closure far from Stability. *in press*.
- [48] C. Hoffman. Ph. D. Thesis. *in preparation*, Florida State University.